

# Northumbria Research Link

Citation: Silva, André Chicrala Amaral (2021) Investigating Magnetic Energy Injection in Solar Active Regions. Doctoral thesis, Northumbria University.

This version was downloaded from Northumbria Research Link:  
<http://nrl.northumbria.ac.uk/id/eprint/47575/>

Northumbria University has developed Northumbria Research Link (NRL) to enable users to access the University's research output. Copyright © and moral rights for items on NRL are retained by the individual author(s) and/or other copyright owners. Single copies of full items can be reproduced, displayed or performed, and given to third parties in any format or medium for personal research or study, educational, or not-for-profit purposes without prior permission or charge, provided the authors, title and full bibliographic details are given, as well as a hyperlink and/or URL to the original metadata page. The content must not be changed in any way. Full items must not be sold commercially in any format or medium without formal permission of the copyright holder. The full policy is available online: <http://nrl.northumbria.ac.uk/policies.html>



**Northumbria  
University**  
NEWCASTLE

**INVESTIGATING MAGNETIC  
ENERGY INJECTION IN SOLAR  
ACTIVE REGIONS**

**ANDRÉ CHICRALA AMARAL SILVA**

PhD

2021



**INVESTIGATING MAGNETIC  
ENERGY INJECTION IN SOLAR  
ACTIVE REGIONS**

ANDRÉ CHICRALA AMARAL SILVA

A thesis submitted in partial fulfilment of  
the requirements of the University of  
Northumbria at Newcastle for the degree of  
Doctor of Philosophy

Faculty of Faculty of Engineering &  
Environment

October 2021



## Abstract

Active regions (ARs) are the manifestation of magnetic fields on the solar surface (i.e., the photosphere). The amount of energy injected through the photosphere can be calculated by the vertical Poynting flux that has two components related to the emergence / shearing of magnetic flux. Part of this energy is stored on the magnetic field for later release as energetic events (i.e., flares). Vector magnetic field data from the Helioseismic Magnetic Imager (HMI) were used to derive photospheric velocities with a Python version of the Differential Affine Velocity Estimator for Vector Magnetograms (DAVE4VM). This thesis work focuses on the interplay between the emergence and shearing components of Poynting flux, using data covering the transit of 51 ARs that are representative of Solar Cycle 24. Given the diversity in morphology and temporal sampling of the data, the results obtained provide a step forward in understanding the general aspects of the Poynting flux in ARs and how its evolution is related to their morphology and flare activity.

In Chapter 5, 3 flaring ARs were compared to 5 non-flaring ARs. Removal of field-aligned flows was verified as not affecting total Poynting flux, but pixels can change by  $\pm 10^9$  erg cm<sup>-2</sup> s<sup>-1</sup> in the two components. As pixels range from  $\pm 10^2$  to  $\pm 10^9$  erg cm<sup>-2</sup> s<sup>-1</sup>, it is clear that the field-aligned flow removal has significant impact on a pixel-by-pixel basis. ARs that produced M-class flares (NOAA 12443 and 12644) had greater frequency of pixels in the histogram extremities than the non-flaring ARs.

In Chapter 6, Emergence was observed to inject the majority of energy for  $\sim 75\%$  of the 51 ARs. This was also observed for all cases when the ARs were grouped by Mt. Wilson classes. The energy injection value ranges were found to escalate with increasing magnetic field complexity, being significantly larger for  $\beta\gamma\delta$ . ARs that evolve upwards in Mt. Wilson class display increased levels of energy injection compared to their counterparts that evolve down or remain the same.

In Chapter 7, when ARs are grouped according to their maximum GOES flare the median values of the energy distributions show a significant rise with increasing flare class. M-/X-class producing ARs display the largest imbalance between Poynting flux components, with emergence having a median of 57% of total energy. When lifetime-accumulated energy is considered against the soft X-ray flare index ( $FI_{SXR}$ ), all ARs with  $FI_{SXR} > 30$  have emergence contributing  $>50\%$ .



# Contents

<b>Abstract</b>	<b>iii</b>
<b>Preface</b>	<b>xv</b>
<b>Acknowledgements</b>	<b>xvii</b>
<b>Declaration</b>	<b>xix</b>
<b>1 Introduction</b>	<b>1</b>
1.1 The photosphere and sunspots . . . . .	2
1.2 The Mt. Wilson classification . . . . .	8
1.3 Active regions and the overlying field . . . . .	9
1.4 Flares . . . . .	14
1.5 Space weather . . . . .	19
1.6 Active region energy injection/removal . . . . .	21
<b>2 Instrumentation and data sources</b>	<b>25</b>
2.1 Spectropolarimetry . . . . .	25
2.1.1 The Zeeman effect . . . . .	25
2.1.2 The Hanle effect . . . . .	28
2.1.3 The Stokes Parameters . . . . .	29
2.2 The Helioseismic and Magnetic Imager . . . . .	32
2.3 NOAA/SWPC reports . . . . .	38
<b>3 Poynting flux and photospheric velocity inversion methods</b>	<b>43</b>
3.1 Poynting flux theory . . . . .	43
3.1.1 Poynting flux in the photosphere . . . . .	43
3.1.2 Proxy Poynting flux . . . . .	45
3.1.3 Removal of field aligned velocities . . . . .	46
3.1.4 Modified Poynting flux equations . . . . .	48
3.2 Calculating velocities from magnetic field data . . . . .	49
3.2.1 Velocity inversion in the photosphere . . . . .	49

3.2.2	Overview of different methods used for velocity inversion with LOS magnetic field data . . . . .	50
3.2.3	Velocity inversion using vector magnetic field data . . . . .	53
<b>4</b>	<b>Data processing</b>	<b>57</b>
4.1	PyDAVE4VM . . . . .	57
4.1.1	Python in Solar/Astro Physics . . . . .	57
4.1.2	Porting the code . . . . .	58
4.1.3	Optimizing the code . . . . .	59
4.1.4	Addons . . . . .	61
4.2	Results output database . . . . .	63
4.3	The pipeline . . . . .	64
4.3.1	Selecting regions . . . . .	67
<b>5</b>	<b>Case study of the Poynting flux of 3 flaring and 5 non-flaring ARs</b>	<b>69</b>
5.1	History of solar Poynting flux measurements . . . . .	69
5.1.1	Poynting flux before modern instrumentation (legacy era) . . . . .	69
5.1.2	Proxy Poynting flux (MDI era results) . . . . .	71
5.1.3	Poynting flux in modern times (SDO era) . . . . .	74
5.2	The data set . . . . .	77
5.3	The impact of removing field-aligned flows . . . . .	79
5.4	Distribution of Poynting flux per pixel . . . . .	82
5.5	Evolution of FOV-integrated energy . . . . .	87
5.6	A closer look at NOAA 12644 . . . . .	91
5.7	Discussion . . . . .	93
<b>6</b>	<b>Differences in Poynting flux behaviour between Mt. Wilson classifications</b>	<b>99</b>
6.1	Introducing the dataset . . . . .	100
6.2	Overall energy share . . . . .	103
6.3	Energy injection as a function of Mt. Wilson class . . . . .	105
6.3.1	Analysis per most complex Mt. Wilson class issued over lifetime . . . . .	105
6.3.2	Analysis per daily Mt. Wilson classification issued . . . . .	108

6.3.3	Poynting flux and the daily changes in Mt. Wilson class . . . . .	112
6.4	Discussion . . . . .	115
<b>7</b>	<b>Statistical relationship between Poynting flux behaviour and flare activity level</b>	<b>119</b>
7.1	Energy accumulation and maximum flare level produced . . . . .	120
7.2	A closer look at the M- and X-class flaring regions . . . . .	123
7.3	Relationship between lifetime-accumulated energy and lifetime-accumulated flare index . . . . .	126
7.4	Discussion . . . . .	127
<b>8</b>	<b>Conclusions &amp; Future Work</b>	<b>133</b>
8.1	Principal results . . . . .	134
8.1.1	Case study of the Poynting flux of 3 flaring and 5 non-flaring ARs . . . . .	134
8.1.2	Differences in Poynting flux behaviour between Mt. Wilson classifications	135
8.1.3	Statistical relationship between Poynting flux behaviour and flare activity level . . . . .	136
8.2	Future work . . . . .	137
<b>Appendix A List of ARs used in this work</b>		<b>141</b>
<b>References</b>		<b>142</b>

## List of Figures

1	The structure of the Sun and some of the major events that take place on its surface. Credits: By Kelvinsong (Own work) [CC BY-SA 3.0 ( <a href="http://creativecommons.org/licenses/by-sa/3.0">http://creativecommons.org/licenses/by-sa/3.0</a> )], via Wikimedia Commons. . . . .	2
2	Observations of NOAA 12192 using different instruments. Source: Toriumi and Wang (2019) . . . . .	4
3	Yearly average of the sunspot number. Source: Solar Cycle Science <a href="http://www.solarcyclescience.com/solarcycle.html">http://www.solarcyclescience.com/solarcycle.html</a> . . . . .	6
4	The butterfly diagram represents the appearance of sunspots during the solar cycle. Credits: NASA, Marshal Space Flight Center, Solar Physics - <a href="http://solarscience.msfc.nasa.gov/images/bfly.gif">http://solarscience.msfc.nasa.gov/images/bfly.gif</a> (updated monthly). . . . .	6
5	The magnetic butterfly diagram represents how the surface magnetic field is distributed over the solar cycle. Source: Solar Cycle Science <a href="http://www.solarcyclescience.com/solarcycle.html">http://www.solarcyclescience.com/solarcycle.html</a> . . . . .	7
6	The solar plasma in the corona as observed by the AIA 171Å(top left), 193Å(top right) and 211Å(bottom) at 2015-11-04 23:43. Source: LMSAL Sun today. . . .	10
7	Picture of the solar corona in white light (left) and the same picture after digital enhancement. Source: Rušin et al. (2010) . . . . .	11
8	GOES and AIA measurements for different wavelengths on 2015-11-04 when NOAA 12443 produced a sequence of flares including a M-class flare. Source: LMSAL Sun today . . . . .	16
9	Left: The sunspot, seen in the continuum, where the spectral line observations studied by Hale were measured. Right: the triplet formed by the magnetic field effect in the Iron line $\lambda$ 617.3 nm. Source: Hale et al. (1919). . . . .	27
10	Illustration of a single emission line breaking into different components in the presence of a magnetic field. Source: Santiago (2004). . . . .	28
11	Changes in polarisation of light caused by the Zeeman effect. Source: Trujillo Bueno (2003) . . . . .	31
12	Measurements of the Stokes parameters on the AR NOAA 12443 measured along the Fe lines. Source: Silva (2017) . . . . .	32

13	Distribution of HARP tracked regions on the solar disk at 2013/08/03 21:36 as made available by the HMI science team. Courtesy: JSOC and HMI science team.	35
14	Example of the SWPC SRS file for 2015-11-04. . . . .	39
15	Example of the SWPC <i>Events</i> file for 2015-11-04. . . . .	40
16	Diagram of a flux tube rising through the photosphere. Source: Démoulin and Berger (2003). . . . .	47
17	Optimization curves comparing the accuracy of DAVE (left panel) and DAVE4VM (right panel) as a function of the window size. Source: Schuck (2008). . . . .	54
18	Scatter plots of the different velocity components obtained by DAVE (left panel) and DAVE4VM (right panel) against the “ground truth” of the ANMHD simulation. The points in red, blue, and black represent the x, y, and z components of the velocity vector, respectively. Source: Schuck (2008). . . . .	55
19	Scatter plots for the three velocity components ( $v_x, v_y, v_z$ ) calculated by Python and IDL versions of DAVE4VM. The calculation was performed using the SHARP data for AR NOAA 12443 on 2015-11-04 at 12:00 UT and 12:12 UT. It can be seen that the calculations from Python and IDL display an excellent correspondence.	60
20	Example of a PyDAVE4VM pipeline configuration file. . . . .	65
21	This diagram illustrates how the main modules used to conduct the analysis over the set of observations of an AR communicate between themselves. . . . .	66
22	Mt. Wilson classification of the whole dataset of NOAA regions from the beginning of the HMI coverage in 2012 to the end of 2018. . . . .	67
23	(a) Area-averaged and (b) area-integrated scatter plots showing the correlation between Poynting flux and coronal X-ray brightness. Source Tan et al. (2007). . .	72
24	Sum over time of the proxy Poynting flux ( $S_R$ ) multiplied by pixel area ( $dA$ ) and the time between magnetograms ( $\Delta t$ ). Source Welsch et al. (2011). . . . .	73

25	Left: Scatter plots between the velocities obtained by DAVE4VM before and after using Equations 3.14 and 3.15 to remove the field aligned components. Right: difference between the velocities before and after removing the field aligned velocity atop the image of the vertical magnetic field. To improve visualization the values in the colorbar were clipped for horizontal and vertical velocities at, respectively, 0.5 and 0.25 km s <sup>-1</sup> which represents less than the full extent of the differences as it can be seen in the scatter panels. . . . .	80
26	Left: Scatter plots between the Poynting flux calculated using the velocities obtained by DAVE4VM before and after using Equations 3.14 and 3.15 to remove the field-aligned components. Right: difference between the Poynting flux components before and after removing the field aligned velocity overlaid on an image of vertical magnetic field. To improve visualization the values in the colorbar were clipped at 5 × 10 <sup>8</sup> erg cm <sup>-2</sup> s <sup>-1</sup> which represents less than the full extent of the differences as it can be seen in the scatter panels. . . . .	81
27	Frequency distributions of negative (left column) and positive (right column) values of Poynting flux emergence component, $S_{\perp n}$ , over whole AR observation period. The top row displays all five non-flaring ARs, with the lower three rows showing the average of these distributions (in blue) for comparison with each of the flaring ARs (in red). . . . .	83
28	Same as Fig. 27, but for the Poynting flux shearing component, $S_{\perp t}$ . . . . .	84
29	Same as Figs. 27 and 28, but for the total Poynting flux, $S_{\perp s}$ . . . . .	85
30	Overlays of $S_{\perp n}$ (top), $S_{\perp t}$ (middle), and $S_{\perp s}$ (bottom) on continuum intensity (left) and radial magnetic field (right) images of NOAA 12443 at 2015-11-04 12:10 UTC. Values of Poynting flux and magnetic field are clipped at ±10 <sup>8</sup> erg cm <sup>-2</sup> s <sup>-1</sup> and ±1000 G, respectively, to improve the visualisation. . . . .	86

31	Time series of the energy evolution the three flaring regions compared with the non flaring regions of the control set. Each time step assume that the power obtained by calculating the Poynting flux stayed constant over the 720 seconds window. Row wise, from top to bottom we have the plots for the contributions given by the emergence, shearing and total Poynting flux. Column wise from left to right we have NOAA 11593, 12644 and 12443. The red dashed line mark the latitudes where NOAA 12644 and 12443 produced a M class flare. The gray dashed lines mark the latitudes where problems with disambiguation are diminished in our dataset. . . . .	88
32	Time series of the cumulative energy for the three flaring regions compared with the non flaring regions of the control set. Row wise, from top to bottom we have the plots for the contributions given by the normal, tangential and total Poynting flux. Column wise from left to right we have NOAA 11593, 12644 and 12443. The red dashed line mark the latitudes where NOAA 12644 and 12443 produced a M class flare. The gray dashed lines mark the latitudes where problems with disambiguation are diminished in our dataset. . . . .	90
33	Frequency distribution of the most complex Mt. Wilson classification issued for each region in the dataset. . . . .	102
34	Frequency distribution of every daily Mt. Wilson classification issued for each region in the dataset. . . . .	102
35	Box-and-whisker plot of the share of the lifetime-accumulated energy that was injected by emergence (blue box) or shearing (orange box). The red line marks the point where the contribution of the components are balanced (i.e., 50%). . . .	104
36	Top: Box-and-whisker plots of the lifetime-accumulated energy by emergence (blue) and shearing (orange) and their total (green), grouped according to the most-complex Mt. Wilson classification the ARs exhibited over their lifetime. The dashed red line indicates net zero change. Bottom: Box-and-whisker plots of the share of total lifetime-accumulated energy that is injected by emergence (blue) and shearing (orange), grouped according to the most-complex Mt. Wilson classification the ARs exhibited over their lifetime. The dashed red line marks the point where the contributions of the components are balanced. . . . .	107

37	Same as Figure 36, but for daily-accumulated energies. The left (right) column contains the case for energy-accumulation over the 24 hours preceding (following) the Mt. Wilson classification being issued. . . . .	110
38	Same as Figure 36, but with the ARs separated into panel columns according to their daily starting Mt. Wilson classifications. In each panel the x-axis now displays the Mt. Wilson classification that the ARs subsequently evolve into at the end of the 24 hours that energy was accumulated over. . . . .	113
39	Top: Box-and-whisker plots of the lifetime-accumulated energy by emergence (blue) and shearing (orange) and their total (green), grouped according to the maximum GOES flare class the ARs exhibited over their lifetime. The dashed red line indicates net zero change. Bottom: Box-and-whisker plots of the share of total lifetime-accumulated energy that is injected by emergence (blue) and shearing (orange), grouped according to the maximum GOES flare class the ARs exhibited over their lifetime. The dashed red line marks the point where the contributions of the components are balanced. . . . .	121
40	Evolution of energy injection via Poynting flux for NOAA regions 11654, 11748, 11968, 12253, 12257, 12443, 12644 and 12673. The blue, green and orange curves represent, the energy injected via the emergence, shearing and total Poynting flux, respectively. The red vertical lines represent the moment where the M- (dotted lines) and X-class (dashed lines) flares took place. . . . .	124
41	Top panel: Scatter plots of the lifetime-accumulated energy injected by emergence (blue) and shearing (orange) and their total (green) against the accumulated soft X-ray flare index of every region. The dashed red line indicates net zero change. Bottom panel: Scatter plots of the share of the lifetime-accumulated total energy that is injected by emergence (blue) and shearing (orange) the accumulated soft X-ray flare index of every region. The dashed red line marks the point where the contributions of the components are balanced. . . . .	127
42	Magnetograms of NOAA regions 12546 (left; 2016-05-15), 12665 (centre; 2017-07-10), and 12673 (right; 2017-09-03). The regions were close to the disk centre at the time those images were produced. Source: LMSAL. . . . .	130

43	Lifetime-accumulated energy for all of the ARs in the complete data set as a function of their NOAA number. . . . .	139
----	---	-----

## List of Tables

1	Mt. Wilson classification rules. . . . .	8
2	A short comparison guide between the Zeeman and Hanle effects. Adapted from Ignace et al. (1997). . . . .	29
3	Comparison between the performance of DAVE and DAVE4VM. Source: Schuck (2008). . . . .	55
4	A comparison between the energy exchange in the chromosphere and corona. Adapted from Withbroe and Noyes (1977). . . . .	70
5	Summary of the ARs featured in this work showing NOAA number designation, number of GOES flares produced by the AR, lifetime-average spot area expressed in millionths of the solar hemisphere, and daily Mt. Wilson class. . . . .	78
6	Summary of the ARs featured in this work showing NOAA number designation, number of GOES flares produced by the AR, lifetime-average spot area expressed in millionths of the solar hemisphere, and daily Mt. Wilson class. . . . .	90
7	Median values from the box-and-whisker plots of lifetime-accumulated energy grouped by lifetime-maximum Mt. Wilson classification in Figure 36. . . . .	108
8	Median values from the box-and-whisker plots of daily-accumulated energy grouped by daily Mt. Wilson classification in Figure 37. . . . .	111
9	Median values from the box-and-whisker plots of daily-accumulated energy grouped by maximum GOES flare class in Figure 39. . . . .	122
10	List of ARs featured in this thesis (2012–2013). . . . .	141
11	List of ARs featured in this thesis (2014–2017). . . . .	142

## **Preface**

The Sun is essential for so many aspects of life (including making it possible for a start) on Earth that it is natural to try to better understand and predict its behaviour. The geomagnetic field mostly keeps the Earth safe from most of the energetic phenomena that could otherwise dramatically impact human activities. However, as our ambition towards being a space-born species increases, it becomes more pressing to improve our capacity to forecast energetic events that may harm equipment or even humans that are in spacecrafts flying above the magnetosphere.

Most of the extreme energetic phenomena are associated with the evolution of solar active regions. In this sense, this work tries to produce a general description of how energy is injected in active regions as a whole and according to their magnetic field complexity. Then, knowing how the energy is building up it is possible to explore if there are any links between energy injection and flares. As the ARs studied in here were sampled to proportionally represent the ARs of Solar Cycle 24, the results should offer a solid benchmark for future works.



## Acknowledgements

I would like to formally thank:

- My supervisor Shaun for all the guidance and fun we had;
- My fiancée Anna for all the love, care and for keeping me sane;
- My family for supporting me even though they have no clue of what I do;
- My office mates for being the best office mates I could ever have wished for;
- My friends in Brazil that I miss every day;
- My friends from other countries that receive me with open arms in their land;
- My teachers that resisted the urge to throw a brick at me (and also the one that did not);
- The university for the scholarship.

I really hope that I haven't over my life been such an ungrateful cookie that those who helped me don't know how much I appreciate it and need to rely on this formal piece of written validation.



## **Declaration**

I declare that the work contained in this thesis has not been submitted for any other award and that it is all my own work. I also confirm that this work fully acknowledges opinions, ideas and contributions from the work of others. The work was done in collaboration with my supervisor Dr. D. Shaun Bloomfield.

Any ethical clearance for the research presented in this thesis has been approved. Approval has been sought and granted by the Faculty Ethics Committee / Ethics Online on 18/01/2018.

**I declare that the Word Count of this thesis is 41,162 words.**

Name: André Chicrala Amaral Silva

Signature:

Date: 26 October 2021



# Chapter 1

## Introduction

The Sun is the closest star to Earth and the main responsible for several aspects of our daily life on the planet ranging from the very heating that keeps life going as we know to disturbances in magnetosphere.

Active regions (ARs) can often be seen in the Sun and have intense magnetic fields that are able to store vast amounts of energy. The stored energy may suddenly be released during a magnetic field reconnection which will result in flares that may be followed by a coronal mass ejection (CME) or not.

Flares and CMEs are some of the main drivers of space weather and can produce a diversity of effects on Earth, one of the most known examples being aurorae. However, the near-Earth space weather can also have negative effects such as the damaging of power grids. Since the mechanisms that cause a flare or a CME are not yet fully understood, the capacity of predicting these events and their impact in the space weather still have room for improvement.

This thesis aims to improve our understanding of energy injection and removal in ARs at the solar surface and to study how this injection/removal changes as the ARs pass over the solar disk. To ensure a thorough description, the ARs studied have different levels of flaring and magnetic structure carefully sampled to reflect what is commonly observed in the solar surface.

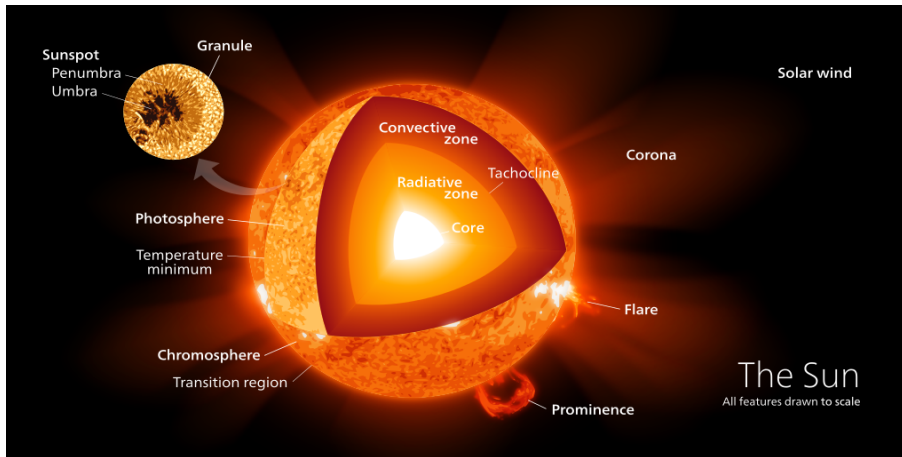


Figure 1: The structure of the Sun and some of the major events that take place on its surface. Credits: By Kelvinsong (Own work) [CC BY-SA 3.0 (<http://creativecommons.org/licenses/by-sa/3.0>)], via Wikimedia Commons.

## 1.1 The photosphere and sunspots

The Sun is a G-type star located on the main sequence of the Hertzsprung-Russel diagram. As such, its internal structure consists of three different layers: the core, the radiative zone and the convective zone. Its atmosphere is also composed of three layers: the photosphere, chromosphere and corona. The structure of the Sun and some of its features are illustrated in Figure 1.

The photosphere, also known as the solar surface, is the lowest layer of the solar atmosphere and can directly be observed with a telescope. Therefore, it presents the main access for the understanding of the processes in the solar interior and atmosphere. Assuming that the solar atmosphere is stratified, the photosphere is about 500 km thick and the plasma that composes it mostly consists of hydrogen and has a density of approximately  $10^{17}$  particles per cubic centimeter. The temperature in the photosphere is about  $\sim 4000 - 6000$  K which is “only” about three to four times hotter than molten lava.

Atop the photosphere, the remaining two layers that compose the solar atmosphere are the chromosphere and the corona. The chromosphere and corona are considerably less dense than the photosphere, while the chromosphere is about  $10^{15} \text{ cm}^{-3}$  dense, the corona ranges from  $10^8 \text{ cm}^{-3}$  at the base to less than  $10^6 \text{ cm}^{-3}$  at its upper parts. In terms of size, the chromosphere is four times as wide as the photosphere, being about 2000 km wide while the corona can stretch itself up to a few solar radius. One of the most intriguing features that is observed when comparing the different layers of the solar atmosphere is the temperature gradient. When the temperature

is measured radially following an outward direction from the Sun, starting from the core, it initially drops sharply from values over 15 million K to 4000 K in the photosphere. The temperature starts increasing again reaching values of up to 20 000 K in the chromosphere and finally surpasses 1 million K in the corona. The transition region between the chromosphere and the corona is roughly 100 km thick and it is where the temperatures show their largest increase rising from  $10^4$  K to  $10^6$  K. Although the mechanisms that cause the temperature gradient to invert are and have been the source of intense debate for over half a century already (e.g., Alfvén, 1947; Schatzman, 1949), there is still no consensus on how coronal heating takes place. However, new research keeps unveiling new features in the corona (e.g., Antolin, 2020) that may contribute to solving this intriguing problem.

It can be observed that the solar surface rotates around its own polar axis. However, unlike Earth, the rate at which it rotates varies with latitude. At the solar equator the Sun rotates considerably faster, with a period of 24.47 days, while close to the poles the period reaches almost 38 days (Hrazdára et al., 2021).

Stars are known to produce magnetic fields due to their plasma motions and the exact mechanisms that produce these magnetic fields and how intense they can become vary according to the stellar type. Stars of different stellar types can vary significantly in mass, rotation speed and depth of their convective zone causing them to have distinct plasma motions. The solar magnetic field is believed to be produced at the tachocline, which is the region between the radiative and convective zones, by dynamo action (see chapter 7 in Schrijver and Zwaan, 2008). The magnetic structures that are formed at the tachocline expand due to magnetic pressure, which make them buoyant and capable of emerging through the solar surface where they can be directly observed. Since it is not possible to directly observe the tachocline, studies on the formation of solar magnetic fields are conducted using simulations. Charbonneau (2020) presents an extensive discussion on the different models that try to understand the solar dynamo.

Since the photosphere is located just above the convection zone, where the dynamics are mainly driven by convection, it displays a granular pattern over the majority of its area. Granules are the top of convection cells and, typically, each granule is between 100 – 1000 km wide, with the exception of super granules that can be thirty times as large. For comparison, the convection zone depth is approximately 0.3 solar radius or  $\approx 2 \times 10^5$  km. Both granules and super granules have a

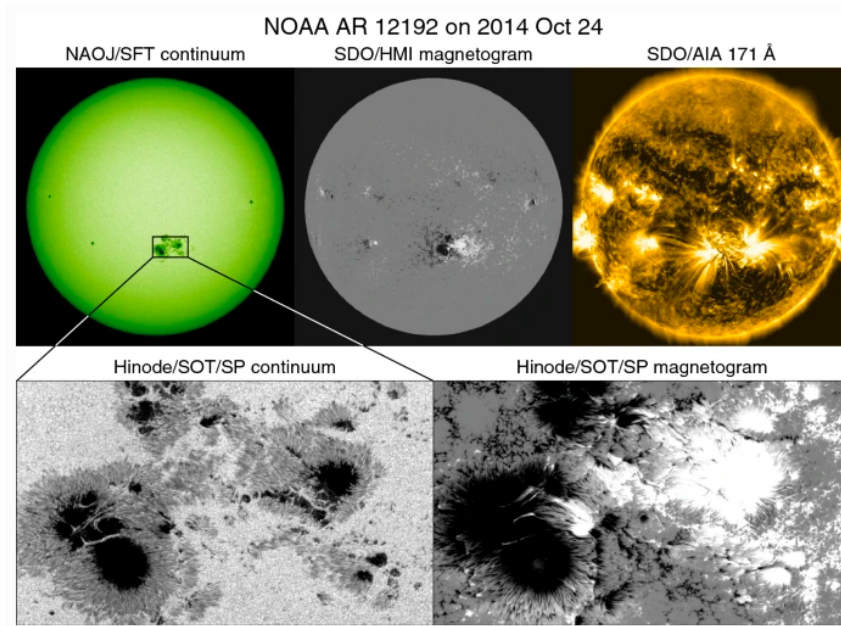


Figure 2: Observations of NOAA 12192 using different instruments. Source: Toriumi and Wang (2019)

rather small magnetic field associated with them, which is of a few Gauss only. Granular regions compose much of what is known as the quiet Sun, which receives this name due to the fact that there are no extreme releases of energy associated with these regions. A review about observations of the quiet Sun can be found in Bellot Rubio and Orozco Suárez (2019).

The emergence and submergence of magnetic structures in the photosphere show that these structures are displaying a fluid-like behaviour. The study of how the dynamics of magnetic structures in a plasma can be approximated with fluid dynamics started when Alfvén (1942) published his discoveries of Electromagnetic-Hydrodynamic Waves kickstarting the field that is now known as magnetohydrodynamics. The Alfvén Theorem (Alfvén, 1943) shows that plasma motions perpendicular to the magnetic field lines do not take place on a perfectly conducting fluid such as a plasma and, then, the magnetic field lines will move with the plasma explaining the direct observation of the fluid-like motion displayed by the magnetic structures in the solar atmosphere.

The most prominent manifestation of the magnetic fields that are produced by dynamo action within the convection zone are the sunspots that can often be observed in the solar surface, as illustrated in Figure 2. At the beginning of the previous century, sunspots were observed to have an intense magnetic field (Hale, 1908) that can reach over 4000 G. Sunspots look darker in relation to their surroundings as their strong magnetic field inhibits the convective heat flow. The magnetic

field in sunspots can be measured using the Zeeman effect (Zeeman, 1897) that predicts how an emission line can split depending on the magnetic field intensity. A few years after the discovery of the Zeeman effect, the discovery of the Hanle effect (Hanle, 1925) showed that the presence of a magnetic field can also affect the polarization of emission lines. The discoveries of Pieter Zeeman and Wilhelm Hanle constitute the basis that allows studying the magnetic field in the solar atmosphere in greater detail including the capacity to directly measure these fields. A discussion about how magnetic fields are measured in the solar atmosphere can be found in Chapter 2 along with details about the instrumentation used in this work.

When observed in continuum emission, a sunspot consists of a dark umbra region that is partially or entirely surrounded by an penumbra region. Furthermore, a sunspot is considered “regular” if it has a single umbra with a reasonably circular structure. Sunspots may present a diversity of shapes and some of them exhibit a complex morphology where the magnetic field polarities are not clearly separated. Also, it is not uncommon to observe sunspots in groups. The magnetic field of a sunspot is more intense and vertically oriented in the center of the umbra region and it falls monotonically in the outward direction while also changing direction to be more horizontally oriented in the penumbra. Pores also appear in the continuum as dark spots and have a significant magnetic flux of up to 1000 G. However, pores are smaller in size than most sunspots having a radius that can reach up to 1500 km and they are not surrounded by a penumbra (Simon and Weiss, 1970; Solov’ev et al., 2019).

The idea of monitoring the number of sunspots that can be seen in the solar surface dates back to the 1800s (Wolf, 1851) but the daily counting of sunspot groups was introduced more than a century later (Hoyt and Schatten, 1998). Although the telescopes used to observe the Sun and sunspots improved dramatically since the daily counts started, the historical data that were gathered still provide a unique chance to study the Sun on a longer time scale. Figure 3 shows the sunspot number as recorded from the earliest solar observations to the recent times.

Sunspot count is a strong indicator of solar activity and, by observing the sunspot number variation over time, it can be seen that the frequency at which they appear in the photosphere varies according to the solar cycle (Harvey, 1994). While a peak in the number of sunspots can be observed close to the solar maximum, the number of regions observed during the solar minimum may even drop to zero for many days in a row. The location where sunspots tend to be found also

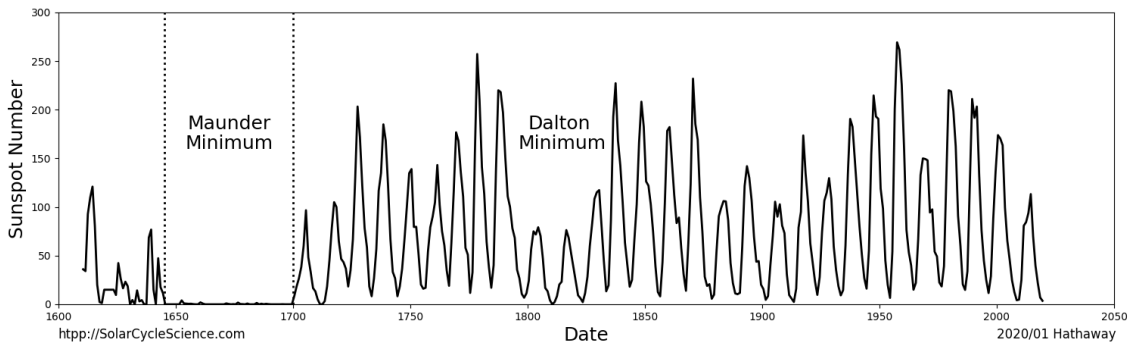


Figure 3: Yearly average of the sunspot number. Source: Solar Cycle Science <http://www.solarcyclescience.com/solarcycle.html>

**DAILY SUNSPOT AREA AVERAGED OVER INDIVIDUAL SOLAR ROTATIONS**

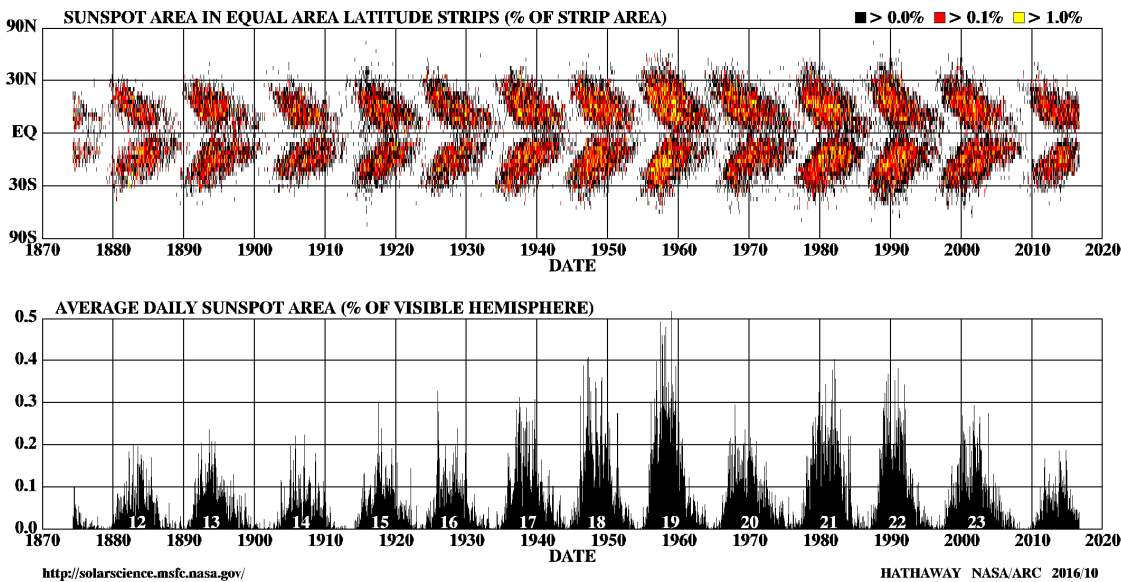


Figure 4: The butterfly diagram represents the appearance of sunspots during the solar cycle. Credits: NASA, Marshall Space Flight Center, Solar Physics - <http://solarscience.msfc.nasa.gov/images/bfly.gif> (updated monthly).

varies according to the solar cycle. When close to the beginning of the solar cycle sunspots can be seen as much as 40° away from the equator and are more observed closer to the equator as the cycles progress. This variation in frequency and location of sunspot appearance during the solar cycle is nicely illustrated in the so-called butterfly diagram of Figure 4 that shows the latitude of the appearance of sunspots as a function of time.

The solar cycle marks the rise and fall in solar activity and it is not limited to a variation in the number of sunspots being observed. The rise on the number of sunspots being observed on the

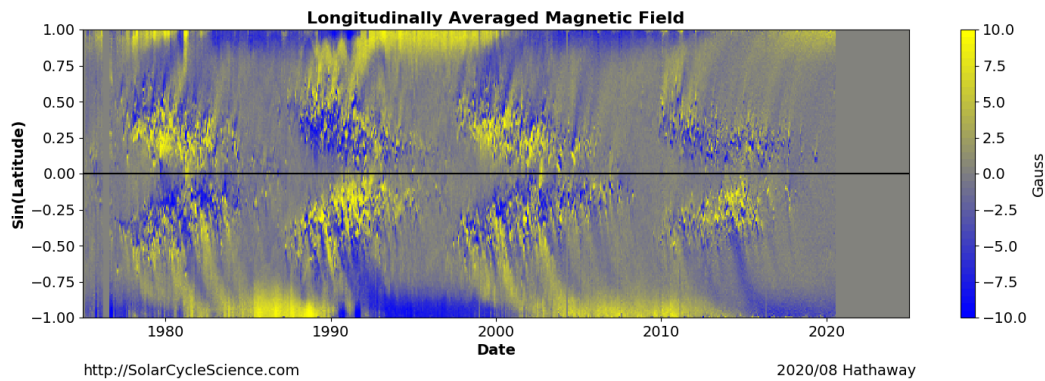


Figure 5: The magnetic butterfly diagram represents how the surface magnetic field is distributed over the solar cycle. Source: Solar Cycle Science <http://www.solarcyclescience.com/solarcycle.html>.

solar surface is followed by an increase in the emission of extreme ultraviolet and X-rays, and a higher occurrence of CMEs and flares. Additionally, an inversion in the magnetic field polarity takes place over an 11 years period as represented in Figure 5.

Using the historical data to study different solar cycles it was possible to spot some of the long term variability in the solar cycle, one of the most prominent examples being the Maunder minimum that lasted from 1645 to 1715. The Maunder minimum is the only grand minimum of activity period for which there are registers of observations made with telescopes. During the Maunder minimum, the solar activity was greatly reduced and no sunspot could be directly observed, while at the same time significantly lower temperatures were being observed on Earth. For this reason, the period over which the Maunder Minimum lasted for is also known as “the little ice age” and it is still being studied to better understand and evaluate how low the activity levels really were when compared to the long term variability on solar activity and how these variations can impact the Earth climate (see; Usoskin et al., 2015; Owens et al., 2017). In a more broad context, Arlt and Vaquero (2020) bring a review about the historical sunspot records and how the definition of sunspot changed over time, while a review about the solar cycle can be found in Hathaway (2015). Petrovay (2020) brings a review paper with the predictions for the solar cycle 25 which, as of this writing, has just started.

As instrumentation advances, powerful telescopes with the likes of GREGOR (Dominguez-Tagle et al., 2017) and DKIST (Tritschler et al., 2016) allow the study of small scale features of the solar atmosphere. However, exploring these details in the magnetic structure of an AR is out of the

Table 1: Mt. Wilson classification rules.

Class	Feature/classification rule
$\alpha$	A single dominant spot often linked with a plage of opposite magnetic polarity
$\beta$	A pair of dominant spots of opposite polarity
$\gamma$	Complex groups with irregular distribution of polarities
$\beta\gamma$	Bipolar groups with more than one clear North – South polarity inversion line
$\delta$	Umbræ of opposite polarity together in a single penumbra

scope of this work.

## 1.2 The Mt. Wilson classification

The idea of classifying sunspots according to their morphology started with Hale et al. (1919) who observed that sunspots could have different polarities and attempted to explain how these polarities are distributed in ARs. With the data of daily sunspot observations, two systems have emerged since then: the Mt. Wilson classification (Smith and Howard, 1968) and the McIntosh classification (McIntosh, 1990). These eventually formed a standard that is used today for producing the National Oceanic and Atmospheric Administration (NOAA) reports on solar observations.

The Mt. Wilson classification, which received its name after the observatory where the researchers that developed it were based, is an updated version of the classification proposed by G. Hale (Hale et al., 1919) and classifies the magnetic field distribution of sunspot groups according to their polarity and complexity of spatial mixing. Although the Mt. Wilson classification describes sunspot groups in a limited way it is enough to classify every group (Jaeggli and Norton, 2016). The Mt. Wilson classification is relatively simple and its decision rules are summarized in Table 1.

The McIntosh classification was developed as a tool for flare forecasting as the system was developed to classify sunspot groups based on earlier works that studied flares in a statistical sense (Waldmeier, 1938; Giovanelli, 1939; Smith and Smith, 1963) which highlighted that flares tend to happen close to complex sunspot groups. The McIntosh scheme then introduced 60 different types of sunspots based on the combinations of the different parameters used to perform the classification. Although the McIntosh classification is capable of classifying ARs taking into account considerably more details of their morphology, the number of possible classifications is large when compared to the sample size used to produce the results featured in this work. For this reason, de-

spite keeping track of their McIntosh class, the discussion contained here uses the Mt. Wilson classification to classify the ARs. Details about the data used here are given in Chapter 2.

### 1.3 Active regions and the overlying field

It can be clearly seen in images containing magnetic field measurements that the magnetic structure of sunspots can cover large amounts of area over the photosphere. It can also be seen that by observing the solar plasma at different temperatures, as in the Atmospheric Imaging Assembly (AIA, Lemen et al., 2012) observations in Figure 6, the magnetic structure on the surface can reach out far above the photosphere stretching itself over the other two layers that compose the solar atmosphere which are the chromosphere and the corona. The magnetic field structure can be thought as if it is forming “an almost horizontal canopy with a base in the middle or upper photosphere” (Solanki, 2002). The entirety of the magnetic structure that is spanned by the sunspot, from the photosphere to the corona, including the sunspot form an active region (AR).

The intense magnetic fields of ARs make them capable of storing vast amounts of energy depending not only on how intense the magnetic field is but also on how its three dimensional structure is organized. ARs and their evolution are linked to most large scale energetic events that take place in the Sun such as flares and coronal mass ejections (CMEs). A review on flare producing ARs can be found in Toriumi and Wang (2019). The main focus of this thesis will be on answering the question of how energy is injected and removed in ARs at photospheric level.

The magnetic field topology can be indirectly observed, as in Figure 6, since the charged particles in the plasma that compose the solar atmosphere will keep their movement in an orbit along any existing magnetic field line on its path. Then, with instruments such as the AIA which are capable to observe the Sun in seven extreme ultraviolet (EUV) channels, pictures of the plasma on different heights of the solar atmosphere are used to indirectly show the magnetic field structure. Unfortunately, measuring the magnetic field using the Zeeman effect to study the corona in detail is considerably harder than in the photosphere. Observing the corona directly is particularly challenging as the layer is optically thin. Also, the magnetic field in the corona is considerably weaker ( $\sim 10$  G) than in the photosphere. Coronagraphs, that are designed to observe the corona, must use a physical device to block the direct light coming from the photosphere so only the outermost part

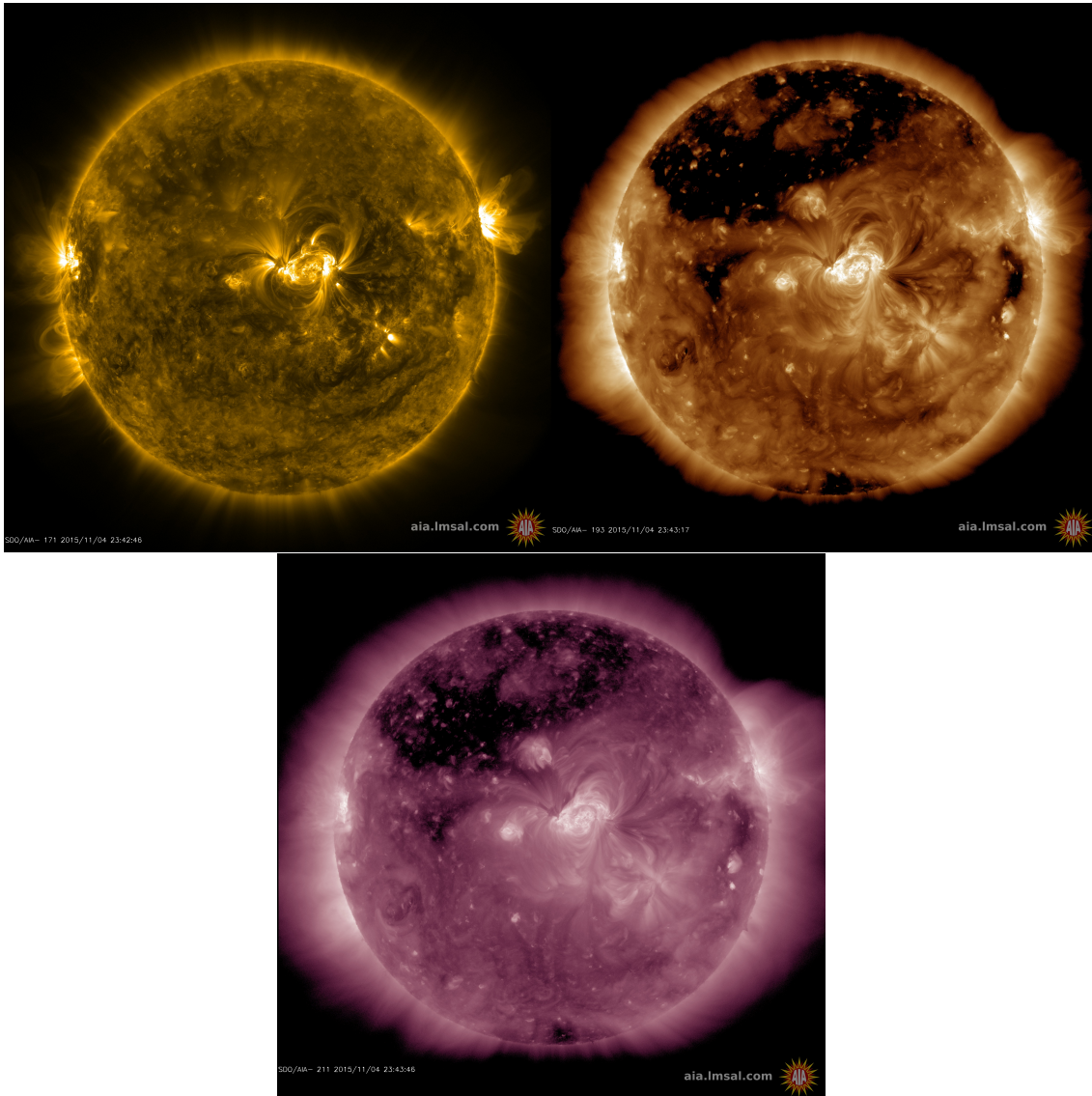


Figure 6: The solar plasma in the corona as observed by the AIA 171Å (top left), 193Å (top right) and 211Å (bottom) at 2015-11-04 23:43. Source: LMSAL Sun today.

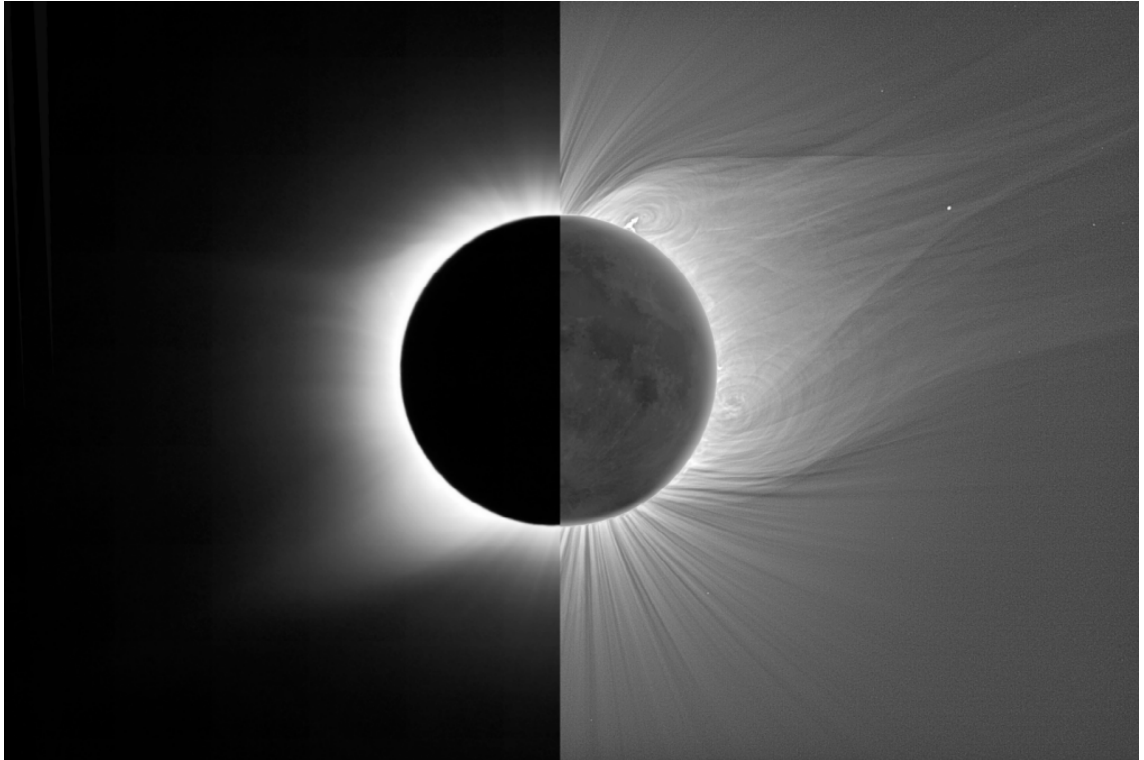


Figure 7: Picture of the solar corona in white light (left) and the same picture after digital enhancement. Source: Rušin et al. (2010)

of the corona can be seen. Currently the “viable” alternative to make use of an artificial block to reduce the effects caused by the Sun glare is taking measurements during a solar eclipse. Despite producing unique results, as shown in Figure 7, these simply don’t happen often enough to be practically useful.

The lack of direct measurements of coronal magnetic fields does not mean that the 3D magnetic structure cannot be studied. The coronal magnetic field can be modelled from measurements made at the photospheric level by employing magnetic field extrapolations, as proposed by Nakagawa et al. (1973). Magnetic field extrapolations assume that the plasma motions are dominated by magnetic forces since where the plasma pressure is small when compared to the magnetic forces and such a field is said to be force-free. Since the ratio between plasma and magnetic pressure (i.e., plasma  $\beta$ ) in the Corona is small assuming a force-free field is a suitable approximation for coronal fields. Considering a force-free field (i.e.,  $\mathbf{J} \times \mathbf{B} = 0$ ) lying above a boundary surface such

as the photosphere, the magnetic field in the overlying volume will follow (Régnier, 2012),

$$\nabla \times \mathbf{B} = \alpha \mathbf{B},$$

$$\mathbf{B} \cdot \nabla \alpha = 0,$$

$$\nabla \cdot \mathbf{B} = 0,$$

where  $\alpha$  is the ratio of vertical currents and vertical field,

$$\alpha = \mu_0 \frac{J_x}{B_x} = \mu_0 \frac{J_y}{B_y} = \mu_0 \frac{J_z}{B_z}.$$

In this scheme, magnetic field extrapolations are divided into three categories based upon how they treat the existence of electric currents. A potential field extrapolation is the case for  $\alpha = 0$ , from which it is clear that there are no currents (i.e.,  $\mathbf{J} = 0$ ). If  $\alpha$  is non-zero and has a constant value for the entire volume, then  $\mathbf{J} = \alpha \mathbf{B}$  which is referred to as a linear force-free extrapolation. However, if  $\alpha$  is allowed to vary spatially throughout the volume then  $\mathbf{J} = \alpha(x, y, z) \mathbf{B}$  which is referred to as a nonlinear force-free extrapolation.

Obviously, since the idea of extrapolating the magnetic field from photospheric observations was proposed both computational resources and mathematical methods used to perform the calculations saw a considerable development, improving the capacity to obtain more accurate reconstructions of the field. However, the complexity of the electric currents and plasma movement on the solar surface is still beyond what can currently be replicated and still represents a daunting challenge to overcome. Discussing magnetic field extrapolations in detail is beyond the scope of this work, but reviews of the topic can be found in Régnier (2013) and Wiegelmann et al. (2017), while Warren et al. (2018) presents a comparison between the performance of different models.

Since the complexity of the magnetic field topology (including how much the magnetic field lines are twisted) is of great importance to the evolution of an AR, it is then useful to keep track of how complex the AR magnetic structure is. In this sense, magnetic helicity can be used to measure the complexity of the field which can be calculated over the whole volume occupied by it and also over a single field line (Moraitis et al., 2019). The magnetic helicity ( $H$ ) can be calculated as the integral over the volume ( $V$ ) of the dot product between the magnetic field ( $\mathbf{B}$ ) and the vector

potential ( $\mathbf{A}$ ),

$$H = \int_V \mathbf{A} \cdot \mathbf{B} dV. \quad (1.1)$$

Under ideal magnetohydrodynamics conditions, magnetic helicity is conserved (Woltjer, 1958). However, during a magnetic field reconnection, that may not be the case depending on whether or not a CME happens as a result of the reconnection. If a magnetic field reconnection result in a flare only the field energy can be minimized while the helicity is conserved thorough a turbulent process of relaxation of the field lines (Taylor, 1974; Diamond and Malkov, 2003). Now if the magnetic field reconnection results in a CME, part of the field is ejected and then helicity is also removed from the system. However if one looks at the bigger picture of the solar system (the entire Heliosphere) considering the solar dynamo, ARs, CMEs and magnetic clouds in the interplanetary space helicity conservation can be effectively tracked (Berger, 2005). The build up or removal of helicity ( $\dot{H}$ ) over a surface ( $S$ ) in the photosphere can be calculated as (Berger and Field, 1984; Kusano et al., 2002),

$$\dot{H} = 2 \int_S \mathbf{A}_p \times (\mathbf{V} \times \mathbf{B}) \cdot \mathbf{n} dS = \dot{H}_t + \dot{H}_n, \quad (1.2)$$

where  $\mathbf{A}_p$  is the vector potential of the potential magnetic field,  $\mathbf{V}$  is the surface velocity and  $\mathbf{n}$  is the surface normal. Changes in helicity can then be separated depending on the type of surface motion that is being observed, where  $\dot{H}_t$  and  $\dot{H}_n$  are representation of the contributions given by, respectively, shearing ( $\mathbf{V}_t$ ),

$$\dot{H}_t = -2 \int_S (\mathbf{A}_p \cdot \mathbf{V}_t) \mathbf{B}_n \cdot \mathbf{n} dS, \quad (1.3)$$

and emergence ( $\mathbf{V}_n$ ) motions,

$$\dot{H}_n = 2 \int_S (\mathbf{A}_p \cdot \mathbf{B}_t) \mathbf{V}_n \cdot \mathbf{n} dS. \quad (1.4)$$

Equations 1.3 and 1.4 are calculated similarly to the energy injection, which is the focus of this work, and will be explored later. When observing the photosphere, upflows and downflows of plasma are emergence motions ( $\mathbf{V}_n$ ). Since magnetic structures are move along with the plasma, there is also an injection or removal of magnetic field associated to these motions. The shearing motion ( $\mathbf{V}_t$ ) is then accounting for plasma movement along the solar surface and can also be referred to as horizontal plasma motions. The phrase “shear motion” can cause some confusion as it is not the same as magnetic shear that a group of magnetic field lines can be subjected to,

although the horizontal motion of magnetic footpoints can cause the magnetic field to shear (Wang, 1994).

One of the benefits of being able to extrapolate the magnetic field is that it becomes then possible to calculate the energy that is stored in its whole volume. The magnetic energy stored in a magnetic field over a volume can be calculated as,

$$E = \int_V \frac{B^2}{2\mu_0} dV. \quad (1.5)$$

Since the potential field represents the minimum energy state of the magnetic field, any surplus compared to it must be what an AR has available to release in an event, known as the energy budget. Then, an upper bound for the energy budget can be estimated using Equation 1.5 by subtracting the energy obtained with the estimated magnetic field from different extrapolation methods. However, there is a difference between the calculations of the energy budget for a CME,

$$E_{\text{budget}}^{\text{CME}} = E_{\text{nff}} - E_{\text{pot}}, \quad (1.6)$$

and for a flare,

$$E_{\text{budget}}^{\text{flare}} = E_{\text{nff}} - E_{\text{lff}}, \quad (1.7)$$

where  $E_{\text{pot}}$ ,  $E_{\text{lff}}$  and  $E_{\text{nff}}$  are the energies calculated from the magnetic field obtained from the potential, linear force-free, and non-linear force-free extrapolations, respectively. This difference is due to the role of helicity in the process. For CMEs, part of the field is ejected so helicity is not conserved and the energy budget is calculated in relation to the potential state. For non-eruptive flares, helicity is conserved so the field can only relax towards a linear force-free state.

## 1.4 Flares

Despite registers of solar observations, including sunspot observations, being dated back to 800 B.C. (Arlt and Vaquero, 2020), the first observation of a solar flare was made by Richard Christopher Carrington and Richard Hodgson in 1859, already in the telescope era. The telescopes used by Carrington and Hodgson were observing the Sun in the white-light continuum when the flare took place and prompted a new era of investigations in solar phenomena. With access to consider-

ably better instrumentation, it is now possible to know that a flare as intense as the one observed by Carrington and Hodgson, is actually a rare event (Riley, 2012) and they release considerably more energy than the flares that are usually observed in the Sun. The modern telescopes that are used to observe and study flares, such as GOES or AIA, use measurements of the soft X-ray flux or take images of the Sun in the EUV part of the spectrum where flares that are not intense enough to be visible in white light can be promptly seen in these wavelengths.

A flare happens when magnetic field lines undergo a process of reconnection that results in the sudden release of large amounts of energy. Part of the magnetic energy that is impulsively released cause the coronal loops to heat resulting in an abrupt increase in the intensity of the light emitted by the region which is one of the observational signatures of a flare and is illustrated in Figure 8. The flare as a phenomenon is better defined as not only the brightening of the coronal loops but as the whole process from the energy release to the brightening of the coronal loops.

Observing the curves produced in the soft X-ray flux it can be seen that a flare happens on a timescale that may vary from a few minutes to hours where the flare undergo different phases. First there is the pre-flare phase where the X-ray flux stays at a background radiation level. This can be seen in Figure 8 before the light curve start to climb. The build up is known as impulsive phase where, as the name suggests, energy is being impulsively released which makes the X-ray flux peak. How high the measured peak reaches will define the flare class as it is promptly seen in the top panel of Figure 8. Finally, there is a recovery phase, that may last hours, where the emissions go back to pre-flare levels.

The intensity of a flare is currently classified depending on the peak of the soft X-ray flux integrated over 1-8 Å as measured by GOES (Toriumi and Wang, 2019). There are five different classes used to describe a flare according to the power of their emission at Earth, separated according to the order of magnitude of the emission. The classes are: A ( $10^{-8} \text{ W m}^{-2}$ ), B ( $10^{-7} \text{ W m}^{-2}$ ), C ( $10^{-6} \text{ W m}^{-2}$ ), M ( $10^{-5} \text{ W m}^{-2}$ ) and X ( $10^{-4} \text{ W m}^{-2}$ ). The letters are just an encoding of the orders of magnitude of the emission and to tell precisely where a flare stand in this scale they are also accompanied by a number that goes from 1 to 9.9 (i.e., a M4.3 flare is a flare with  $4.3 \times 10^{-5} \text{ W m}^{-2}$ ). Cliver and Dietrich (2013) estimates that the event observed by Carrington and Hodgson would have been as high as X45±5 on the GOES classification which is still quite above the most recent extreme event on 4th November 2003 where the GOES classification was X35±5.

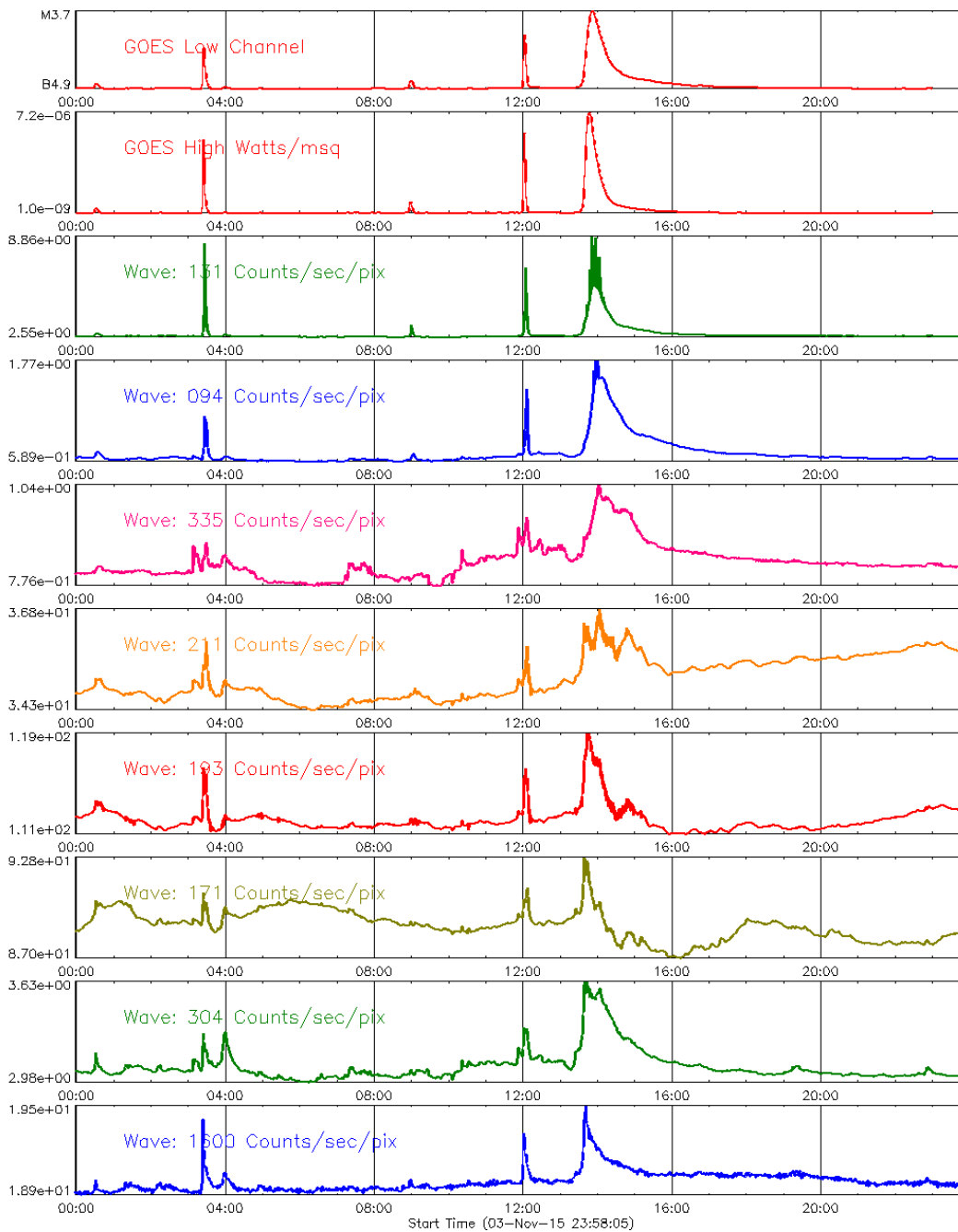


Figure 8: GOES and AIA measurements for different wavelengths on 2015-11-04 when NOAA 12443 produced a sequence of flares including a M-class flare. Source: LMSAL Sun today

While flares are large scale events, nanoflares are much smaller and localized releases of energy that happen in bursts of  $\sim 10^{24}$  erg (Parker, 1988). On the other extremity there are super flares and the ones produced by other G-type stars can release a total bolometric energy ranging from  $10^{29}$  to  $10^{32}$  erg (Maehara et al., 2012).

Flares are energetic events that are a result of a magnetic reconnection process that occurs in the

magnetic structure of ARs being then more frequently observed during the solar maximum. In the solar minimum, where few or no ARs at all are observed in the solar disk, flares are then not commonly observed. To estimate how frequent are energetic events, Schrijver et al. (2012) conducted an investigation of energetic events using solar, stellar, lunar, and terrestrial records and shows that the frequency of flares can be approximated by a power law with the frequency of an event decreasing with the magnitude of the event.

Now, if the number of flares reported by GOES is actually counted over a period of time, the number of B- and A-class flares will be smaller than the number of C-class flares which is an apparent contradiction to the reports of Schrijver et al. (2012). During the solar cycle the background radiation level also varies and sometimes, it can be seen in the first panel of Figure 8, it lies above what is produced by a B class flare. GOES then cannot detect the peaks in soft X-ray flux and register the flares that have a flux below the background radiation level.

As discussed in Benz (2017), one of the first challenges faced by the scientific community was to define what a flare is and some of the earlier definitions for a flare made it difficult to draw a distinction between a flare and a CME as, among other factors, the word eruption was being used to describe the flare. CMEs are also a consequence of magnetic field reconnection, which is why more often than not mid-/large-magnitude flares are followed by CMEs (Andrews, 2003), but CMEs are caused when part of the magnetic field (and therefore part of the plasma filament) is ejected during the reconnection. All the particles that were orbiting the ejected field are released with it so, essentially, a CME is the result of magnetic energy being converted to kinetic energy and potential gravitational energy lifting the CME from the solar atmosphere. Aschwanden (2016) found that the mass ejected during a CME is between  $0.1 \sim 30 \times 10^{15}$  g and the expansion speeds range from  $100 \text{ km s}^{-1}$  to  $3000 \text{ km s}^{-1}$ .

In studying how the magnetic energy is distributed in two different X-class flares that were accompanied by CMEs, Emslie et al. (2005) found that the largest share of the energy in the events is released as kinetic energy in the CME. However, the uncertainties shown in their analysis make it possible that both flare and CME have a comparable contribution in the energy dynamics of the overall event. Emslie et al. (2005) found that the integrated radiated energy measured with GOES soft X-ray flux amounted to  $5.4 \times 10^{30}$  ergs, while the total radiant energy is on the order of  $10^{32}$  erg which is in the same order of magnitude of the energy released in the acceleration of

the CME.

In the SDO-era, works as Aschwanden et al. (2014) and Aschwanden (2016) extended the understanding on the energetic of flares and CMEs by presenting studies covering hundreds of events. Aschwanden et al. (2014) found that the magnetic fields in the regions that produced the events had a total potential energy ranging from  $1 \times 10^{32} - 4 \times 10^{33}$  erg. The non-potential energy estimated through magnetic field extrapolations was on average 7% larger than its potential counterpart, but this ratio between the two energies can be quite contrasting depending on the region as the ratio was found to vary from 0.4% to 25%. The energy dissipated during solar flares, calculated by comparing the free energy in time, varies from 20% to 80% and scales accordingly to the potential energy. Aschwanden (2016) found that CMEs can release  $10^{28} - 10^{33}$  erg. Later, Aschwanden et al. (2019) adds that the total dissipated magnetic energy largely exceeds the thermal and nonthermal energy in flare events, which shows that the energy released during the magnetic reconnection is, as expected, enough to produce flares.

Flares that release more than  $10^{33}$  erg are known as super flares. Schaefer et al. (2000) found 9 occurrences of flares in solar-type stars with the energy released in some of these events reaching  $10^{38}$  erg. Maehara et al. (2012) investigated how often these flares happen on solar-type stars and found 365 occurrences in 148 different stars where the total bolometric energy released in each of those events was found to range from  $10^{33} - 10^{36}$  ergs. Also, solar-type stars that are younger than the Sun were found to produce superflares more frequently, but stars that are similar to the Sun release a comparable energy during super flares to their younger counterparts.

A superflare has not been produced by the Sun in over 2000 years (Schaefer et al., 2000). The largest flare produced by the Sun in the recent history was the one observed by Carrington that is estimated to have released  $10^{32}$  ergs (Tsurutani et al., 2003). Still, this flare was an order of magnitude short of being considered a superflare.

Schaefer et al. (2000) makes a discussion about the possible consequences that a superflare may cause to a planet. The authors estimate that a flare with  $10^{35}$  ergs would cause a flux of  $3.5 \times 10^7$  ergs  $\text{cm}^2$  in a planet located at 1 AU from the star. At a planet surface level Schaefer et al. (2000) point out that while this flux is too small to cause geophysical effects such as rocks melting, icy surfaces could see a large-scale melting. For the atmosphere the consequences will largely

depend on its structure but the possible effects include: temporary heating, worldwide aurora, temporary breakup of the ionosphere, and ozone depletion. This analysis does not take into account possible damages that a super flare could cause in the infrastructure that would then lead to disruptions, economic damages and life loss.

These effects would correspond to more significant energetic impacts on other planets that rise from more active stars. The Earth also experiences the effect of the solar activity and it can lead to a diversity of consequences. Many of these consequences are linked to mankind scientific development such as the electric grid or the global position system (GPS). Then, the technological advance of humankind also increases the demand to forecast these events and how they will affect the near Earth space. The set of conditions driven by the solar activity that affects the space within the solar system and bodies therein form what is known as space weather.

## **1.5 Space weather**

In the 20th century with the invention of radio and radar it became possible to clearly notice that flares and CMEs are far from being just a phenomenon that takes place in the Sun, as disturbances in telecommunications started to be linked to the observation of flares and CMEs.

During the space race period when the spacecrafts became powerful enough to reach heights above the magnetosphere it was proved that the Earth was in the constant influence of the solar wind, an idea that was initially proposed by Parker (1965). By then, with the magnetosphere shielding the Earth against the solar wind, most of its impact was then believed to be relevant only to the spacecrafts that flew beyond its protection. With the increasing amount of technology that depends on data gathered by satellites to conduct ground-based operations, the effect that solar activity has on a spacecraft is becoming more relevant to daily life. GPS is probably one of the best examples, with the whole of aviation making extensive use of these instruments and need a high degree of accuracy to keep their operations running smoothly.

Although the Earth's magnetic field can offer some degree of protection to the Earth from the effects of the solar wind and CMEs, the disturbances caused in the magnetic field can propagate to the surface. Temporary disturbances in the Earth's magnetic field are known as geomagnetic storms (Gonzalez et al., 1994) and are measured in cooperation by different observatories around

the globe and these measurements are mapped back to indexes of disturbances (e.g., the Dst index).

Disturbances in the geomagnetic field are known to induce currents and increase the heat in the ionosphere (Chapman, 1937; Chapman and Ferraro, 1940) which can lead to disruptions into communications systems such as the radio and also in radar systems. Solar flares cause the side of Earth's ionosphere that is facing the Sun to increase its temperature which then affects its ionization and density. This can affect radiation travelling through this layer, such as radio waves, which make flares particularly disruptive to communications (e.g.; Hayakawa et al., 2019).

Geomagnetically induced currents (GICs) are a consequence of the interaction between the geomagnetic field, the magnetic field of CMEs and the magnetized solar wind (Schrijver and Mitchell, 2013). These currents can affect the power grids during a period of strong geomagnetic activity and were found to account for about 4% of the disturbances in the US high-voltage power grid (Schrijver and Mitchell, 2013; Schrijver et al., 2015).

One of the most known examples of how disturbances affect the modern world happened in Quebec on 13th March 1989 where a severe geomagnetic storm caused a blackout that lasted for more than 9 hours. With the increasing dependence that human life has on technology, the potential economical and life losses that geomagnetic storms can cause rose significantly prompting governments to invest more in contingency plans (e.g., Bolduc, 2002; Schrijver et al., 2015; Singer et al., 2019; Spann et al., 2019) and in the agencies that monitor and provide forecasts of space weather. Accurate forecasts for energetic events allow the administration of key infrastructure, for example the electrical grid, to prepare for the event. Schrijver et al. (2015) point out that forecasts being more than 12 hours ahead of a magnetic structure of a CME arriving are essential to prepare the infrastructure.

A diversity of different parameters is used to measure and evaluate the solar-terrestrial conditions. Some of these parameters are: the geomagnetic indexes (Kp-Ap) that quantifies disturbances in the geomagnetic field, the total electron content in the ionosphere, the solar wind speed and magnetic field, CMEs arrival time and also the number and class of flares taking place in the solar surface. These measurements are also used as entries for models that try to forecast the solar-terrestrial conditions.

Camporeale (2019) reviews how recent improvements in machine learning and artificial intelligence, boosted by the development of more powerful and accessible Graphics Processing Units (GPUs), are impacting the development of new (and upgrade of existing) space weather prediction models. For solar flare forecasts, Camporeale (2019) points that most models are using features extracted from images as an input to their forecast models and they are “not embracing a full black box approach” when it comes to using machine learning tools. The accuracy of the models discussed by Camporeale (2019) are mostly below 80% but the author also points out that there are only a few years worth of data that are being continuously produced by SDO which is now close to covering a full solar cycle. This “modest” data coverage brings to question if the data gathered so far is adequate for machine learning purposes that mostly prevail over other statistical methods when the datasets are vast.

Space weather models can benefit from data from different missions which results on the models having a multitude of parameters, that are derived from the data, available to consider when trying to issue a forecast. However, selecting which parameters are more important and which can be overlooked is a rather daunting task, as shown by Leka and Barnes (2003). As of now, models that try to differentiate flaring and non-flaring ARs do not usually track or take into consideration the energy evolution of the ARs. A better understanding of how energy is injected and accumulated, and also how it evolves in ARs with different levels of flaring activity, should then provide models with a new set of more physically meaningful parameters that could potentially be used in the future to improve flare forecasting models.

## **1.6 Active region energy injection/removal**

As discussed throughout this Introduction chapter, ARs are the solar structures that span the most prominent solar energetic events but, so far and on purpose, discussions about the energy dynamics of ARs have been neglected in this work. Achieving a better understanding of the energy dynamics of ARs at the photospheric level and exploring if it is directly connected to flares is the core objective of this work. Then, in this last section of the introductory chapter, some general points on the injection and removal of energy in ARs are discussed so that more specific discussions can be made in the following chapters where appropriate.

Understanding the energy dynamics of the Sun is basically a task of tracking how the energy produced in the core through nuclear fusion is changing as it propagates outwards. While propagating the energy may change form, e.g. magnetic energy being dissipated into heat, or intensity through absorption and emission while interacting with matter present along its path. Defining the boundaries where the energy transfers and changes are being studied is then a fundamental step as in principle those changes could be followed indefinitely. This thesis focuses on the energy dynamics at the photospheric level with the lower boundary being the top of the convective zone and the upper boundary the chromosphere and lower parts of the corona.

The mechanisms that allow energy to propagate may also vary depending on the layer that is being studied. Since the photosphere is located just above the convective zone the energy between these two layers is changed via plasma emergence and submergence. With the magnetic structures frozen in the plasma that is being exchanged between the photosphere and convective zone, that brings a direct change of magnetic energy between the layers. The total energy stored in a magnetic field can also be changed depending on how field lines are twisted due to their footpoint motions. Considering that these field lines stretch from the photosphere into the overlying corona, horizontal plasma motions at the photospheric level can therefore change the energy content of the overlying atmosphere (i.e., the movement of footpoints will then affect the amount of non-potential energy in the magnetic field).

The energy injection and removal then happens at the photospheric level in a similar way to what is observed for helicity with the plasma motions and the magnetic structures frozen into it, acting to change the amount of energy in the entirety of the magnetic field. The energy changes through the photosphere, also known as the photospheric Poynting flux, can nowadays be directly studied as the measurements of the magnetic field vector on the photosphere were made regularly available by the HMI instrument and science team. The Poynting flux is covered in depth in Chapter 3.

The changes in energy caused by the movement of the photospheric plasma can be indirectly measured using magnetic field extrapolations as that would ultimately allow the tracking of the energy content over time. These studies also received major contributions from the HMI data as some extrapolations are only possible to be obtained by having the full magnetic field vector to extrapolate the field from. Sequences of magnetic field vector images can also be used to calculate the plasma velocity as the magnetic structures are moving with it. However, the HMI coverage

for the magnetic field vector that allowed studying plasma velocities in greater detail is still fairly recent, dating back to 2012 and the exploration of all these vector magnetic field data are surely far from the end.

The main aim of this work is to deepen the understanding of the role that flux emergence and shear flows have in the process of energy injection within ARs. This will be done by comparing the behavior of flux and shear flows and the consequences they have on the evolution of different ARs. To achieve this goal, analysis of flux emergence and shear flows was conducted on a set of 51 ARs including flaring and non-flaring regions, focusing on how the characteristics of these processes contribute to any energetic events that take place. The comparison of the results obtained for ARs of different sizes/fluxes, evolutionary phases and magnetic configurations show the broader context of how flux emergence and shear flows affect energy injection within ARs. Then this thesis should provide a definitive benchmark for future studies of photospheric flows within ARs since no other works perform such analysis and compare the results for a large number of ARs. The next paragraph will outline the contents of the remaining chapters of this work.

Chapter 2 explains how magnetic fields are measured in the solar surface and walk the reader over the instrumentation used in this work. Chapter 3 discusses the specifics of the Poynting flux at the photosphere showing the relevant equations that are used to process the data. Chapter 4 first explains how the plasma velocity can be obtained from images of the photospheric magnetic field vector and then walks the reader on how the data was processed and stored to later produce the results featured in the following chapters. Chapter 5 compares the Poynting flux for a set of 8 ARs, 5 non-flaring and 3 that produced different levels of flaring activity, profiling the Poynting flux at pixel level and comparing the Poynting flux of the flaring ARs against the non-flaring ones. Chapter 6 make use of the complete dataset to investigate the contribution of emergence and shearing motions to energy injection and also profiles the Poynting flux according to the ARs Mt. Wilson class in different timescales. Chapter 7 explores the differences in the Poynting flux for regions of varying flaring activity, the existence of timescales linked to the pre-flare energy build-up and investigates how each manifestation of energy injection is linked to the events. Finally, Chapter 8 brings the conclusions and also suggestions of future works that could be carried on to further extend the contributions of this work.



## Chapter 2

# Instrumentation and data sources

This chapter first introduces the physical principles that make it possible to measure the magnetic field in the solar atmosphere so that later in this text it can be discussed how SDO/HMI produces the vector magnetic field images that are one of the main data products that make works like this possible. HMI data is available in different versions based on the measurements and are organized in data series that receive different levels of pre/post-processing before being published. Following an initial discussion, some details about the specific data series that is being used will be presented to justify why this particular series was chosen. Another building block of this thesis is all the information in the daily reports of solar activity produced from ground-based observatories and made available by the Space Weather Prediction Center (SWPC) that is part of the National Oceanic and Atmospheric Administration (NOAA). The reports made available by SWPC are the source of the meta data that are used to label regions according to their Mt. Wilson class. The discussion on why and how these reports are used here are the last section of this chapter.

## 2.1 Spectropolarimetry

### 2.1.1 The Zeeman effect

As mentioned in Chapter 1, the discovery of the Zeeman effect (Zeeman, 1897) made it possible to measure the magnetic field in the Sun using observations from telescopes by studying the effect the magnetic field has on the spectral lines (see Figures 10 and 9).

The Zeeman effect measures the magnetic field by looking at how the degeneracy of energy states in an atom is broken in the presence of a magnetic field, which leads the spectral lines to appear blurred and, if the field is strong enough, split into components.

Emission lines are the signature of the light emitted by an electron when it changes energy states towards the ground state which then affect the electron total angular momentum. The wavelength displacement ( $\Delta\lambda_{\sigma^\pm}$ ) caused in the components of a emission line due to the presence of magnetic field of is given by,

$$\Delta\lambda_{\sigma^\pm} = \pm g_{\text{eff}} \frac{e\lambda_0^2}{4\pi m_e c} B, \quad (2.1)$$

where  $e$  is the electron charge,  $m_e$  is the electron mass,  $c$  is the speed of light,  $B$  is the magnetic field magnitude,  $\lambda_0$  is the original wavelength of the observed line and  $g_{\text{eff}}$  is the effective Landé factor of the line. Considering a Zeeman triplet, where a line breaks into three components, the unshifted component is referred as the  $\pi$  component and the components that are shifted are called the  $\sigma^-$  and  $\sigma^+$  components.

The Landé factor, which represents how sensitive an emission line is to the presence of a magnetic field, is associated with a perturbation in the electron energy state and, thus, can be expressed as a function of its total angular momentum ( $\mathbf{J}$ ), orbital angular momentum ( $\mathbf{L}$ ) and spin ( $\mathbf{S}_p$ ),

$$g_{\text{eff}} \equiv \frac{3}{2} + \frac{S_p(S_p + 1) - L(L - 1)}{2J(J + 1)}, \quad (2.2)$$

which shows that the sensitivity of an emission line to a wavelength displacement caused by the presence of a magnetic field depends on the element that is emitting the line. HMI produces its measurements using the spectral line from neutral Iron (Fe I) at 617.3 nm.

The definition of “normal” Zeeman split is based on the historical observations of an emission line being split into a triplet. This is shown in the first published solar observations of a Zeeman splitting (Hale et al., 1919) that are reproduced in Figure 9.

Oddly enough, when a case other than a line that is broken into a triplet is observed this is known as “anomalous” Zeeman effect, as illustrated in Figure 10. The number of components ( $N_{\text{comp}}$ ) a line can break into is a function of the magnitude of the total angular momentum ( $J$ ),

$$N_{\text{comp}} = 2J + 1 \quad (2.3)$$

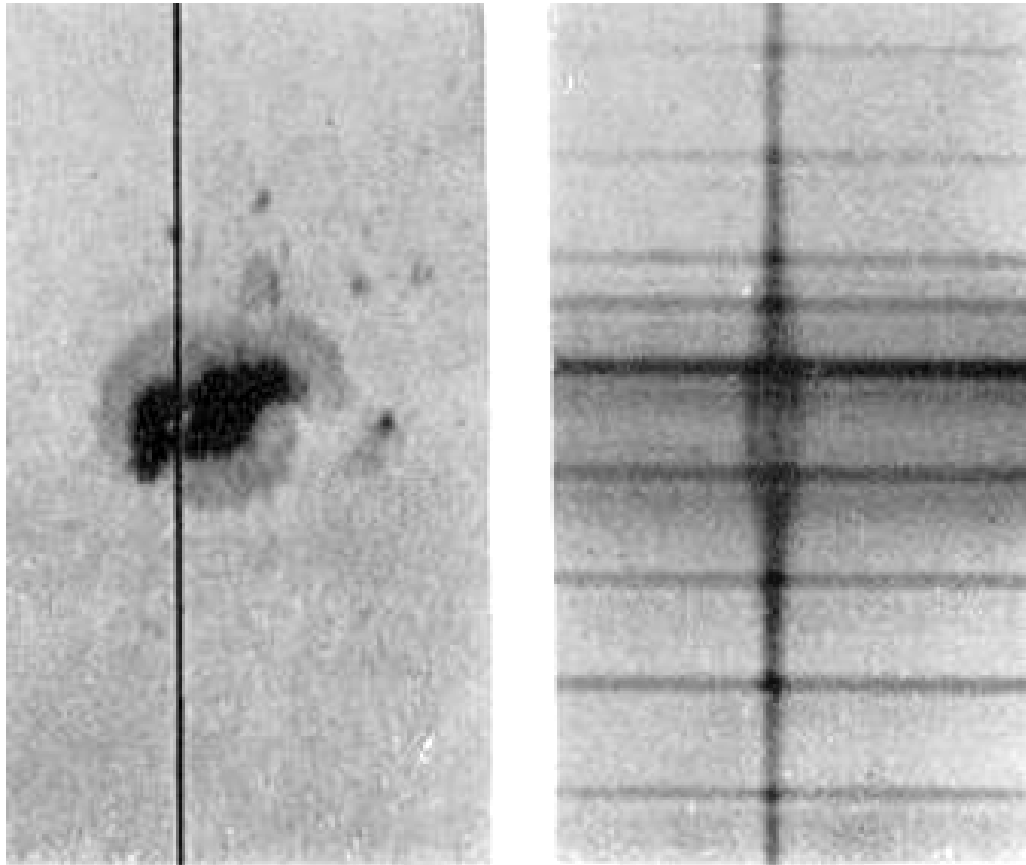


Figure 9: Left: The sunspot, seen in the continuum, where the spectral line observations studied by Hale were measured. Right: the triplet formed by the magnetic field effect in the Iron line  $\lambda$  617.3 nm. Source: Hale et al. (1919).

The triplet then will be the case for a transition between  $J = 1$  and  $J = 0$  or if the two energy levels have the same Landé factor in which case a single Landé factor can be used to calculate the splitting for the whole line. Generally, more than three lines are observed when a emission line is seen to split with the  $\pi$  and  $\sigma$  having two more sub components as illustrated in Figure 10. The total angular momentum of an electron ( $\mathbf{J}$ ) can be expressed as a sum of its orbital angular momentum ( $\mathbf{L}$ ) and spin ( $\mathbf{S}_p$ ),

$$\mathbf{J} = \mathbf{L} + \mathbf{S}_p . \quad (2.4)$$

Considering that the orbital angular momentum ( $\mathbf{L}$ ) and spin ( $\mathbf{S}_p$ ) depend on the atomic structure and each different element has its own unique structure, their emissions will show a different sensitivity to the presence of magnetic fields. It is quite remarkable to consider that the Zeeman effect discovery happened a few years before major scientific discoveries that started quantum physics being published forever changing how the atomic structure is understood.

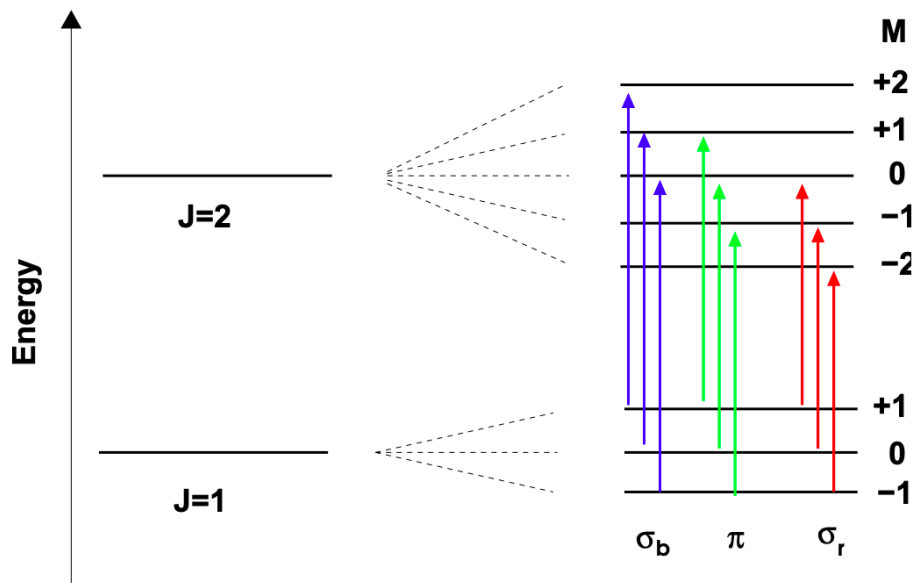


Figure 10: Illustration of a single emission line breaking into different components in the presence of a magnetic field. Source: Santiago (2004).

It is important to consider that the Zeeman effect cannot be calculated with the same degree of accuracy to every region of the solar disk. For example, in regions where the magnetic field is not intense enough to cause the Zeeman splitting to be larger than the Doppler width of a spectral line, the changes in the line caused by  $|B|$  are at or below noise threshold making it impossible to perform an accurate measurement.

### 2.1.2 The Hanle effect

When light is travelling from the source to the observer it interacts with the matter along its path through a combination of absorption, re-emission and scattering. These interactions between light and matter may impact not only the intensity of the light but also its polarization. Therefore, what is being observed often does not represent a faithful picture of the light source.

While spectroscopy occupies itself on studying the intensity of a light beam as a function of its wavelength, more information can be extracted from the object that is being observed if the polarization of the light spectrum is also taken into account. Changes in polarization and intensity of light can be used to unveil further details about the medium (i.e., the solar atmosphere) that is on the way between the source and the observer. Since the interactions between the light and the medium may cause the intensity and polarization of light to change, these changes can be traced

Table 2: A short comparison guide between the Zeeman and Hanle effects. Adapted from Ignace et al. (1997).

Parameter	Zeeman effect	Hanle effect
Line process	Emission or absorption	Resonance-line scattering
Polarization	Circular	Linear
Applicability	Zeeman shift $\gg$ natural line width	Zeeman shift $\sim$ natural line width
Observability	Zeeman shift $\geq$ doppler line width	Zeeman shift $\leq$ doppler line width
Field sensitivity	$B \geq 1\text{kG}$	$1\text{G} \leq B \leq 1\text{kG}$
Predominant over	Umbral	Penumbra

back to retrieve the original emission of the source using models of the atmosphere in order to draw an accurate picture of the source itself.

Part of the properties of the medium can be extracted using the Zeeman effect but the changes in polarization of resonance-line scattering when the source is subjected to a magnetic field are described by the Hanle effect (Hanle, 1925). The Hanle effect is particularly useful to perform measurements of the magnetic field as it is predominant in regions with weaker fields than what is necessary for the Zeeman effect to be observed. Also, the Zeeman effect will provide an accurate picture of the field by itself only for simple geometries of magnetic field as more complicated geometries would see cancellation in the polarization observed on the Zeeman components (Ignace et al., 1997). Table 2 illustrates in what conditions the Zeeman or Hanle effect is dominant for a given emission/absorption line.

While the Zeeman and Hanle effects can then account for the changes the light goes when exposed to magnetic fields they do not describe the different properties of intensity and polarization of the light beam that is being measured. Such a description, that provides the basic formalism that allows the original properties of the light source to be recovered, is given by the Stokes parameters.

### 2.1.3 The Stokes Parameters

The Stokes parameters are a set of four parameters (I, Q, U, V) that can be directly measured and completely describe the intensity and polarization of light as a function of the wavelength ( $\lambda$ ). The Stokes parameters are the basis of what is known as spectropolarimetry that studies the polarization state of light as a function of wavelength. The measurements of these parameters combined with a series of theoretical models of the solar atmosphere are, along with the Zeeman and Hanle effects, the physical principles that make it possible to study the solar (and stellar) atmosphere in greater

detail obtaining measurements such as the magnetic field of the solar surface.

In the sentences that follow there is a description of each of the Stokes parameters. For a more complete guide to spectropolarimetry one may refer to the works of Landi Degl'Innocenti (1992), Solanki (1993) and Landstreet (2015) and a description of a basic setup to measure the Stokes parameters can be found in Topasna and Topasna (2009). A masterclass on the subject can be found in del Toro Iniesta (2007).

Stokes I is simply a measurement of the intensity of light over a spectral range. Then, a basic property of Stokes I is that it is always larger than or equal to zero.

Since light can be linearly and/or circularly polarized the remaining three Stokes parameters (Q, U and V) are used to describe the polarization state of it. Stokes Q and U represent the fraction of the light intensity that is linearly polarized. Stokes V will account for the fraction of the light intensity that is circularly polarized. Changes in the polarization measured can also depend on the observer as illustrated in Figure 11 where how the observed Stokes Parameters profiles can change depending on the observer position in relation to the light source.

Commonly, the Stokes parameters are represented as part of the Stokes vector that contains the information from the four parameters in a column matrix,

$$\mathbf{I} = (I, Q, U, V)^T . \quad (2.5)$$

There are two properties of the Stokes parameters that allow relationships between the parameters to be established depending on light being completely polarized or unpolarized (see, Solanki, 1993). With the exception of cases where resonance lines are being observed close to the solar limb, in the absence of magnetic field  $Q = U = V = 0$  which ensures that the measurements of Stokes Q, U and V are directly related to the presence of magnetic features. In this case the Stokes vector resumes itself to Stokes I. In the case which light is completely polarized each parameter intensity can be calculated as a function of each other,

$$I^2 = Q^2 + U^2 + V^2 , \quad (2.6)$$

The Stokes parameters show distinct behaviours when being measured over different parts of a

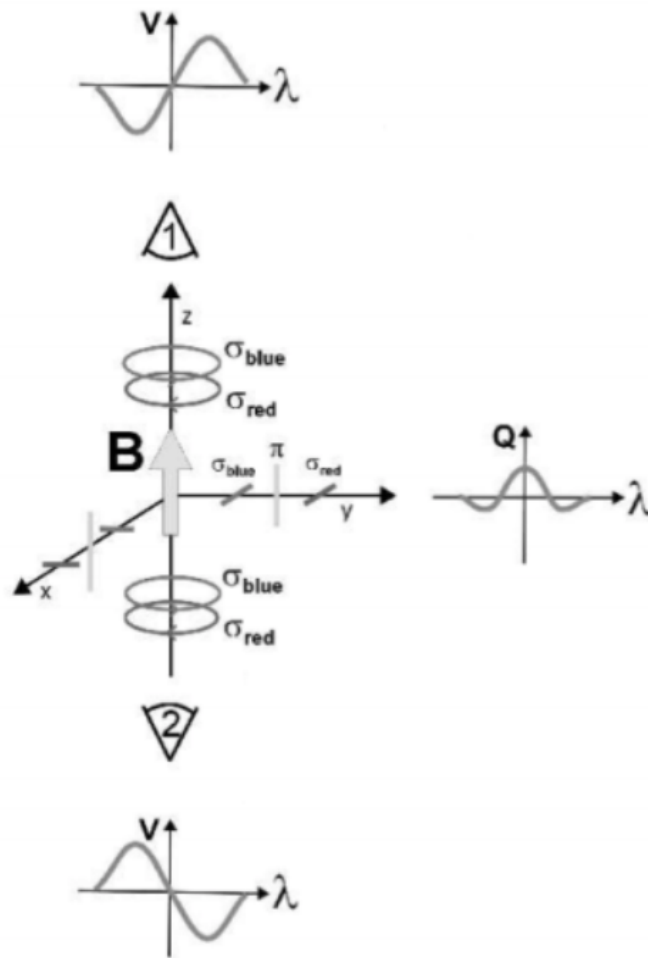


Figure 11: Changes in polarisation of light caused by the Zeeman effect. Source: Trujillo Bueno (2003)

sunspot as the structures that compose a sunspot have quite distinct magnetic field properties. When measured over the umbra of a sunspot, where the magnetic field is mostly vertical, Stokes V is dominant in relation to Q and U. Then, Stokes V profile shows a well defined shape as the portion of the magnetic field that is along the LOS introduces circular polarization via Zeeman effect. On the other hand, over the penumbra of a sunspot where the magnetic field is more oriented towards the solar surface, the polarization will be mostly linear which will cause Q and U to be dominant terms for polarization in the Stokes vector.

When measuring the Stokes parameters over different wavelengths, which is equivalent to say over the height of the solar atmosphere, the Stokes profile of each parameter for every image pixel is obtained. The Stokes profiles in Figure 12 show the signature shapes of every Stokes parameter as measured by Hinode. The characteristic shapes in Figure 12 can be seen by plotting the light

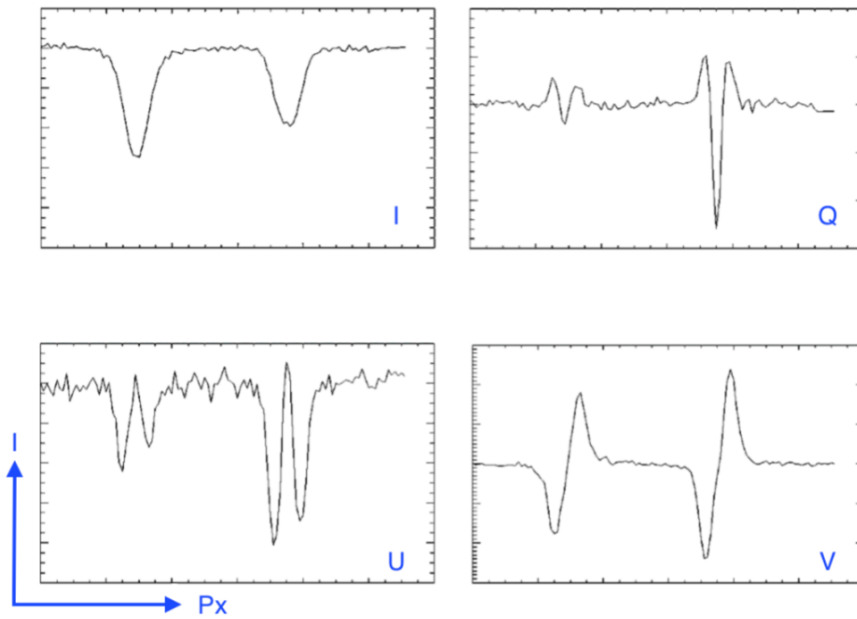


Figure 12: Measurements of the Stokes parameters on the AR NOAA 12443 measured along the Fe lines. Source: Silva (2017)

intensity (I) along each pixel (Px) of the image space.

## 2.2 The Helioseismic and Magnetic Imager

The Helioseismic and Magnetic Imager (HMI; Pesnell et al., 2012; Hoeksema et al., 2014) was launched on 11th February 2010 onboard the Solar Dynamics Observatory (SDO; Pesnell et al., 2012) and since 1st May 2010 it performs near-continuous measurements covering the entirety of the solar disk. HMI was designed to monitor the Sun in order to help uncover, but not exclusively, the origins and evolution of magnetic fields in the solar atmosphere. This continuous stream of data derived from observations taken from the whole visible part of the solar surface is a gigantic leap in comparison with what existed before and, at the time of writing this thesis, taking place, has completed the coverage of a complete solar cycle of 11 years. Specifically talking about measurements of the vector magnetic fields, these were rare to find before HMI and, mostly, data limited itself to observe the magnetic field along the LOS.

Earlier continuous measurements of the photospheric magnetic field were made using the Michelson Doppler Imager (MDI; Scherrer et al., 1995) that is aboard the Solar and Heliospheric Observatory (SOHO; Domingo et al., 1995) spacecraft. SOHO was launched in December of 1995 and

provided the solar community with the data that were crucial to produce new scientific results for over two decades. While its data can still be used, data from HMI has massive improvements over MDI. The most obvious example is the cameras that are measuring the magnetic field, as MDI has a 1024x1024 CCD camera that is 4 times smaller than its HMI counterpart. Also, comparing the definitive products, MDI LOS only magnetic field products are produced at a 96 min sampling that is about 8 times what HMI takes to calculate the full magnetic field vector. While studies from the HMI era benefited from more resolution, both temporal and spatial, data from MDI still provides an unique window to study the solar magnetic field from 1995 onward.

HMI has two  $4096 \times 4096$  cameras taking measurements around the Fe I 6173.34 Å absorption line, one of which is taking narrow-band images of the solar surface every 45 s while the other measures the linear and circular polarization at every 135 s in 0.5 arcsec pixels. Those images then contain the measurements of the Stokes parameters that are used to produce the vector magnetic field data after going through an inversion of Stokes procedure. The HMI Stokes inversion procedure that are used to calculate the vector magnetic field requires images of the Stokes parameters taken in six different wavelengths so that the Stokes profiles can be obtained after a Stokes inversion.

The Stokes inversion is performed by the Very Fast Inversion of the Stokes Vector (VFISV; Borrero et al., 2011) method that uses a Milne-Eddington (ME) atmosphere model to recover the Stokes profiles. VFISV assumes that the physical properties of the solar atmosphere are constant with height in addition to the source function being linearly dependent with the optical depth which allow the Radiative Transfer Equation (RTE) to be solved using the Unno–Rachkovsky solution (Unno, 1956). Stokes inversion algorithms are computationally demanding but by using VFISV, HMI is capable of producing high quality full-disk maps of the magnetic field vector every 10 minutes. The integration time of VFISV to produce maps of the vector magnetic field is significantly larger than the sampling of both cameras as by investigating the accuracy that can be obtained to recover the maps Borrero et al. (2007) showed that more accurate results could be produced by averaging VFISV parameters in time as it helps minimizing the impact of solar p-modes and photon noise in the data.

Saying that six images containing measurements at different wavelengths are being used to obtain the Stokes profiles implies that each Stokes parameter profile, as in Figure 12, is extrapolated

based on six points distributed over the wavelengths. For comparison, the Solar Optical Telescope (SOT; Tsuneta et al., 2008) onboard the *Hinode* (Kosugi et al., 2007) spacecraft uses 112 points to determine each of the Stokes profiles, greatly increasing the spatial sampling of each measurement. Unlike HMI, SOT is not taking measurements over the whole solar surface but rather along a slit region and to take the measurements to produce the vector magnetic field map of a single active region SOT can take several minutes to raster the slit across the solar surface. For a study where having continuous observations of the solar surface with a regular sampling is critical, HMI is then currently the most suitable instrument.

One of the major challenges while inverting the data is to solve the  $180^\circ$  azimuth ambiguity in the transverse field direction (Harvey, 1994). The transverse field ambiguity is a problem that arises from the fact that the measurements of transverse fields are obtained with only the plane of linear polarization, which will then result in two possible azimuths for the magnetic field vector that differ themselves by 180 degrees. To find the 'correct' magnetic field azimuth, in a process that is often referred to as disambiguation, the HMI pipeline uses the nonlocal minimization Metcalf (1994) method. This uses the potential field extrapolated from the LOS magnetic field to choose among the two possible solutions the one that will minimize the absolute value of the magnetic field divergence as this condition should be satisfied for any magnetic field.

Although the HMI pipeline does a great job in solving the  $180^\circ$  ambiguity for the majority of the disk, it can struggle to determine the correct (or a consistent) solution when ARs are close to the solar limbs. In an image of the vector magnetic field this would appear as a sudden change in polarity between two consecutive time stamps. There are other factors that also create difficulties in measuring the magnetic field and an in dept discussion on the limitations involved in HMI measurements can be found in Hoeksema et al. (2014).

While the trained eye can identify and ignore the most apparent shifts in polarity caused by disambiguation effects, it is challenging to develop algorithms that can discern changes caused by disambiguation effects and the plasma motions that normally take place in the solar surface. Then, if the shifts caused by disambiguation are not removed (or at the very least minimized) it can dramatically impact any result derived from the HMI magnetic field vector. The effects brought by the field ambiguity and the impact introduced on the results displayed in this work (as well as how it is addressed) are discussed in the data processing Chapter 4.

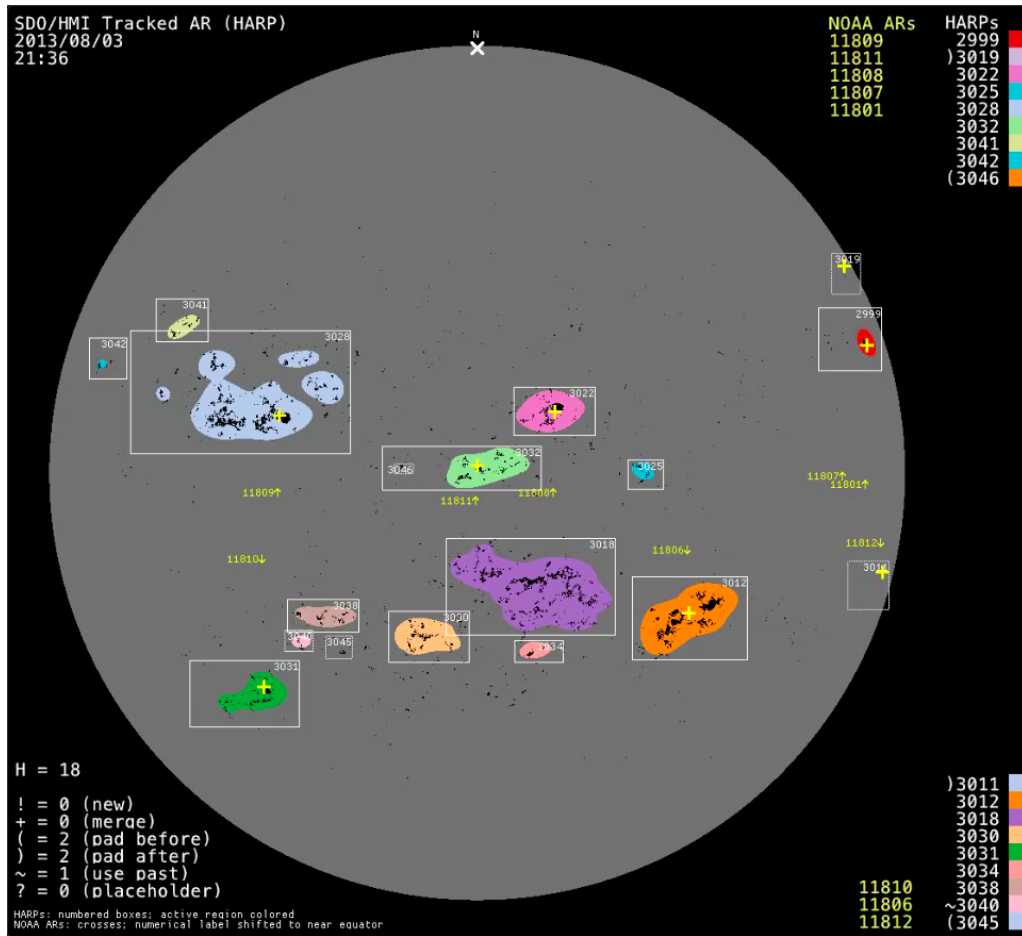


Figure 13: Distribution of HARP tracked regions on the solar disk at 2013/08/03 21:36 as made available by the HMI science team. Courtesy: JSOC and HMI science team.

Automated codes are used in the HMI pipeline to scan the images of the HMI 720 s LOS magnetic field and continuum to identify and track magnetic structures. If a magnetic structure has both a LOS field strength above 100 G and the size scale of an AR, the region encompassing the magnetic structure is designated as a HMI Active Region Patch (HARP). Based on the criteria to select the HARPs, NOAA regions can be associated with HARP regions but other magnetic structures such as plage also can fit the criteria to receive a HARP designation. Figure 13 shows an example of the HARP bounding boxes mapping produced by the HMI pipeline. Images like the one in Figure 13 are part of movies created by the HMI science team and made available by JSOC and show the overlay of the solar surface and the patches that are used to designed the HARPs (coloured regions) as well as the bounding boxes that are defined for each of them.

If a HARP magnetic structure appears isolated from other ARs or plage it is in principle quite straightforward to define the HARP boundaries. The boundaries need only to be large enough to

contain the whole structure throughout its passage as the definitive HARP bounding box size does not change in size during the image series produced for a region. However, the process of defining the boundaries for a HARP region are not always simple, as magnetic structures are often seen to be transiting over the solar surface in groups making it difficult, sometimes impossible, to draw a rectangular box containing only the magnetic field of a single AR structure. Another factor that further complicates setting HARP boundaries is that new magnetic structures can emerge inside already defined boundaries. In this case, another image series with a new bounding box may be created for the emerging region which will result in the same NOAA region being associated to two different HARPs. In the case of an emergent AR the data series contains up to two days before the region is spotted so the box should also be able to observe the pre-emergence area unless of course the region emerges close to the East limb<sup>1</sup>. In a more practical sense, the HARP bounding box represents the reduced FOV of the observations that are used in this thesis.

For the reasons mentioned above HARPs often contain the observations of multiple ARs and their trailing plage regions. During the solar minimum, where the solar surface is sparsely populated by ARs it is more common to find HARPs containing a single AR. On the other hand, during the solar maximum HARPs are more likely to be found containing two or more NOAA ARs.

Once the HARP box is set, each image from the HARP series will have its individual pixels classified according to their magnetic field. The mapping of these pixels in the HARP image space is available for download as an image in the `bitmaps` segment. Bitmaps provide a value mask of the image showing which pixels are considered magnetically active and which pixels are part of the quiet Sun which makes them useful to filter information or look for features in the HARP image space.

The images derived from HMI observations, as well as most of the image data made available for and by the astronomical community, are encoded as Flexible Image Transport System (FITS; Wells et al., 1981; Pence et al., 2010) using the extension `.fits`. One of the main advantage of using the FITS format is its flexibility that allows metadata to be inserted in the same file as the image. Each FITS file produced for the HARPs series contain extensive information from the structures in the HARP such as: the heliographic latitude and longitude of the HARP box, which NOAA numbers are in the HARP and the LOS magnetic flux. The full list of features in

---

<sup>1</sup>Left hand side of the Sun with the north up as observed by the HMI.

the metadata can be found in Hoeksema et al. (2014).

HARPs are made available in two different data series: near real-time (nrt) and definitive. The main difference between those segments is related to the geometry of the HARP. Since for the nrt HARPs it is not yet known how the magnetic flux coverage will evolve, so it is not possible to define a fixed bounding box for the whole HARP lifetime as new features may emerge or the different features being observed may move beyond the box limits. Some of the HARPs in the nrt series may also be flagged for merging in the definitive version.

### **HMI SHARPs**

The Space-weather HMI Active Region Patch (SHARP; Bobra et al., 2014) is a data series with the collection of the most relevant observations in the HARP series. SHARPs cover observations from all the ARs observed since 1st May 2010 and, as it is for most data from the SDO science team, can be requested via the Joint Science Operations Center (JSOC). Data in the SHARPs receive more processing in the HMI pipeline than the other HARP observations and therefore have a more complete set of products, including also a summary of AR-related parameters for every observation. For a complete list of these parameters see Table 3 in Bobra et al. (2014).

The data series derived from HMI observations are produced using the World Coordinate System (WCS) for solar images (Thompson, 2006) to establish the physical values for position within the image space. The WCS is also commonly used in images produced from observations made by other instruments in the astrophysics community. The SHARPs are available in helio-projective Cartesian CCD image coordinates or in a heliographic Cylindrical Equal-Area (CEA) format. Like the HARPs, SHARPs also are available in a nrt and a definitive series. There are then four different SHARP data series based on the projection and timing (`hmi . sharp_720s`, `hmi . sharp_cea_720s`, `hmi . sharp_720s_nrt` and `hmi . sharp_cea_720s_nrt`), all of which as their name suggests have a 720 s sampling. The spatial sampling covered by a HMI pixel is  $\sim 362.5$  km across, which covers about half an arcsecond of the solar surface. The CEA series is remapped from plane-of-sky image sampling to a Lambert CEA projection that minimizes distortions when close to the equator. Although the distortions are significant away from the equator, the Lambert CEA projection is quite appropriate when studying ARs considering that regions lie within  $\pm 45^\circ$  latitude. The vector magnetic field in the CEA series is then made available in cylindrical coordinates ( $B_r$ ,  $B_\theta$  and  $B_\phi$ )

instead of field strength and azimuth and inclination angles with respect to the LOS.

The results in this work were produced by making extensive use of the `hmi . sharp_cea_720s_nrt` data series, directly benefiting from this data format for the following reasons:

- the AR target pointing has already been achieved through field-of-view cut-outs on NOAA-numbered ARs (and additional strong unspotted flux concentrations);
- the images have already been remapped from plane-of-sky image sampling to a Lambert cylindrical equal-area (CEA) projection;
- the **B** has already been reformatted from the line-of-sight reference frame into spherical components defined in the solar radial ( $B_r$ ), longitude ( $B_\phi$ ) and latitude ( $B_\theta$ ) directions.

The final two points listed above allow for more direct comparison of results from ARs at locations away from solar disk centre (i.e., where plane-of-sky pixels cover different surface length scales and the line-of-sight deviates significantly from the surface normal). Specific information about the ARs such as their Mt. Wilson classification or on any events associated to them are supplemented by daily reports on space weather described in the following section.

### 2.3 NOAA/SWPC reports

The NOAA Space Weather Prediction Center (SWPC) is part of the United States National Weather Service and it is responsible for monitoring and forecasting the Earth space weather. SWPC then publishes reports of a diversity of features that determine the conditions in the solar-terrestrial environment. The reports are not only used to produce science but also for branches of industry where space weather is relevant, such as aviation or companies that operate the electric grid.

To obtain information about the sunspot morphology and events associated with the ARs present in the SHARPs, data from the SWPC *Solar Region Summary* (SRS) and *Events* reports were used. These files present an overview of the properties of ARs such as their daily Mt. Wilson classification, spot area, location and the flares that the region produced. Although the format which observations are published in has changed a few times, and new products were designed over the years, some segments such as the Report of Solar and Geophysical Activity (RSGA) provide files containing the reports since 1966 that, back then, contained all the information related

```

:Product: 1104SRS.txt
:Issued: 2015 Nov 04 0030 UTC
# Prepared jointly by the U.S. Dept. of Commerce, NOAA,
# Space Weather Prediction Center and the U.S. Air Force.
#
Joint USAF/NOAA Solar Region Summary
SRS Number 308 Issued at 0030Z on 04 Nov 2015
Report compiled from data received at SWO on 03 Nov
I. Regions with Sunspots. Locations Valid at 03/2400Z
Nmbr Location Lo Area Z LL NN Mag Type
2443 N06E03 314 0560 Fkc 17 52 Beta-Delta
2445 N16W69 026 0200 Eac 11 10 Beta-Delta
2447 N03E23 295 0020 Cro 02 03 Beta
IA. H-alpha Plages without Spots. Locations Valid at 03/2400Z Nov
Nmbr Location Lo
2439 N16W87 046
2441 N15W46 005
2442 N16W76 035
2444 S04W14 333
2446 N15W31 350
II. Regions Due to Return 04 Nov to 06 Nov
Nmbr Lat Lo
None

```

Figure 14: Example of the SWPC SRS file for 2015-11-04.

to space weather gathered from different observatories. The SRS and *Events* reports started being published in 1996 and are since then made available by SWPC.

The SRS files are produced based on reports of the preceding day from up to six different ground based observatories that report to SWPC in near real time. The number of observatories that contribute with observations in the report may vary as local weather conditions may make observing the Sun impossible. The SRS .txt file for 2015-11-04 is displayed as an example in Figure 14. Each SRS file contains a header that has general information about the file followed by three sections which summarise i) the observations of regions with sunspots, ii) regions that can be observed in H-alpha but do not show spots and iii) regions that are due to return. Only the information in the first section (I. Regions with Sunspots.) of the SRS files is needed here because the objective of this work is to study the energy injection in ARs. Each row of this section contain the following information about an AR:

- Nmbr: The NOAA region number;
- Location: AR location on the disk;
- Lo: Carrington longitude of the group;
- Area: total corrected area of the group in millionths of the solar hemisphere;

Edited Events for 2015 Nov 04										
#	#Event	Begin	Max	End	Obs	Q	Type	Loc/Frq	Particulars	Reg#
2280 +	0921	0925	0927	G15	5	XRA	1-8A	B9.6	2.1E-04	2445
2280	0924	0925	0929	LEA	3	FLA	N17W65	SF	DSD	2445
2310 +	B0930	U0948	A1055	SVI	3	FLA	N08E03	SF		2443
2310 +	1028	1032	1035	G15	5	XRA	1-8A	C1.1	2.9E-04	2443
2320 +	1155	1203	1206	G15	5	XRA	1-8A	M2.5	7.3E-03	2445
2320	1200	1200	1202	SAG	G	RBR	1415	34		2445
2320 +	1201	1202	1203	SVI	G	RBR	8800	94		2445

Figure 15: Example of the SWPC *Events* file for 2015-11-04.

- Z: McIntosh classification of the group;
- LL: longitudinal extent of the group in heliographic degrees;
- NN: total number of visible sunspots in the group;
- Mag Type: Mt. Wilson magnetic classification of the group.

The information concerning any flares that the observed ARs produced is extracted from the *Events* files. As with the *SRS*, the *Events* reports also result from the contributions of different ground-based observatories, but these are also supported by satellite observations from the Geostationary Operational Environmental Satellite (GOES). The *Events* .txt file for 2015-11-04 is shown as an example in Figure 15. Each column in an *Events* file contains the following information:

- Event: event number;
- Begin: UTC time that the event began;
- Max: UTC time when the event reached its peak;
- End: UTC time when the event ended;
- Obs: the reporting observatory;
- Q: the quality of the data;
- Type: the report type;
- Loc/Frq: location or frequency or wavelength of the event;

- Particulars: additional information from the report;
- Reg#: the SWPC-assigned NOAA number.

In the context of this work, the relevant energetic events are only GOES soft X-ray flares and therefore, from the *Events* files, only the entries where the column *Type* is flagged as *XRA* are relevant.



## Chapter 3

# Poynting flux and photospheric velocity inversion methods

### 3.1 Poynting flux theory

In the Introduction Chapter it was briefly discussed how the motion of plasma can inject or remove energy into an existing magnetic structure. In this Chapter it will be discussed how the Poynting flux can be calculated at the photosphere and the challenges inherent to this task.

#### 3.1.1 Poynting flux in the photosphere

The Poynting flux is a representation of how much energy is being transferred through a given surface. Assuming that the observed magnetic field is on a surface and considering that for the purposes and intents of this work the base of the photosphere can be treated as being said surface, calculating the Poynting flux would then show how much energy is flowing from the convective zone into the chromosphere and corona. The Poynting flux ( $\mathbf{S}$ ) can be calculated as the cross product between the electric ( $\mathbf{E}$ ) and magnetic ( $\mathbf{B}$ ) fields,

$$\mathbf{S} = \frac{1}{\mu_0} \mathbf{E} \times \mathbf{B}, \quad (3.1)$$

which can also be expressed in its integral form, by considering a surface ( $S$ ) the Poynting flux is,

$$\mathbf{S}_s = \frac{1}{\mu_0} \int_S \mathbf{E} \times \mathbf{B} \cdot \mathbf{n} dS, \quad (3.2)$$

where  $\mathbf{n}$  is the unit vector normal to the surface. Most of the dynamics in the solar surface can be described using the magnetohydrodynamics (MHD) equations where the plasma is considered to display fluid like behaviour. In an ideal MHD regime, where the plasma can be treated as a perfect conductor, Ohm's law is,

$$\mathbf{E} + \mathbf{v} \times \mathbf{B} = \mathbf{0}, \quad (3.3)$$

which is a useful property as it allows the electric field to be described in terms of the velocity ( $\mathbf{v}$ ) and the magnetic field ( $\mathbf{B}$ ) vectors,

$$\mathbf{E} = -\mathbf{v} \times \mathbf{B}. \quad (3.4)$$

By substituting Equation 3.4 into Equation 3.2 the Poynting flux can then be calculated without the electric field depending only on the velocity and the magnetic field vectors,

$$S_s = \frac{1}{4\pi} \int_S (-\mathbf{v} \times \mathbf{B}) \times \mathbf{B} \cdot \mathbf{n} dS, \quad (3.5)$$

which is a major advantage in relation to using Equation 3.2 since the magnetic field vector can be measured in the photosphere and, as discussed in the next chapter, the velocity vector in the photosphere can be calculated from a sequence of vector magnetic field images. Now to leave the Poynting flux equation on a positive note, consider that for a cross product between two vectors,

$$\mathbf{A} \times \mathbf{C} = -\mathbf{C} \times \mathbf{A},$$

which then allows the Poynting flux at the photosphere to be calculated as (see, e.g., Kusano et al., 2002),

$$S_s = \frac{1}{4\pi} \int_S \mathbf{B} \times (\mathbf{v} \times \mathbf{B}) \cdot \mathbf{n} dS = S_n + S_t. \quad (3.6)$$

Equation 3.6 can be split into two different components that will account for the separated contributions given by the flux emergence (i.e., due to velocities that are normal to the surface,  $\mathbf{v}_n$ ),

$$S_n = \frac{1}{4\pi} \int_S B_t^2 \mathbf{v}_n \cdot \mathbf{n} dS , \quad (3.7)$$

and a shearing motion (i.e., due to velocities that are tangential to the surface,  $\mathbf{v}_t$ ),

$$S_t = -\frac{1}{4\pi} \int_S (\mathbf{v}_t \cdot \mathbf{B}_t) \mathbf{B}_n \cdot \mathbf{n} dS , \quad (3.8)$$

where  $\mathbf{B}_t$  is representing the photospheric 2D tangential magnetic field vector (i.e., parallel to the photospheric surface) and  $\mathbf{B}_n$  is the vertical magnetic field (i.e., normal to the photosphere).

While Equations 3.7 and 3.8 can quantify the energy exchange through the photosphere, they do not indicate what portion of the magnetic energy that is being injected into or removed from an AR corresponds to free magnetic energy, which is the energy available to produce energetic events such as flares or CMEs. The most appropriate method to track the energy budget relies on using magnetic field extrapolations as discussed in Chapter 1.

### 3.1.2 Proxy Poynting flux

To calculate Equations 3.6, 3.7 and 3.8 one then needs data from the full vector magnetic field and plasma velocities. However, the degree of coverage provided by HMI is rather unique and measurements of the full vector magnetic field before HMI were rare to find. An alternative to using the full vector magnetic field to study the energy injection was then to use a proxy version of Poynting flux (e.g., Tan et al., 2007),

$$S = \frac{1}{4\pi} |v_t| B_n^2 . \quad (3.9)$$

Equation 3.9 accounts for the Poynting flux caused by photospheric footpoint motions as in Parker (1979),

$$S = -\frac{1}{4\pi} v_t B_n B_t > 0 , \quad (3.10)$$

with the assumption that the normal and tangential components of the magnetic field are equivalent. Regarding these assumptions, Tan et al. (2007) warns that when the magnetic field is almost horizontal (vertical), the proposed assumption will result in a overestimation/underestimation of the Poynting flux. Equation 3.9 is similar in terms to Equation 3.8 assuming that  $B_n \approx B_t$ . Basi-

cally, Equation 3.9 accounts for the unsigned contributions of the tangential velocities.

Since only the LOS magnetic field and tangential velocities are necessary to calculate Equation 3.9, data from SOHO/MDI and the plasma velocities obtained by feeding a sequence of LOS magnetogram images into feature tracking methods are sufficient for its calculation.

Although the assumptions that support the use of the proxy Poynting flux are debatable at best, they are a fair attempt to explore the energy dynamics of the photosphere with the data that was available at that time as MDI provided a continuous coverage of the solar surface LOS magnetic field. Studying the proxy Poynting flux then allowed many authors (to name a few, Tan et al., 2007; Welsch et al., 2009; Li et al., 2010; Welsch et al., 2011; Fan et al., 2011) to explore the connection between the photospheric flows and energy injection. These works, that are reviewed in detail in Chapter 5, also created a larger demand for better image tracking methods that then contributed to their development and improvement.

### 3.1.3 Removal of field aligned velocities

Considering that the Poynting flux Equation 3.6 depends on the cross product between velocity and magnetic field, the very nature of a cross product will immediately result in any velocity that is in the same direction as the magnetic field not contributing to the energy injection or removal. This is not a problem for calculating Equation 3.6 (as it's a cross product), but does become a problem for Equations 3.7 and 3.8 (as it relies on dot products). Then, not removing these field-aligned velocities from the velocity field that is calculated using a sequence of magnetic field images will impact the numerical calculation of the two Poynting flux components.

The methods used to calculate the velocity vector track the movement of features between two successive images, or image sets, of the magnetic field. Démoulin and Berger (2003) point out that tracking methods are following the motion of the intersection that flux tubes have with the photosphere as illustrated in Figure 16.

Figure 16 illustrates a flux tube that is crossing through the photosphere and moves with a velocity  $\mathbf{u}_f$ . Démoulin and Berger (2003) points that from the geometry in Figure 16 there is a ratio between the vectors  $|\mathbf{u}_f|/v_n = |B_t|/B_n$ . Then an inclined flux tube can lead to a measured horizontal velocity through either a real horizontal movement or by emergence (if its photospheric intersection point

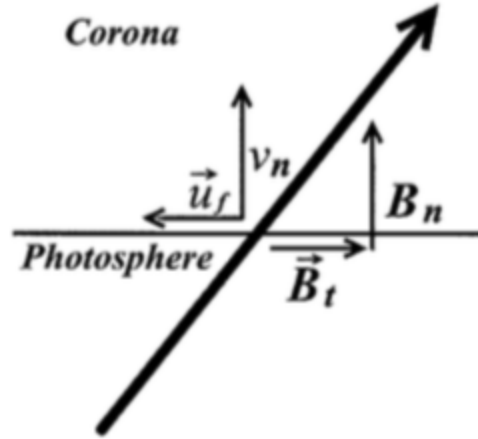


Figure 16: Diagram of a flux tube rising through the photosphere. Source: Démoulin and Berger (2003).

is moving horizontally). The observed velocity  $\mathbf{u}$  can be expressed as,

$$\mathbf{u} = \mathbf{v}_t - \frac{v_n}{B_n} \mathbf{B}_t. \quad (3.11)$$

Welsch (2006) later defines the observed velocity  $\mathbf{u}$  as the ideal flux transport velocity. Welsch (2006) further expands the discussion on the differences between the ideal flux transport velocity ( $\mathbf{u}$ ) and the plasma velocity ( $\mathbf{v}$ ). First, the ideal flux transport velocity ( $\mathbf{u}$ ) is a representation of the movement observed by magnetic features in a magnetogram when their evolution can be considered ideal (i.e., when the diffusive transport is neglectible). Also,  $\mathbf{u}$  is able to capture flux cancellation or emergence that happen in the sequence of images used to calculate it.

In 2012 with the HMI coverage of the solar surface, the greater accessibility of vector magnetic field data made it possible to explore the complete picture of the photospheric Poynting flux as in Equations 3.6, 3.7 and 3.8 which require knowledge of both the velocity and magnetic field vectors. Schuck (2008) then uses the discussion of Démoulin and Berger (2003) to further explore the relationship between the ideal flux transport velocity and the plasma velocity so that the full plasma velocity vector can be obtained. Schuck (2006) then uses the flux transport vector ( $\mathbf{F}$ ) to establish a relationship between  $\mathbf{u}$  and  $\mathbf{v}$ ,

$$\mathbf{F} = \mathbf{u}B_n \equiv B_n\mathbf{v}_t - v_n\mathbf{B}_t = \hat{n} \times (\mathbf{v} \times \mathbf{B}) = \hat{n} \times (\mathbf{v}_\perp \times \mathbf{B}), \quad (3.12)$$

where  $\mathbf{v}_\perp$  is the plasma velocity perpendicular to the magnetic field and the terms  $B_n\mathbf{v}_t$  and  $v_n\mathbf{B}_t$

represent the shearing and emergence motions of the plasma, respectively. Then the plasma velocity  $\mathbf{v}$  is presented as,

$$\mathbf{v} = \mathbf{u} - \frac{(\mathbf{u} \cdot \mathbf{B}_t) \mathbf{B}}{|\mathbf{B}|^2} + v_{\parallel} \frac{\mathbf{B}}{|\mathbf{B}|}, \quad (3.13)$$

where  $v_{\parallel}$  is the plasma velocity parallel to the magnetic field. The horizontal and vertical components of plasma velocity that are perpendicular to the magnetic field can then be written as,

$$\mathbf{v}_{\perp t} = \mathbf{u} - \frac{(\mathbf{u} \cdot \mathbf{B}_t) \mathbf{B}_t}{|\mathbf{B}|^2}, \quad (3.14)$$

and,

$$\mathbf{v}_{\perp n} = -\frac{(\mathbf{u} \cdot \mathbf{B}_t) \mathbf{B}_n}{|\mathbf{B}|^2}. \quad (3.15)$$

Equations 3.14 and 3.15 then recover the correct plasma velocity contributions from the ideal flux transport velocity for use in calculating the two components of Poynting flux.

### 3.1.4 Modified Poynting flux equations

The emergence and shearing components of Poynting flux that are represented in Equations 3.7 and 3.8 can then be modified to use only the Equations 3.14 and 3.15 plasma velocities that are perpendicular to the magnetic field (e.g., Liu and Schuck, 2012),

$$S_{\perp n} = \frac{1}{4\pi} \int_S B_t^2 \mathbf{v}_{\perp n} \cdot \hat{n} dS, \quad (3.16)$$

and,

$$S_{\perp t} = -\frac{1}{4\pi} \int_S (\mathbf{v}_{\perp t} \cdot \mathbf{B}_t) \mathbf{B}_n \cdot \hat{n} dS. \quad (3.17)$$

In the HMI era, the results from Equations 3.16 and 3.17 were used to keep striving for a better understanding on the energy dynamics of the photosphere. It is worth mentioning that most of these works were presenting results and discussions that are more focused on studying the helicity of ARs or using Poynting flux results to conduct a case study about one AR or a small group of ARs. In the next Chapter it will be discussed how a sequence of images from the magnetic field can be used to calculate the plasma velocity and how those methods evolved to benefit from the continuous coverage of vector magnetic field data provided by HMI.

## 3.2 Calculating velocities from magnetic field data

One of the most simple cases to obtain the velocity at which features in an image are moving would be to calculate the velocity of a vehicle, lets say a McLaren MP4/4, that is racing in a straight line while being observed by a camera. From a sequence of these images and assuming that it is known when each image was taken and what is the spatial sample of the camera (i.e. how much physical distance each pixel is covering), calculating the velocity of the MP4/4 is a simple matter of counting how many pixels the MP4/4 moved from one image to the next and dividing by the time interval between the two images. Then, the camera that is taking the images needs to have a spatial (i.e., the physical dimension covered by each pixel) and temporal (i.e. the time difference between two images) sample that befits this problem.

Methods that are able to detect movement from a sequence of images see applications in a huge diversity of products ranging from advanced defence systems that are capable to intercept incoming missiles to creating video game controllers like the Microsoft kinect. The physics involved in each problem are vastly different and although these methods have the shared goal of estimating the velocity of features in a sequence of images they can be very unique in their approaches.

### 3.2.1 Velocity inversion in the photosphere

Velocity inversion techniques are the set of tools that allow the velocity of the magnetized plasma to be measured using a sequence of photospheric magnetic field images. The photosphere is known, through both observations and theory, to be incredibly dynamic with a different variety of motions exhibited by the many magnetic structures that are seen there. Therefore, trying to estimate the velocity of a feature using a similar logic as that discussed in the 2D MP4/4 example above would more often than not lead to unrealistic results as the magnetic features can for example emerge or submerge (i.e., a 3rd dimension of motion) or cancel themselves. A tracking code could mistake these typical photospheric behaviours for an unrealistically fast motion of the observed magnetic structure entering or leaving the image space.

The velocity obtained through a sequence of solar images was first commonly calculated using Local Correlation Tracking (LCT; November and Simon, 1988). LCT is a method that uses cross correlation techniques to track features that can be observed in successive images. The MDI was

the first solar instrument to provide a consistent and continuous coverage of magnetic field data for codes that use LCT. Chae (2001) was among the first authors that presented work applying LCT to a series of MDI LOS magnetograms, and by studying NOAA 8011 they achieved an observational calculation of the magnetic helicity through a sequence of magnetic field images.

As pointed out by Schuck (2008), most methods that were developed to estimate the plasma velocities in the photosphere make use of the induction equation to find solutions that are realistic (i.e. speeds that do not exceed the limitations imposed by the medium), so events like the emergence of a new magnetic structure are not treated as if the structure had entered the image space with an incredible speed. The normal component of the induction equation can be written as,

$$\partial_t B_z + \nabla_h \cdot (B_z \mathbf{v}_h - v_z \mathbf{B}_h) = 0, \quad (3.18)$$

and was used by Kusano et al. (2002) to test the LCT solutions extracted from vector magnetograms so that the velocity fields obtained would not contradict the induction equation. Although Kusano et al. (2002) presented a method to improve the accuracy in obtaining velocities from vector magnetograms, the magnetic field data necessary to do so was only made routinely available almost a decade later when HMI started producing its measurements and the SDO science team made the data available.

### 3.2.2 Overview of different methods used for velocity inversion with LOS magnetic field data

The different methods that could estimate the plasma velocities using measurements of the LOS photospheric magnetic field and their performances were reviewed by Welsch et al. (2007). The existing algorithms that are being used to invert velocities using HMI data are mostly updated versions from the algorithms discussed in Welsch et al. (2007). To compare the methods synthetic magnetograms were produced using an Anelastic MHD (ANMHD) simulation so that the results obtained by the different codes could be compared to a “ground truth”. Over the course of the next paragraphs the velocity inversion methods will be discussed and compared as in the review (Welsch et al., 2007).

### **LMSAL LCT**

As pointed out earlier, the first use of LCT in the context of solar physics was made by November and Simon (1988) with white-light images, while the technique was later modified by Hurlburt et al. (1995) and DeRosa (2001) to be able to work with LOS magnetograms. This approach is known as the Lockheed Martin Solar and Astrophysics Laboratory (LMSAL) LCT. This method tracks the movement of information in image pixels through the minimization of a merit function with the position of different features in a pair of consecutive images. The implementation has a limitation when processing two images that are separated by a larger time interval, as any movement exceeding one pixel (i.e., a feature that moves beyond its immediate vicinity) is treated as a miscalculation which can happen quite often depending on the temporal sampling.

### **Induction Method**

The Induction Method (IM; Kusano et al., 2002) was the first algorithm that made explicit use of the magnetic induction equation to calculate the velocity fields in the photosphere, paving the way for other “inductive” algorithms. This method assumes that the horizontal velocities are known through LCT and tries to find the vertical velocities that then satisfy the induction equation. It does however rely on the observed region having one or more null points, which is often the case for ARs, to ensure the uniqueness of the solution. This method has a drawback for horizontal magnetic fields that are close to zero, where the vertical velocity will reach a singularity.

### **Minimum Energy Fit**

Focusing on the evolution of the magnetic features, the Minimum Energy Fit (MEF; Longcope, 2004) presents a method that tries to find the velocity vector that will minimize a penalty function. In the review of Welsch et al. (2007), the penalty function used for MEF was obtained by comparing the sum of the squares of the velocity vectors and the flow fields obtained with how much they needed to be smoothed to remove large velocities in regions close to polarity inversion lines (PILs) as they failed to converge to a minimum energy solution. The process to smooth and remove large velocities may need to be repeated multiple times, that can result in the calculations being computationally expensive.

### Fourier LCT

The Fourier LCT (FLCT; Welsch et al., 2004) is a method that computes the correlation function in Fourier space, unlike the implementation of November and Simon (1988) that uses the physical space. This led to the method being not only more accurate than the LCT counterpart but also faster to calculate as tested by Welsch et al. (2009). However, the same tests indicate that FLCT faces difficulties to obtain accurate speeds for regions with modest magnetic field ( $|B_z| \leq 370G$ ). Knowing the limitations of FLCT, the same work of Welsch et al. (2004) also contains an alternative approach called Inductive Local Correlation Tracking (ILCT). This method uses the results obtained by an LCT method with the additional assumption that the induction equation governs the component of the velocity vector that is perpendicular to the magnetic field. Although ILCT can also obtain the electrostatic potential using the results of LCT, it is also found to perform poorly in regions of small vertical magnetic field. An option presented by Welsch et al. (2007) to work with ILCT is to set the magnetic field threshold used by the algorithm to filter out unwanted contributions to a very low value (1 G in Welsch et al. (2007)) and then manually remove the velocities obtained from regions of low magnetic field strength after the processing is completed.

### Minimum Structure Reconstruction

Georgoulis and LaBonte (2006) developed the Minimum Structure Reconstruction (MSR) method which is another technique that uses both the inductive and electrostatic potential to calculate the photospheric velocities. This method assumes that the photospheric flows can only take place along the magnetic field lines and that  $v_{\perp z} = 0$  in ideal MHD conditions. This presented a complication for Welsch et al. (2007) in comparing the MSR results with the other methods because the ANMHD simulation was recreating the emergence of a magnetic flux tube where  $v_{\perp z} \neq 0$ , which led the MSR method to overestimate the horizontal velocities.

### Differential Affine Velocity Estimator

The Differential Affine Velocity Estimator (DAVE; Schuck, 2006) presents an alternative method to applying LCT to estimate photospheric velocities. DAVE calculates the flux transport velocity through a variational principle that is solved directly by either linear or total least-squares methods. The ideal Ohm's law and an affine flux transport velocity profile act as constraints for the solutions

obtained with the variational principle, ensuring that the velocities obtained are consistent with the magnetic induction equation. DAVE applies its algorithm in subregions, square window, of the image that are defined by the convolution kernel. The performance of the algorithm varies according to the window size being used, which is studied and presented in Schuck (2006).

### **Comparing the performance**

The comparisons made by Welsch et al. (2007) between the results obtained with the different methods mentioned above and the ANMHD simulation include not only the plasma velocities but also other quantities that can be derived once the plasma velocity is known, such as: electric field, magnetic induction, magnetic flux and Poynting flux. The performance of the different methods were found to be quite comparable with no clear top performer across all derived quantities. However, some methods did prove to be more accurate when compared to the others for some specific parameters being calculated. While DAVE performed slightly better to recover the direction and magnitude of the velocities, MEF was the most successful at recovering the electric field.

It is important to note that Welsch et al. (2007) found all of the methods to present significant errors when compared to the “ground truth” provided by the ANMHD simulations. Also, all of these methods were developed to calculate velocities based only on LOS magnetograms which may lead to the results not being necessarily consistent with the evolution of the horizontal field.

Shortly after Welsch et al. (2007) presented their work, updated versions of these methods started being developed to calculate the plasma velocities from a sequence of images of the full magnetic field vector. By having access to the full vector magnetic field the velocity inversion algorithms were capable to produce results that are also consistent with the evolution of the horizontal field. The updated versions capable of working with the 3D magnetic field show a drastic improvement in their accuracy to obtain the velocities when compared to their older versions that work only with LOS magnetic field data, and is discussed in detail in the following section.

### **3.2.3 Velocity inversion using vector magnetic field data**

The Differential Affine Velocity Estimator for Vector Magnetograms (DAVE4VM; Schuck, 2008) is a version of DAVE that was updated to work with full magnetic field vector data. When presenting DAVE4VM, Schuck (2008) also use an ANMHD simulation in an approach akin to Welsch

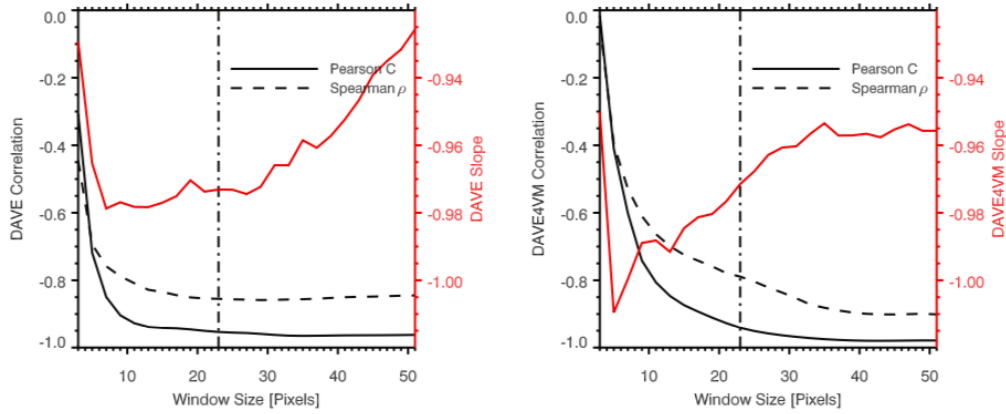


Figure 17: Optimization curves comparing the accuracy of DAVE (left panel) and DAVE4VM (right panel) as a function of the window size. Source: Schuck (2008).

et al. (2007), to assess the performance of both DAVE and DAVE4VM and compare the two versions. DAVE4VM shows a dramatic improvement over DAVE, reaching high precision in recovering all of the velocity-derived parameters from the ANMHD simulation.

Both DAVE and DAVE4VM rely on a window size that is defined by the user, from which the calculations of the plasma velocities are based. The window-size choice directly affects the kernel applied to the convolutions that is used to calculate the many terms in the error metric. Velocities are obtained considering the best fit for local plasma flow in relation to the center of the window. In Schuck (2008), both DAVE and DAVE4VM retrieved their best results when compared to the ANMHD simulations for a window size with 21 – 25 HMI pixels, as shown in Figure 17. The panels in Figure 17 shows the optimization curves obtained for both DAVE and DAVE4VM being the Spearman rank order represented by the dashed black curve and Pearson by the solid black curve. Generally, negative values for Spearman and Pearson coefficients indicate that the values in the y-axis tends to decrease in value as the values in the x-axis increase.

Table 3, extracted from Schuck (2008), shows a summary of the different quantities considered and their Spearman and Pearson coefficients as well as the slope of the scatter plots created between the results from DAVE and DAVE4VM versus the “ground truth” provided by the ANMHD simulation. Mind that the results from DAVE are assuming that the plasma velocity ( $\mathbf{v}$ ) and the ideal flux transport velocity ( $\mathbf{u}$ ) are equivalent which is not correct however, to calculate the plasma velocity from the ideal flux transport velocity, it is necessary to know the full vector magnetic field as described in Equations 3.13 that DAVE has no access to. Table 3 shows that introducing the

Table 3: Comparison between the performance of DAVE and DAVE4VM. Source: Schuck (2008).

Quantities		Dave (Assuming $\mathbf{v} = \mathbf{u}$ )			DAVE4VM		
1	2	Spearman	Pearson	Slope	Spearman	Pearson	Slope
$u_x B_z$	$U_x B_z$	0.34	0.57	0.15	0.88	0.89	0.80
$u_y B_z$	$U_y B_z$	0.70	0.76	0.71	0.94	0.90	0.89
$v_{\perp x}$	$V_{\perp x}$	0.87	0.85	0.91	0.89	0.88	0.94
$v_{\perp y}$	$V_{\perp y}$	0.93	0.92	1.20	0.94	0.94	1.00
$v_{\perp z}$	$V_{\perp z}$	0.17	0.28	0.07	0.80	0.80	0.79
$\nabla_h \cdot (\mathbf{u} B_z)$	$\Delta B_z / \Delta t$	-0.85	-0.95	-0.97	-0.79	-0.94	-0.97
$e_{\perp x}$	$E_{\perp x}$	0.70	0.76	0.71	0.94	0.90	0.89
$e_{\perp y}$	$E_{\perp y}$	0.34	0.57	0.15	0.88	0.89	0.80
$e_{\perp z}$	$E_{\perp z}$	0.96	0.96	1.20	0.94	0.97	1.00
$s_z$	$\mathbf{S}_{\perp z}$	0.20	0.12	0.04	0.88	0.83	0.71

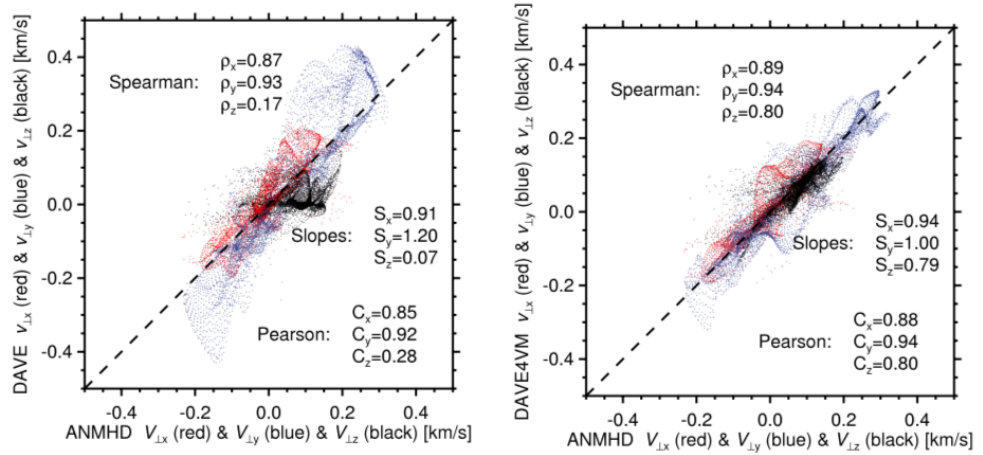


Figure 18: Scatter plots of the different velocity components obtained by DAVE (left panel) and DAVE4VM (right panel) against the “ground truth” of the ANMHD simulation. The points in red, blue, and black represent the x, y, and z components of the velocity vector, respectively. Source: Schuck (2008).

full vector magnetic field data in the calculations improved significantly the precision to which the velocities are recovered, especially in the vertical component. The differences between DAVE and DAVE4VM are further discussed in Schuck (2008) with scatter plots between the different velocity components and the ANMHD simulation, here shown in Figure 18. The black dashed line in Figure 18 represents the line where the results from DAVE or DAVE4VM are exactly equal to the simulation output. The results from DAVE4VM show their largest improvements when compared to DAVE in the y and z components of the velocity vector, with the component along the x-axis having a similar level of dispersion around the dashed line in both DAVE and DAVE4VM.

The calculations performed by DAVE4VM are significantly more demanding than in DAVE. This

can be directly noticed by comparing the number of terms that are necessary to calculate the error metrics that find the best fit for the velocities in relation to the window center. For DAVE the error metric contains a matrix of 15 elements while for DAVE4VM this matrix contain 100 elements. All of these elements are numerically calculated using convolutions of the vector magnetic field images and additional images derived from them which can be a computationally expensive process depending on the image size. The accuracy of DAVE4VM has led to it being one of the most popular methods to obtain velocities from vector magnetic field data during the HMI area.

More recently, some tools are being developed to make use of deep learning methods to estimate horizontal velocities (e.g., Asensio Ramos et al., 2017) and their performance are mostly tested by comparing their results to those obtained using LCT. Also, new tools such as DAVE4VM with Doppler Velocities (DAVE4VMwDV; Liu et al., 2020) may pave the way for further exploration as they have recently been shown to achieve remarkable accuracy in the energy and helicity flux of an AR when tested against an ANMHD simulation.

## Chapter 4

# Data processing

Here the development of the algorithms and methods used to process the data and derive the products necessary to generate the results in this work will be discussed. Codes used in the processing (including the full pipeline responsible for downloading, processing and storing the data) are currently available from the author's github repository: <https://github.com/Chicrala>.

### 4.1 PyDAVE4VM

#### 4.1.1 Python in Solar/Astro Physics

There is an growing demand to make the codes and algorithms used to produce science available to public access although, as this thesis is being written, there are not yet widespread rules that enforce an author to make the codes associated to a scientific publication available. With science being a product of collective human effort, collaboration is particularly desirable and should be encouraged. With the growing dependency on software to produce scientific publications new guidelines on how to use, collaborate and proper acknowledge the usage of different libraries are being constantly discussed and elaborated. For example, DAVE4VM and a variety of other algorithms that explore different aspects of solar-terrestrial physics are made available for computational runs on the NASA Community Coordinated Modeling Center (CCMC) infrastructure.

The original version of DAVE4VM was written by Schuck (2008) in Interactive Data Language (IDL). By the time DAVE was first developed, IDL was the *lingua franca* of solar physics with

a large number of community contributed packages developed to access, process and work with solar data being distributed by Lockheed Martin Solar and Astrophysics Laboratory (LMSAL). The package distribution known as SolarSoft still offers a large degree of support for research in solar physics. However, IDL is a commercial distribution and also a niche language, not being broadly adopted across many communities in academia or industry. The existence of a standard distribution for solar physics is much of what keeps some solar physicists using it because other programming languages, specially open source ones, tend to have a much larger community of users resulting in them seeing a faster development and having more tools available.

Research in astronomy and astrophysics has seen a strong shift to Python over the last decades. Nowadays AstroPy (Astropy Collaboration et al., 2013, 2018) offers a complete library of packages with many different methods to conduct research in a large diversity of areas in astronomy and astrophysics. In solar physics SunPy (Hughitt et al., 2012; Christe et al., 2019) offers dedicated libraries to work with data from solar observatories which is attracting the attention of many solar physicists. Recently, Bobra et al. (2020) published a work where the usage of different computational tools by solar physicists is discussed. In this study it can be seen that Python already shows a similar level of usage to IDL and over 50% of the respondents said they were currently working in both Python and IDL. Given that the development of Sunpy is at large it is unthinkable that IDL will see a significant usage on the solar physics community on the long term.

Since this work proposes to study energy injection in many ARs, it requires downloading, processing and storing a large volume of data. In `SQLite3` Python has a native connection to Structured Query Language (SQL) which is a programming language designed specifically for storing and managing data in a relational database. Then, given the specific needs of this work and also in a push to make an open source version of one of the most successful velocity inversion techniques available to the community, the first task was to port the original DAVE4VM to Python.

### 4.1.2 Porting the code

While designing the Python version the original code structure from DAVE4VM was initially translated to Python, keeping the code similar to the original version when possible, to facilitate a direct comparison between the two codes themselves. That approach is also more friendly to other people that already use DAVE4VM and may later want to migrate to the Python version.

The outputs of every operation were compared with the original IDL version in order to ensure that the code results were being properly replicated as the development of PyDAVE4VM took place. The window size adopted for the analysis in this thesis, is 21 pixels, as this is within the range where DAVE4VM was shown in Schuck (2008) to produce its more accurate results.

To illustrate the successful replication of DAVE4VM's operation a pair of observations of NOAA 12443 were taken as a final test set. For all of the convolution steps that were performed, with the resulting velocity products compared. A scatter plot is shown in Figure 19 comparing the velocities calculated for this test set by the original DAVE4VM and our PyDAVE4VM.

Once DAVE4VM was successfully ported into Python, and upon authorization of DAVE4VM author Dr. Schuck, all the modules were made available to the community using GitHub in the repository that can be freely accessed at: <https://github.com/Chicrala/pydave4vm>. The PyDAVE4VM repository also includes a pair of input data files (the same used to make Figure 19) that can be used to test the codes, a description of each individual module, guidelines for contribution, license and reference from the original version, and a presentation version of the code written using a Jupyter Notebook. The full set of modules that integrate the algorithms used to do this work are also available under an open source license so that people are free to download and modify, as long as any improvements that may result from the usage and individual development are given back to the community.

### **4.1.3 Optimizing the code**

Once the tests indicated that PyDAVE4VM could faithfully reproduce the results of DAVE4VM it was time to optimize the code by profiling the execution of every function and trying to improve their execution times. The vast majority of DAVE4VM processing time take place when calculating the matrix in the error metric function as its hundred different terms involve summing, multiplying and convolving the images of the vector magnetic field and products derived from them. The amount of mathematical operations with images (that can be rather large two dimensional arrays) in this step makes it a computationally demanding process.

Creating a version of an existing algorithm in another language is more than a work of translation as not only the syntax is different but also there are differences in the libraries that each language has available. A library, in the context of computer science, is a collection of resources

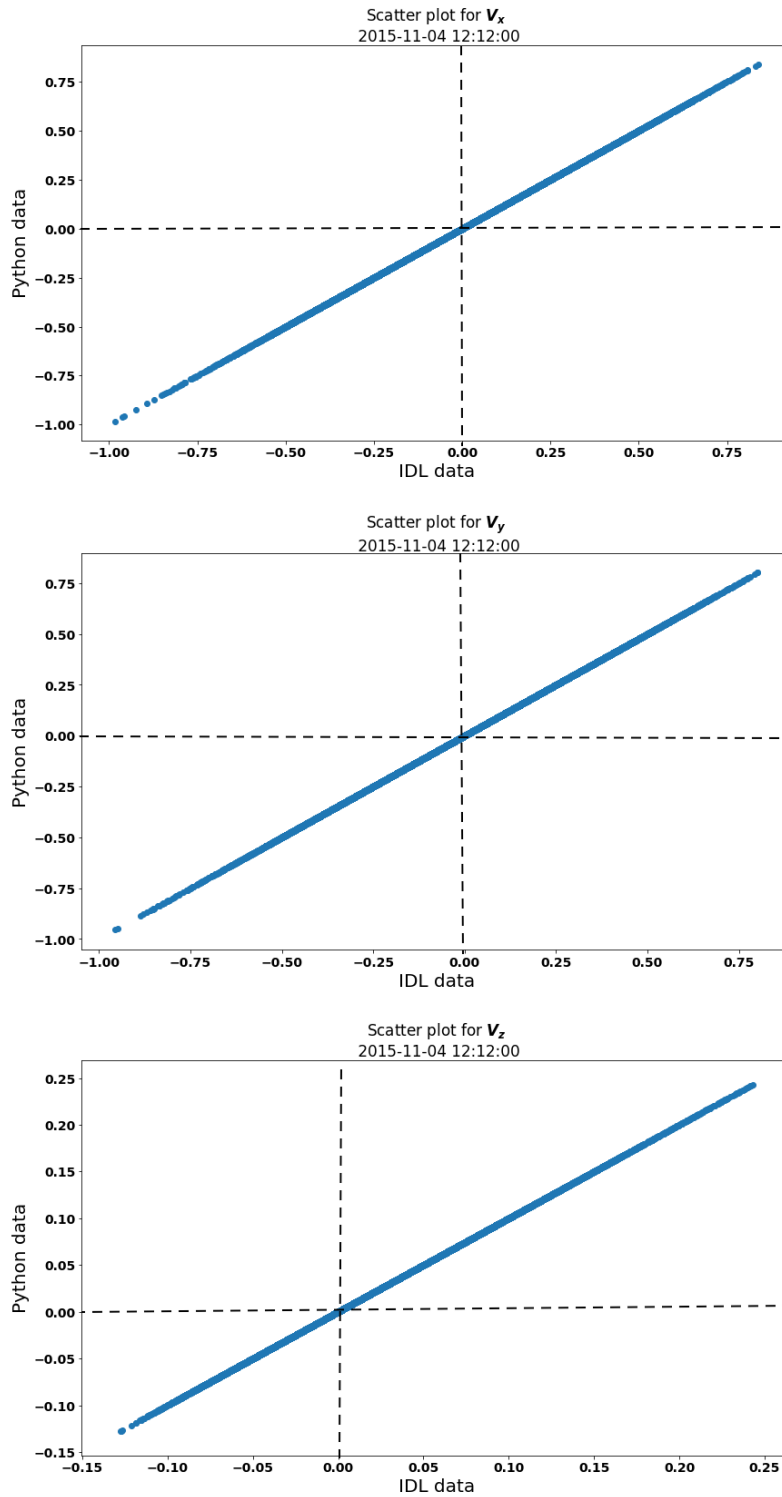


Figure 19: Scatter plots for the three velocity components ( $v_x, v_y, v_z$ ) calculated by Python and IDL versions of DAVE4VM. The calculation was performed using the SHARP data for AR NOAA 12443 on 2015-11-04 at 12:00 UT and 12:12 UT. It can be seen that the calculations from Python and IDL display an excellent correspondence.

in a programming language contain the pre-written codes, configuration data, documentation and other specific products that are necessary for an algorithm to be developed, distributed and maintained. Although libraries may be written with a common goal in mind, the way in which their sub-routines are tailored to perform the necessary calculations can deeply impact the overall performance of an algorithm. Since Python has a larger diversity of libraries when compared to IDL it was necessary to evaluate which routines would optimize PyDAVE4VM execution time, as even a difference of a few seconds quickly escalates to days when operating over a large data set.

In what a computer is concerned images are just an array of numbers and in Python there three main libraries that are commonly used to perform calculations with arrays being those NumPy (van der Walt et al., 2011), SciPy (Virtanen et al., 2020) and AstroPy (Astropy Collaboration et al., 2018). Then it was created three different versions using each the sub-routines of NumPy, SciPy and AstroPy to perform the calculations so that the execution times could be compared.

The execution time for a single pair of FITS files, which for these tests were the vector magnetic field from the SHARP data for AR NOAA 12443, dropped from over 2 minutes using either SciPy or AstroPy to around 20 seconds using NumPy to perform the calculations with arrays. NumPy produced the results significantly faster even when SciPy and AstroPy were set to work using a fast Fourier transform which is the fastest mode that these routines operate in. NumPy being the top performer is not a surprise though as NumPy is one of the most used libraries to work with arrays in the broader scope of computer science.

#### **4.1.4 Addons**

As this work involves more than obtaining velocities from vector magnetic field images some extra subroutines were created and also made available alongside the main PyDAVE4VM distribution. Here they will be shortly presented and described as they are part of the pipeline that process the data for the work in this thesis.

`check_fits` : compares the downloaded files with the list of files available over a given time range. If the number of files is less than what is expected for that time interval the routine tries to download the remaining files. Some missing files are not totally unexpected, as the spacecraft that carries HMI needs to undergo basic routines such as maneuvering that cause the data acquisition to be interrupted then.

`cubitos3` : create data cubes with the arrays of two successive images of the vector magnetic field and also create a separated object with the metadata.

`downloaddata` : uses a subroutine called `drms` to access the JSOC servers and download the data. Once the data is downloaded it checks and reports if there are any gaps in the downloaded file list considering the time range and cadence of the images. This code also attempts to download the missing files three times before logging them as missing.

`lightdb` and `maindb` : creates two slightly different relational databases with the `SQLite3` backend to store the products of the analysis. The difference between those two is that `lightdb` does not store the images. Details on the database will be covered in the next subsection.

`myconfig` : creates a configuration file that is required to run the pipeline. This configuration file contains the HARP number of the observations and the time range to download. This configuration file also sets the default temporal sampling of these images and window size to be used to ensure the integrity of the process.

`neutralline` : obtains the position and immediate vicinity of the polarity inversion lines based on the magnetic field gradient in the image and calculates the integrated magnetic flux and Poynting flux over these pixels.

`swpcparser` : read and extract the information for a given NOAA numbered AR, identified by cross referencing the information from the HARP bounding box coordinates and the image time stamps with the SWPC SRS and *Events* reports. This code requires that the user has these report `.txt` files available on their local disk.

`swpc_db` : create a database to store the information for every AR in the SRS and *Events* reports from SWPC.

`vperp` : calculates the velocity vector perpendicular to the magnetic field from the velocity vector obtained by PyDAVE4VM and the input vector magnetic field observations.

`poyntingflux` : calculates the Poynting flux based on the vector magnetic field observations and the velocity maps created by PyDAVE4VM.

Although these routines are not necessary to run PyDAVE4VM and reproduce the results of the original DAVE4VM, if the idea is to use the velocities as a byproduct to study the two components

of Poynting energy flux (as in Equations 3.7 and 3.8) then the `vperp` routine should be used. This routine uses Equations 3.15 and 3.14 to filter out the velocities that are parallel to the magnetic field and do not contribute to the energy injection. Then the calculation of the individual Poynting flux components as in Equations 3.16 and 3.17 can take place.

## 4.2 Results output database

HMI produces over 1200 observations for the full transit of an AR over the solar disk including, but not limited to, the images containing the full magnetic field vector. Emerging and decaying regions are an exception that will have shorter lifetime, and by consequence less observations related to them. However, the HARP data also track plage regions so for most emerging and decaying flux regions the data volume can still be close to 1200 images as the area occupied by plage regions is also tracked before their emergence and after their decay.

During the analysis 12 different image products are obtained for every two consecutive images that are used as input, those being: the three components of the mean magnetic field vector ( $B_x$ ,  $B_y$ ,  $B_z$ ), the three components of the velocity vector ( $v_x, v_y, v_z$ ), the three components of the velocity vector perpendicular to the magnetic field ( $v_{\perp x}, v_{\perp y}, v_{\perp z}$ ) and the two components of the Poynting flux and their total ( $S_{\perp n}, S_{\perp t}, S_{\perp s}$ ). Therefore, the demand for space to store the data scales quickly with the number of ARs that are being studied, with all the data derived from a single region can occupy over 10 GB (depending on the HARP bounding box size and the amount of observations associated to the region).

To store and organize all these data the SQL database was designed so that the information obtained by the HMI observations, the SWPC SRS and the *Events* reports could be distributed in three different tables where the information for each AR is connected via their NOAA and HARP numbers. Some HARPs may have more than a single NOAA number and the database also accounts for that, creating appropriate links between the products derived from HMI observations and the information mined from the SWPC SRS and *Events* reports.

Some of the most common tools to create and interact with a SQL database include MySQL and PostgreSQL that allow the creation of a server inside the computer memory to store the data, and SQLite3 that uses a file on disk and is native to Python. SQLite3 proved to be a more suitable

tool since the data needed to be stored in an external hard drive and it allows the database to be constructed in a single file instead of a server.

The mobility offered by using SQLite3 does not come without some shortcomings, the most significant of them being that the query times escalate quickly with the database size. With the amount of data expected to be close to 4 TB, images were then organized and stored outside the database although all the integrated and text products derived from them (including the HMI metadata of each observation) were kept in the HMI observations table in the database. Without the images the final size of the database was expected to occupy hundreds of MB which is significantly lower than the 4 TB initially estimated. The algorithm used to create the database and also its schema is available at the `lightdb` routine. The `maindb` routine can create the database file with the columns to accommodate images.

It was also necessary to evaluate and test options to save the images to disk so that they could not only be efficiently stored but also quickly loaded. By testing the space that was necessary to store every image as either a NumPy save file, a text file (.txt) and comma-separated value file (.csv), it was verified that the images saved as text files were occupying significantly less space than the other two options (almost three times smaller than the same images written as a NumPy save files). The time to open and operate on each image was similar regardless of the written file format, so all the images were saved as text files.

A separate database was also created containing information from all the ARs tracked by the SWPC SRS and *Events* daily reports so that this database could be mined for general properties of all the ARs that were observed during the HMI era. The algorithm used to create the database and also its schema is available in the `swpc_db` routine. Having access to the general properties of the ARs from the HMI era proved to be invaluable to select the ARs featured in this study.

### 4.3 The pipeline

Automating the data download, processing and storage was a key element in this work because high volumes of data were required to build the database. The automation also makes the process more consistent and less prone to errors. In this section the pipeline is described as it was implemented for the `lightdb` as this was the database used. The blueprints and a pipeline for the `maindb`,

```
[Parameters]
harpnum = 3688
tstart = 2014.01.25_00:00:00
extent = 30d
cadence = 720s
dbaddress = sqlite:///../testdb.db
window_size = 21
```

Figure 20: Example of a PyDAVE4VM pipeline configuration file.

that stores the images inside the database, are also available in the GitHub. The basic idea behind the pipeline is that from a single configuration file the algorithm will have enough information to be able to download, process, and store the data using the tools described above. An example of a configuration file, that is encoded using JSON and can be created using the `myconfig.py` routine, can be seen in Figure 20. The parameters mentioned above can be described as being:

- `harpnum`: JSOC HARP number;
- `tstart`: Date-time stamp to start searching for observations;
- `extent`: Time window to look for observations on JSOC databases. 30d corresponds to 30 days;
- `cadence`: Desired separation between two consecutive observations (i.e., temporal sampling);
- `dbaddress`: Local address of the results output database;
- `window_size`: DAVE4VM configuration parameter for velocity calculation.

From the configuration file only the `harpnum` and `tstart` parameters were being modified so that the code could look for new regions. The other parameters maintained the following default values to ensure that the processing would be consistent between the different HARPs: 30 days for `extent` which is more than enough to cover the whole period that any AR would be on the disk (i.e., approximately 14 days for an east-to-west-limb passage), 720 seconds for `cadence` which is the best temporal sampling HMI can provide, 20 pixels for `window_size`.

The pipeline work flow is illustrated in Figure 21. From the configuration file the `Call_vn` module will query JSOC and download the data using the `drms` protocol presented as an HMI nugget by K. Glogowski & M. G. Bobra in 2016<sup>1</sup>.

<sup>1</sup><http://hmi.stanford.edu/hminuggets/?p=1757>

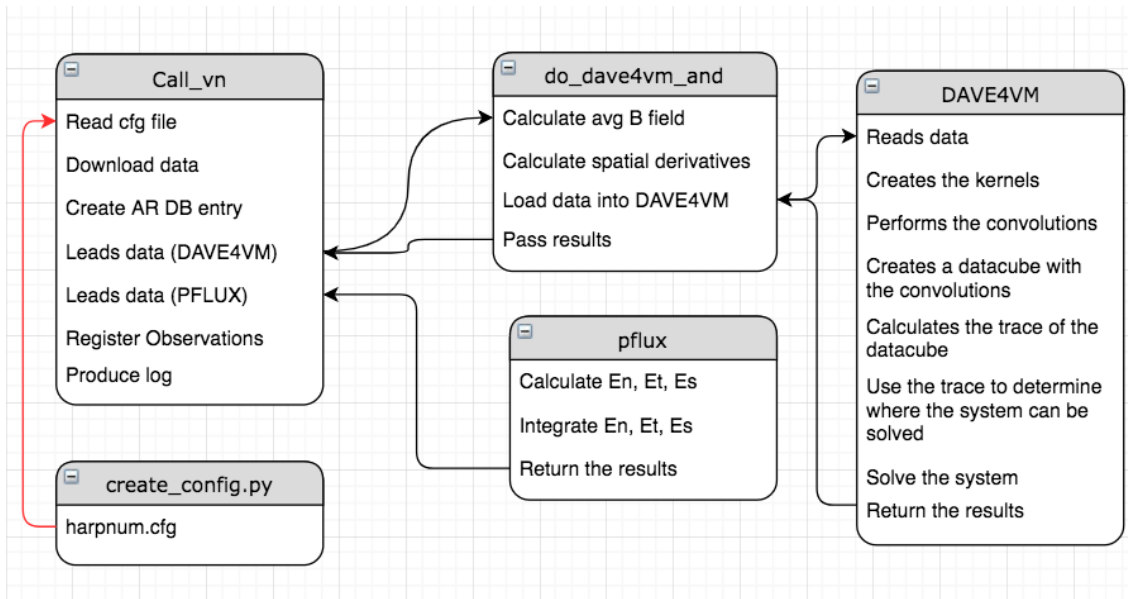


Figure 21: This diagram illustrates how the main modules used to conduct the analysis over the set of observations of an AR communicate between themselves.

The data files are used to obtain the HARP number and check if the database already has readings for that AR and, if not, it creates a new entry. Each pair of observation times are checked to be sure that all three magnetic components are available for both time stamps. These are then passed into the modules that call PyDAVE4VM. Once the 3D velocity vectors are obtained, they are combined with the 3D magnetic vectors to calculate the Poynting flux (see Section 3.1.4).

These derived quantities are then registered into the database with their respective time stamp. The time stamp and the location of the HARP on the solar disk (extracted from the SHARP metadata) are used to search for co-spatial NOAA numbers in the SWPC files. The NOAA number is then used to query the database with the SWPC products to copy any entries from the Events and Morphology of the region which contain the information from the SRS and Events reports. This process keeps going over all consecutive time stamp pairs until the entire series for a HARP number is finished.

All the actions performed in the Call\_vn module are tested and logged according to their outcomes so that each individual HARP number will produce a log file of their processing, greatly facilitating any debugging that may be needed.

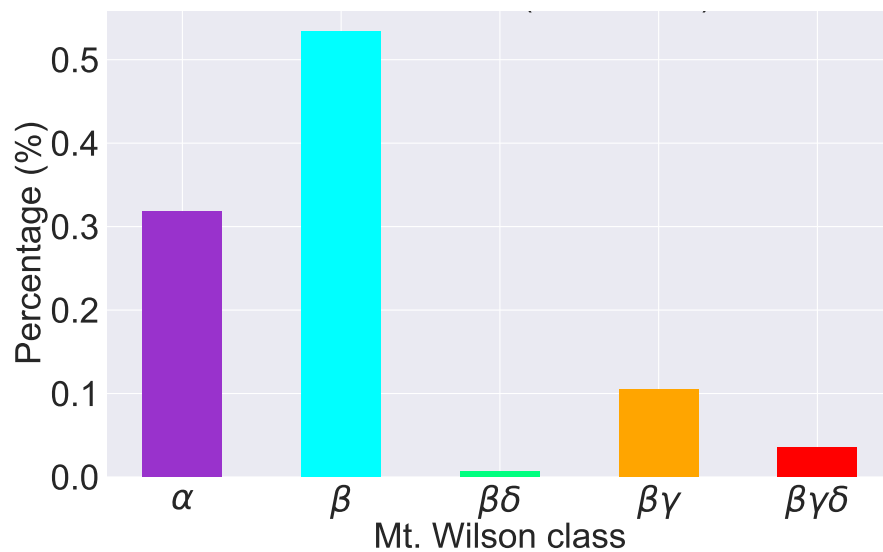


Figure 22: Mt. Wilson classification of the whole dataset of NOAA regions from the beginning of the HMI coverage in 2012 to the end of 2018.

### 4.3.1 Selecting regions

As this work proposes itself to strive for a more general description of energy injection in ARs there are essentially two ways which a dataset can be selected to achieve the objective. The first, and most straightforward method, is to process the data and study the results from all the SHARP regions. This approach would demand a considerably large processing time and storage capacity that are unrealistic when compared to the time and resources available. An alternative, and more efficient approach, is to choose a sample of ARs that portray what was typically observed by HMI.

Obviously, being complex magnetic structures, ARs have dozens of different properties from which the question of “What is commonly observed by HMI?” can be asked. One of the most common ways used to distribute ARs into classifications is by studying their morphology, as discussed in Chapter 1. This is particularly convenient because the SWPC SRS reports contain the daily Mt. Wilson classification of every AR that was observed on the disk that day.

The first step in selecting the ARs to construct the dataset is to understand how the Mt. Wilson classifications of ARs are distributed since the HMI coverage started in 2012. Figure 22 shows a histogram with the Mt. Wilson classification of all the NOAA regions that were on the disk from 2012 until the end of 2018.

The regions selected for this study were then picked according to their Mt. Wilson classification so that the majority of ARs that comprise the dataset were designated as  $\alpha$  or  $\beta$  as these are most commonly observed on the disk. Coverage time was also taken into consideration, as some emerging and decaying ARs have only a couple of days of observations that would undermine the study of their energy dynamics. However, a larger proportion of more complex regions ( $\beta\gamma$ ,  $\beta\delta$  and  $\beta\gamma\delta$ ) were also introduced so that they could have a slightly larger representation, because in a strictly proportional sample their numbers would be too small to realistically attempt to understand their behaviour in a broader sense. Also, the strongest flares observed during this time period (as is usually the case in most solar cycles) were often linked to regions with the more complex Mt. Wilson classifications.

Using the information available in the SWPC database it was then possible to determine which regions would be processed by the pipeline to produce results that are coherent with the ARs that marked the 24th solar cycle. The final dataset contains observations from over 80 HARP numbers that contain over a hundred different NOAA regions. It is not uncommon for the image space of a single HARP to contain more than one NOAA region, although that number doesn't normally exceed two.

## **Chapter 5**

# **Case study of the Poynting flux of 3 flaring and 5 non-flaring ARs**

In this chapter the major works that studied the photospheric Poynting flux will be discussed so a specific understanding can be built of what is currently known. This offers a basis for comparison between the values related to the Poynting flux obtained so far and the results presented later in Chapters 6 and 7. Poynting flux values for the corona and chromosphere are also discussed as they are directly above the photosphere, feeding on its energy output. Works can be separated into three different eras according to their level of access to measurements of the photospheric magnetic field: the SDO era, the MDI era and the ‘legacy’ era. After that, results obtained using a subset of regions in the database is presented and discussed. These are the results that guided the formulation of the questions that would be then used to investigate the complete dataset.

### **5.1 History of solar Poynting flux measurements**

#### **5.1.1 Poynting flux before modern instrumentation (legacy era)**

Many of the most complex problems in solar physics are related to exchanges of, but not limited to, energy or mass. The main motivation behind the first works concerned specifically with how much energy was being injected through the photosphere was explaining the coronal heating. More commonly those estimates were looking at the energy exchanges in the chromosphere and corona but those are also helpful to understand the photospheric Poynting flux.

Table 4: A comparison between the energy exchange in the chromosphere and corona. Adapted from Withbroe and Noyes (1977).

Parameter	Quiet Sun	Active Region
Coronal energy losses ( $\text{erg cm}^{-2} \text{s}^{-1}$ )		
Conductive flux	$2 \times 10^5$	$10^5 - 10^7$
Radiative flux	$10^5$	$5 \times 10^6$
Solar wind flux	$\leq 5 \times 10^4$	$< 10^5$
Total coronal loss	$3 \times 10^5$	$10^7$
Chromosphere radiative losses ( $\text{erg cm}^{-2} \text{s}^{-1}$ )		
Low chromosphere	$2 \times 10^6$	$\geq 10^7$
Middle chromosphere	$2 \times 10^6$	$10^7$
Upper chromosphere	$3 \times 10^5$	$2 \times 10^6$
Total chromospheric losses	$4 \times 10^6$	$2 \times 10^7$

Some of the earliest estimations of energy exchange in the photosphere were provided by Piddington (1956) while investigating the influence of waves in the heating of the solar atmosphere. The author estimated that atop granules the energy flow was  $\sim 5 \times 10^6 \text{ erg cm}^{-2} \text{ s}^{-1}$  and on average over the solar surface this value is one order of magnitude smaller, being  $\sim 5 \times 10^5 \text{ erg cm}^{-2} \text{ s}^{-1}$ . Piddington (1956) points out that this energy flow could propagate over distances larger than  $10^4 \text{ km}$  above the photosphere.

Osterbrock (1961a) estimated that  $3 \times 10^7 \text{ erg cm}^{-2} \text{ s}^{-1}$  are injected from the convection zone through sound waves, although the author indicates that turbulence in the velocity field make the estimation highly uncertain. In another publication Osterbrock (1961b) simulates a diversity of scenarios of energy transfer in the chromosphere and estimates that waves can bring up to  $3 \times 10^8 \text{ erg cm}^{-2} \text{ s}^{-1}$  to the chromosphere, although these values can be orders of magnitude lower depending on the region that is being observed and is more commonly found to be  $\sim 4 \times 10^7 \text{ erg cm}^{-2} \text{ s}^{-1}$ . Kuperus (1969) later estimated the total flux leaving the chromosphere as  $5.6 \times 10^6 \text{ erg cm}^{-2} \text{ s}^{-1}$ .

In the mid 1970s, some observations obtained from the Skylab station started to support the efforts in solar physics. Withbroe and Noyes (1977) estimated that the Sun has a heat input of  $(5 - 8) \times 10^5 \text{ erg cm}^{-2} \text{ s}^{-1}$  with most of this energy employed to expand the coronal gas. Athay (1976) provided some estimates for the energy loss in the corona and the chromosphere that are summarized in Table 4.

### 5.1.2 Proxy Poynting flux (MDI era results)

During the MDI era the data used to calculate the velocities, and thus the Poynting flux, were limited to LOS magnetograms. Then, the works published contributed with the first results of the Poynting flux in ARs produced from observations which, until then, were exclusively studied with simulations. These works also started bringing in more estimations and measurements of the Poynting flux specifically for the photosphere, although most works tend to focus their discussions in other results derived from MDI data such as the magnetic field helicity.

Tan et al. (2007) presented a work exploring the statistical correlation between a range of different parameters that can be calculated from the photospheric magnetic field and coronal soft X-ray brightness. Although the authors include a discussion on the Poynting flux the discussion is more focused on magnetic helicity. The dataset used by Tan et al. (2007) included more than 160 ARs consisting of regions with a NOAA designation and also small regions that have a well defined bipolar flux. LCT was used on MDI magnetograms to estimate the horizontal velocities and then calculate the Poynting flux and magnetic helicity of these regions. Tan et al. (2007) found values that are ranging from  $10^{6.7}$  to  $10^{7.6}$  ergs cm<sup>-2</sup> s<sup>-1</sup> for the proxy Poynting flux. These values are, as pointed out by the authors, consistent with the energy demands of coronal heating and also enough to cover previous estimates of the energy losses in the chromosphere and corona (see Table 4 adapted from: Withbroe and Noyes, 1977). Exploring the coronal X-ray brightness, Tan et al. (2007) found that among all the different results the proxy Poynting flux scored the highest correlation with the average value of the soft X-ray brightness. The correlation between the proxy Poynting flux and coronal X-ray brightness found by Tan et al. (2007) is reproduced in Figure 23.

In another statistical study, Welsch et al. (2009) used a sample of 46 different ARs, all of which had a NOAA designation, to explore the relationship between photospheric flow fields and solar flares. Among the different quantities that can be derived from the photospheric flows Welsch et al. (2009) brought a greater focus to the proxy Poynting flux unlike works that preceded it. By studying the relationship between the velocities estimated using LCT and the observed magnetic field features, it was noticed that the higher values of speed had a higher occurrence in regions with weaker fields. However, the correlation found between speed and field strength is weak, meaning that the values calculated for speed may vary largely regardless of the magnetic field strength. A comparison

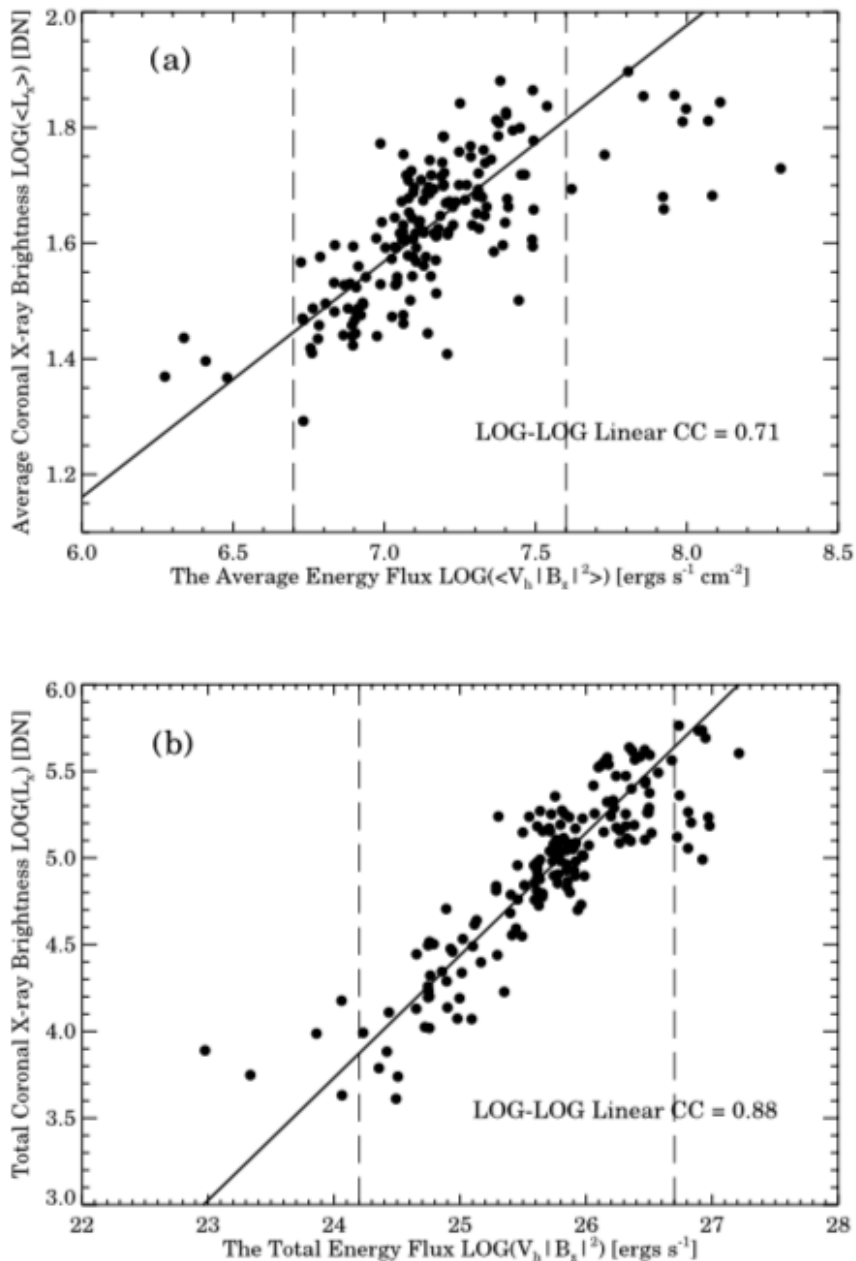


Figure 23: (a) Area-averaged and (b) area-integrated scatter plots showing the correlation between Poynting flux and coronal X-ray brightness. Source Tan et al. (2007).

between the different features that were extracted from the photospheric LOS magnetic field and flares show that the proxy Poynting flux have one of the strongest correlations with the occurrence of flares. The coefficient of determination used by Welsch et al. (2009) is calculated as the linear correlation coefficient squared and its value is approximately 0.25 between the flare occurrence and the proxy Poynting flux. Although the proxy Poynting flux showed the best correlation with flares, the coefficient of determination shows that the proxy Poynting flux by itself is not enough

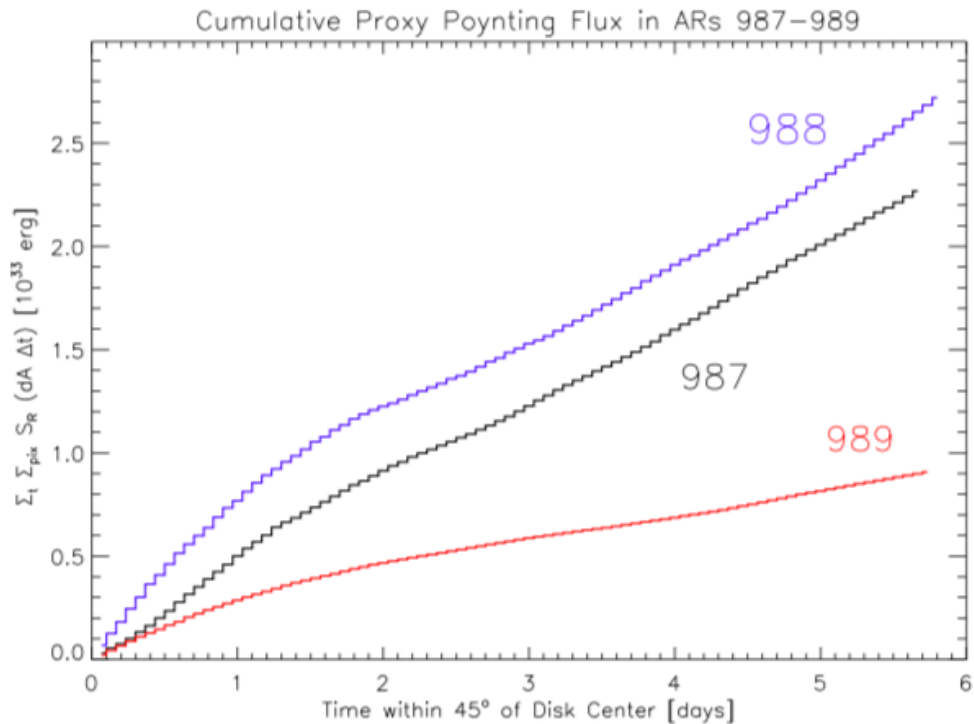


Figure 24: Sum over time of the proxy Poynting flux ( $S_R$ ) multiplied by pixel area ( $dA$ ) and the time between magnetograms ( $\Delta t$ ). Source Welsch et al. (2011).

to explain and predict flare activity.

Using a set of three different ARs with different flare and CME records, Welsch et al. (2011) studied and compared the energy injection of these regions with MDI LOS magnetograms. The three regions featured in this study are NOAA 10987, 10988 and 10989 where only NOAA 10989 produced flares above C-class including one M-class flare. As Welsch et al. (2011) mention there was an initial assumption that the level of energetic activity exhibited by an AR would be somehow connected to its energy dynamics. However, their results suggest that the number of energetic events produced by an AR does not directly correspond to the amount of energy that was injected in it. The evolution of the ARs studied there can be seen in Figure 24. Welsch et al. (2011) points that, given the small sample size, this may simply be a particular case which creates a natural demand to explore this relationship over a significantly larger set.

Case studies that included a discussion on the energy injection driven by the photospheric Poynting flux of an AR were presented by Li et al. (2010) and Fan et al. (2011). Presenting a study that features AR 8038 that produced three CMEs over its passage over the solar disk in May of 1997, Li et al. (2010) found that the AR accumulated an energy of  $1.6 \times 10^{32}$  erg by integrating the

proxy Poynting flux. This energy accumulation happened over the 66 hours that preceded a C1.3 flare, showing that the amount of energy that is normally released in an event such as a flare or a CME may take multiple days to be injected into the AR. Studying NOAA region 10930 that produced an X3.4 flare, Fan et al. (2011) calculated its proxy Poynting flux using data-driven simulations. The data used by the simulations were obtained from Hinode and were able to retrieve not only the proxy Poynting flux but also the radial Poynting flux and the Poynting flux magnitude. The different Poynting flux products derived by Fan et al. (2011) were found to display a similar behaviour for most of the sunspot area, the exceptions being regions with strong sunspot rotation and flux emergence.

### 5.1.3 Poynting flux in modern times (SDO era)

Once measurements of the full magnetic field vector were routinely made available by SDO, it was possible to calculate the velocity fields with more accuracy and also to study both the emergence and shearing components of the Poynting flux. This section discusses some of the Poynting flux results that were obtained when their calculations included removing the field-aligned velocities from the velocity vector that is obtained using LCT methods as they do not contribute to energy injection (see Chapter 3).

In a study featuring two ARs, NOAA 11072 and 11158, Liu and Schuck (2012) were already making use of DAVE4VM to obtain the velocity fields and, thus, both the emergence and shearing terms of the Poynting flux. The authors observed that between the two components of the Poynting flux the emergence term was consistently injecting more energy than its shearing counterpart. In the time period over which both regions were studied, the normal Poynting flux was responsible for close to 60% of the total energy accumulated. Following this work, Liu et al. (2014) then applied similar methods to study the helicity and energy evolution of a larger set composed of 28 ARs, all of which were emerging bipolar regions. Helicity also can be divided into two components that are dependent on the emergence and shearing plasma motion (as discussed in Chapter 1). Comparing the role of emergence and shearing motions to the injection of helicity and energy the authors found distinct behaviours between the two quantities. Most of the energy was injected by emergence (54% of the total) while helicity is mostly injected by shearing (86% of the total).

Most works that can be found in the literature that make use of DAVE4VM and/or LCT techniques to obtain the photospheric flows in order to investigate the evolution of ARs are case studies of a single AR. Case studies can provide meaningful insight on the physics that govern the energy dynamics of an AR and its possible connection with flares and/or CMEs. However, case studies have a limited capacity to offer insights that can be used to explain the general behaviour of energy injection in ARs as they can be considerably different from each other. Additionally, most studies that use DAVE4VM or LCT focus their discussions on helicity, although the calculation of helicity is remarkably similar to the one necessary to obtain the Poynting flux.

Tziotziou et al. (2013) bring forward a study on the evolution of magnetic energy and relative helicity in NOAA 11158 that produced a series of eruptions. In that work it was found that there was a transient decrease in the energy budget of NOAA 11158 as a result of the eruptions, but within hours after the eruptions took place this energy deficit was recovered due to the energy injection. Comparing the contributions given by the emergence and shearing terms of the Poynting flux in NOAA 12283, Romano et al. (2015) found that most of the energy injection was facilitated by the shearing component. This result offers some contrast to what was found by Liu and Schuck (2012) and Liu et al. (2014), in which the studied ARs saw most of their energy being injected by emergence. However, this result is not unreasonable because one of the spots of NOAA 12283 was clearly observed to be rotating with a high angular velocity while also presenting a fast relative motion within the AR.

A different approach to using LCT to obtain the energy injection consists of calculating the Poynting flux directly through a cross product of the magnetic and electric field vectors (Equation 3.1). This was used by Kazachenko et al. (2015) to study NOAA 11158 around the time when it produced an X2.2 flare (the same AR studied by Tziotziou et al. (2013)). The electric fields were calculated using the observed Doppler velocities and also horizontal velocities obtained through FLCT from the vector magnetic field data. The energy flux in the pre- and post- flare instants observed by Kazachenko et al. (2015) were on the order of  $10^9 - 10^{10} \text{ erg cm}^{-2} \text{ s}^{-1}$ . However, during other portions of the energy flux of NOAA 11158 time series the rate at which energy was being injected was significantly smaller (on the order of  $\sim 10^8 - 10^9 \text{ erg cm}^{-2} \text{ s}^{-1}$ ).

Works that study the Poynting flux specifically in plage regions were presented by Yeates et al. (2014) and Welsch (2015) that used distinctly different approaches to produce two case studies

on two different regions of plage associated with NOAA 10930. Yeates et al. (2014) calculated the Poynting flux through data driven simulations, finding that the values obtained could vary considerably depending on the boundary conditions set ranging from  $\approx 10^6$  erg cm<sup>-2</sup> s<sup>-1</sup> to an upper bound of  $3.5 \times 10^8$  erg cm<sup>-2</sup> s<sup>-1</sup>. Yeates et al. (2014) points out that the lower values are a representation of a more realistic domain size for a plage region but that the Poynting flux in plage can vary by a couple orders of magnitude depending on how strong the plasma motions are in those regions. The average value reported by the author using the simulation was  $1.7 \times 10^7$  erg cm<sup>-2</sup> s<sup>-1</sup> but it's important to consider that the average was taken over a spatial location that contained more significant oppositely signed values (i.e., up to  $\pm 6 \times 10^8$  erg cm<sup>-2</sup> s<sup>-1</sup>). These statements are in accordance to what is reported by Welsch (2015) who found an average  $S_n$  of  $(5 \pm 1) \times 10^7$  erg cm<sup>-2</sup> s<sup>-1</sup>, obtained using calculations derived from LCT using Hinode data for another portion of plage in the same AR.

An investigation on flare-induced rotation of the sunspots in NOAA 12371 was presented by Liu et al. (2016) using DAVE and DAVE4VM to calculate the velocities and also Poynting flux. That study observed that some of the spots showed a rotation speed close to 50° per hour which greatly impacted the AR energy dynamics. During the flare start the Poynting flux values integrated over the observed area were  $1 \sim 5 \times 10^{28}$  erg s<sup>-1</sup> quickly inverting its ongoing trend showing then a sharp energy removal  $-5 \sim 10 \times 10^{28}$  erg s<sup>-1</sup>. After the flare took place the energy levels went back to the levels that were previously being observed.

Su et al. (2018) presented a case study of NOAA 12396 that produced a sequence of five C-class flares over its passage through the solar disk. The values of the emergence and shearing components of the Poynting flux integrated over the observed area were found to have similar values around  $3 \times 10^{27}$  erg s<sup>-1</sup>. The proportion of energy being injected by emergence and shear motions is again showing a different behaviour from what was observed so far by the ARs in Liu and Schuck (2012), Liu et al. (2014) and Romano et al. (2015).

Studying a set of 16 NOAA regions, Bi et al. (2018) explored how the magnetic helicity and energy flux evolved in a time period of 2 hours around 16 flares, all of which were lower than a M5.0 class. Most of the discussion in Bi et al. (2018) are referring to the 4 M-class flares in the set and exploring the changes in helicity. In those 4 M-class flares the dominant contribution for both helicity and energy flux was mostly being given by the shearing component. During two of

the four M-class flares, impulsive changes were observed in the emergency term of the Poynting flux. The Poynting flux had positive values up to when the flares took place where it inverted its injection trend reaching negative values in all four cases going back to display positive values after the impulsive phase finished.

## 5.2 The data set

The sample set chosen to conduct an initial investigation into the general properties of AR poynting flux consists of 8 different ARs: 3 flaring (NOAA numbers 11593, 12644, and 12443) and 5 non-flaring (NOAA numbers 11642, 11835, 11896, 12337 and 12581). The 3 flaring regions are quite distinct between themselves in size and complexity, while they also displayed different levels of flaring activity as they passed over the solar disk. The 5 non-flaring regions do not have any entries in the SWPC reports for flare activity associated to them at any point in their disk passage.

NOAA 12644 (the intermediate region of the flaring ARs) is an emergent region and its dataset includes all of its lifetime ranging from some days prior to its emergence and first NOAA designation to some days after it produced an M-class flare. This region then provides a relatively rare opportunity to observe the full energy build-up prior to a major flare.

All the regions selected vary not only in activity but also in Mt. Wilson class and spot area. From the daily classifications issued to the regions over their lifetimes most are either  $\alpha$  or  $\beta$ , although the two regions that produced M-class flares (NOAA numbers 12443 and 12644) received more complex designations for some days of their lifetimes. The area of a sunspot is measured by SWPC in units of millionths of the solar hemisphere ( $\mu\text{Hem}$ ) which is approximately 3 million square kilometres. A large-sized sunspot is defined by Mandal and Banerjee (2016) as any sunspot with area larger than 200  $\mu\text{Hem}$  and the largest sunspots are those with an area larger than 500  $\mu\text{Hem}$ . Most non-flaring ARs are modest in size with an average spot area around 100  $\mu\text{Hem}$ , with the exception of NOAA 12337 that is only 16  $\mu\text{Hem}$ . The two M-class flaring ARs are about 2 – 3 times larger than the non-flaring regions. However, NOAA 11593 that produced 10 C-class flares is only 39  $\mu\text{Hem}$  in spot area (comparable in size only with the smallest non-flaring region, NOAA 12337) which is almost ten times smaller than the largest AR (NOAA 12443). A summary with the number of flares each region produced, characteristic size (in terms of lifetime-average spot

Table 5: Summary of the ARs featured in this work showing NOAA number designation, number of GOES flares produced by the AR, lifetime-average spot area expressed in millionths of the solar hemisphere, and daily Mt. Wilson class.

NOAA Region Number	Number of Flares in GOES Classes			Lifetime-Average Spot Area ( $\times 10^{-6}$ hemisphere)	Daily Mt. Wilson Classification (Days from Central Meridian crossing: negative before, positive after)												
	B	C	M		-6	-5	-4	-3	-2	-1	0	1	2	3	4	5	6
11593	...	10	...	39	...	$\alpha$	$\alpha$	$\alpha$	$\alpha$	$\beta$	$\beta$	$\beta$	$\beta$	$\alpha$	$\alpha$	...	...
12644	14	4	1	236	...	...	...	...	$\beta$	$\beta\gamma$	$\beta$	$\beta$	$\beta$	$\beta$	$\beta$	$\beta\gamma$	$\beta\gamma\delta$
12443	2	40	1	362	...	$\beta$	$\beta\gamma\delta$	$\beta\gamma\delta$	$\beta\gamma$	$\beta\delta$	$\beta\delta$	$\beta\delta$	$\beta$	$\beta$	$\beta$	$\beta$	$\beta$
11642	...	...	...	89	...	$\alpha$	$\alpha$	$\alpha$	$\alpha$	$\alpha$	$\alpha$	$\alpha$	$\alpha$	$\alpha$	$\alpha$	$\alpha$	$\alpha$
11835	...	...	...	141	$\alpha$	$\alpha$	$\beta$	$\beta$	$\beta$	$\beta$	$\beta$	$\beta$	$\beta$	$\beta$	$\alpha$	$\beta$	$\beta$
11896	...	...	...	126	...	$\alpha$	$\alpha$	$\alpha$	$\alpha$	$\alpha$	$\alpha$	$\alpha$	$\beta$	$\alpha$	$\alpha$	$\alpha$	$\alpha$
12337	...	...	...	16	...	...	$\alpha$	$\beta$	$\beta$	$\beta$	$\beta$	$\beta$	$\beta$	$\beta$	...	...	...
12581	...	...	...	100	...	...	...	...	$\beta$	$\beta$	$\beta$	$\beta$	$\beta$	$\beta$	$\beta$	$\alpha$	$\alpha$

area), and daily magnetic complexity (i.e., Mt. Wilson class) can be found in Table 5.

As discussed in Chapter 1, measuring the magnetic field vectors close to the solar limb is particularly challenging due to the  $180^\circ$  azimuth disambiguation problem. The HARPs produced and published by the HMI science team include measurements up to when the regions either submerge or disappear beyond the solar West limb. Then, in order to avoid some of the errors introduced by the disambiguation problems, the analysis here only consider SHARPs with field-of-view centroids (i.e. the latitude in the middle of the HARP box) that lie between  $\pm 70^\circ$  heliographic longitude. In addition, some later figures will indicate the  $\pm 50^\circ$  longitude mark. These constraints were determined by visual inspection of movie sequences created with the vertical magnetic field ( $B_r$ ) data for every AR in the dataset. The limit chosen corresponds to the longitude where patches of pixels can be seen flipping between the two disambiguation solutions in successive frames. It is worth noting that a HARP with a centroid at, e.g.,  $50^\circ$  longitude will often have a HARP FOV that still extends out to  $\sim 60^\circ - 65^\circ$  longitude, given the typical size of HARP bounding boxes.

### 5.3 The impact of removing field-aligned flows

In Chapter 3 it was discussed that velocities aligned with the magnetic field do not contribute to energy injection, and these must be removed from the velocity fields obtained from velocity inversion methods for the accurate calculation of the two Poynting flux components. In this section, how this removal process affects the calculation of velocity and Poynting flux will be studied.

Figure 25 shows the impact caused by removing the field-aligned velocities from the velocity field vector for a sample observation of NOAA 12443 (the largest and most complex AR in this data set) for one time stamp (2015-11-04 12:10 UT; when this AR was close to disk center). The left hand column of Figure 25 contains scatter plots between each component of the velocity vector as calculated by PyDAVE4VM ( $v_x, v_y, v_z$ ) and the velocity vector that remains after the field-aligned flows are subtracted ( $v_{\perp x}, v_{\perp y}, v_{\perp z}$ ) as in Equations 3.14 and 3.15. The right hand column of Figure 25 shows the images of the difference between these velocities (in red/blue) overlaid on the vertical field to show what magnetic features are associated with the largest differences.

The impact on the velocities can be seen across all components of the velocity vector illustrated in Figure 25. However, looking at the scatter plots it can be noticed that the impact on the vertical

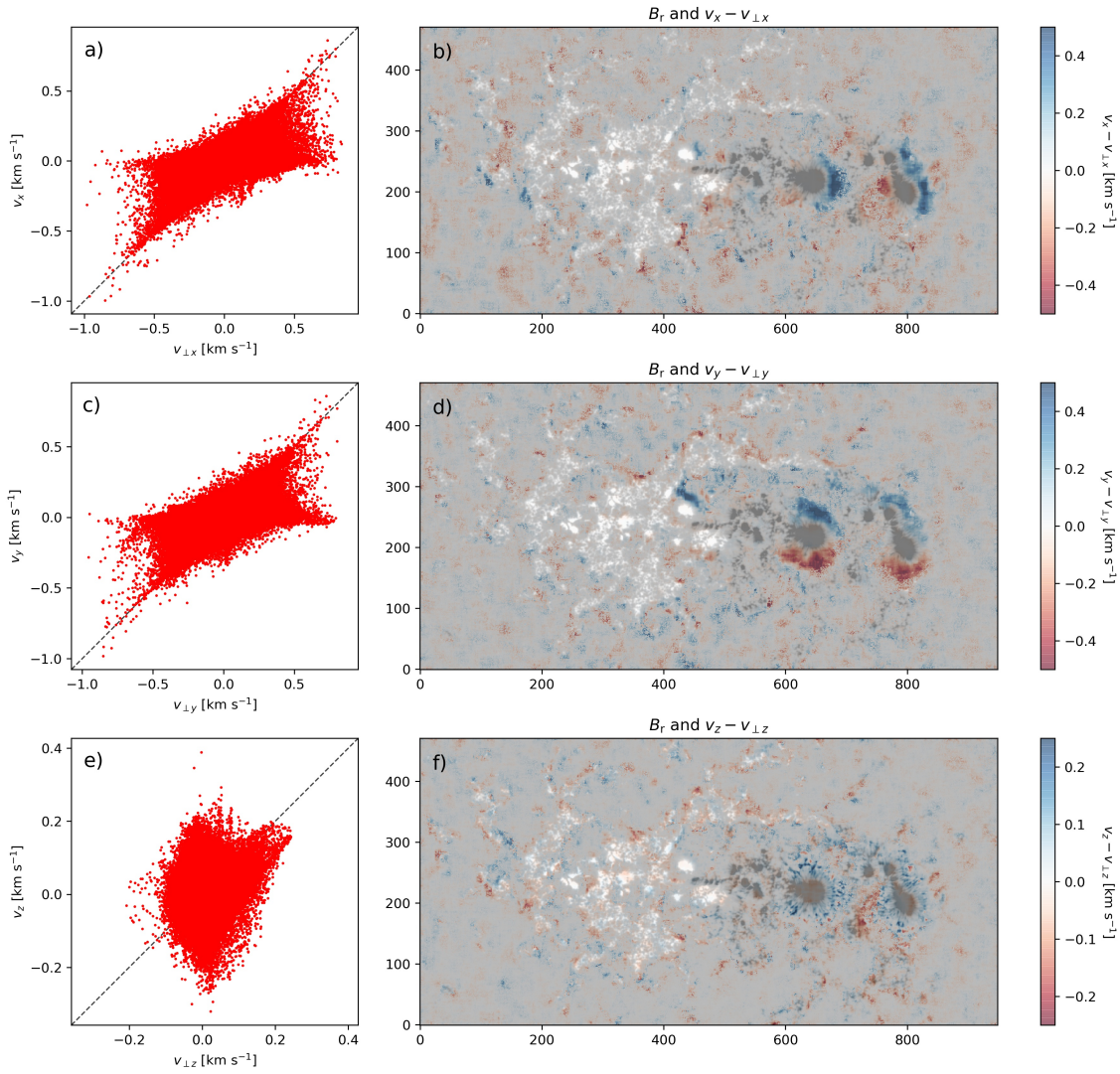


Figure 25: Left: Scatter plots between the velocities obtained by DAVE4VM before and after using Equations 3.14 and 3.15 to remove the field aligned components. Right: difference between the velocities before and after removing the field aligned velocity atop the image of the vertical magnetic field. To improve visualization the values in the colorbar were clipped for horizontal and vertical velocities at, respectively, 0.5 and 0.25 km s<sup>-1</sup> which represents less than the full extent of the differences as it can be seen in the scatter panels.

velocity (panel e) is relatively different from those observed in the horizontal velocity components (panels a and c) that are similar between themselves. In panels b and d, the differences in the horizontal velocities ( $v_x - v_{\perp x}$  and  $v_y - v_{\perp y}$ ) are, for the majority of pixels, below  $\pm 0.2$  km s<sup>-1</sup> although this difference can surpass  $\pm 0.5$  km s<sup>-1</sup> for some pixels. The largest differences in horizontal velocities are located around the two leading spots and are more intense than the differences in vertical velocities (panel f). The differences in vertical velocities are, on the majority, below  $\pm 0.1$  km s<sup>-1</sup> although some values can be over  $\pm 0.2$  km s<sup>-1</sup>. The differences observed for the

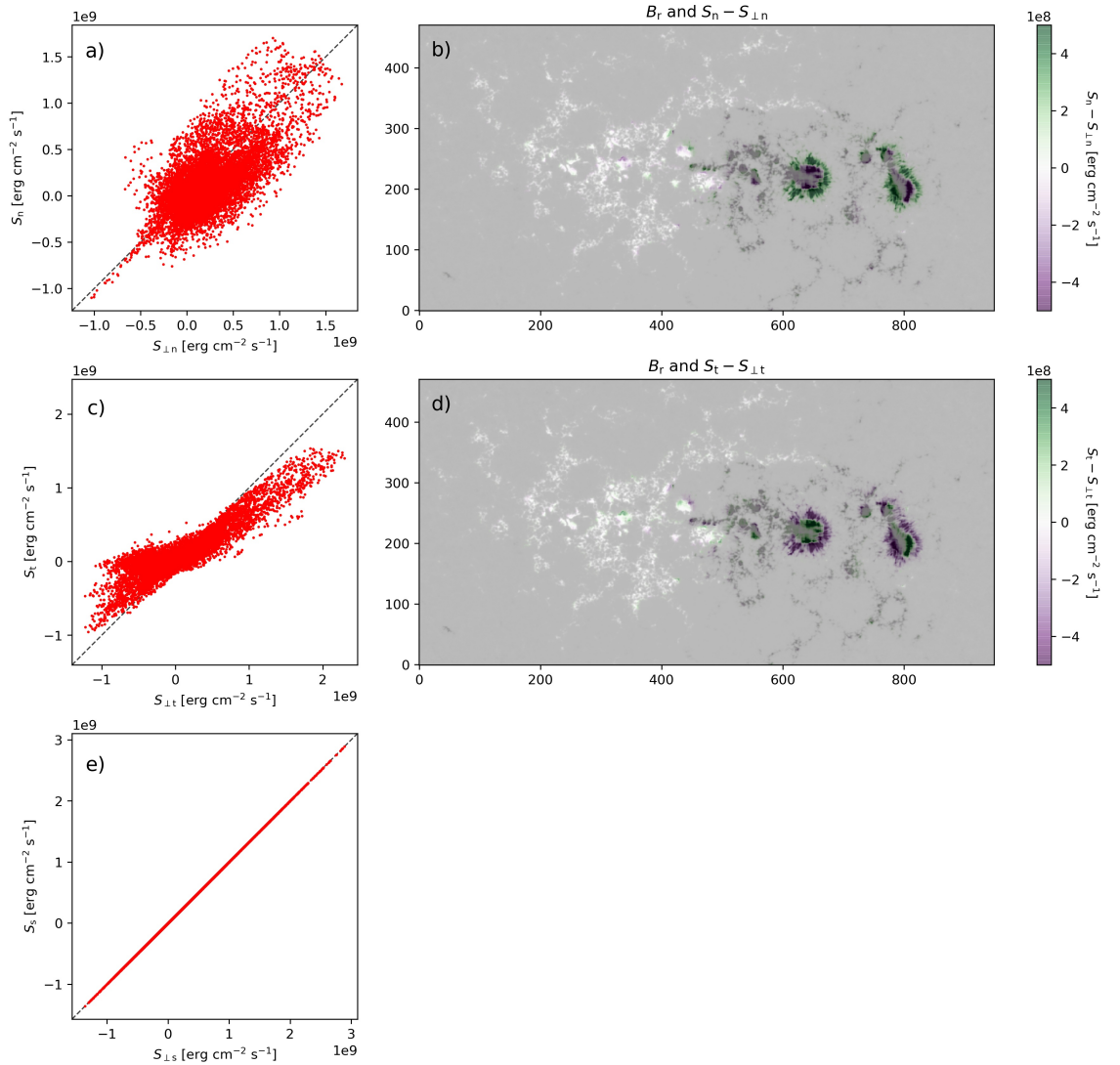


Figure 26: Left: Scatter plots between the Poynting flux calculated using the velocities obtained by DAVE4VM before and after using Equations 3.14 and 3.15 to remove the field-aligned components. Right: difference between the Poynting flux components before and after removing the field aligned velocity overlaid on an image of vertical magnetic field. To improve visualization the values in the colorbar were clipped at  $5 \times 10^8 \text{ erg cm}^{-2} \text{ s}^{-1}$  which represents less than the full extent of the differences as it can be seen in the scatter panels.

horizontal velocity overlays have distinct symmetry around the spots, which is a consequence of the field orientation in those regions. The trailing plage can also see differences in the velocities after the removal of the field-aligned components that are as large in magnitude as is observed around the leading spots. However, these pixels that contain a larger velocity difference in the trailing plage appear in a significantly smaller concentration of pixels than in the spots.

A similar comparison to the one presented in Figure 25 was also carried out to study the impact

that the field-aligned velocity removal has on the Poynting flux components. This led to Figure 26 that compares Poynting flux calculated before ( $S_n$ ,  $S_t$ ,  $S_s$ ) and after ( $S_{\perp n}$ ,  $S_{\perp t}$ ,  $S_s$ ) the field-aligned velocities were removed from the PyDAVE4VM output. The impact on the emergence (panel a) and shearing (panel c) terms of the Poynting flux show some resemblance with that observed for the changes in horizontal and vertical velocities (left column of Figure 25). For example, the differences in vertical velocities have a similar shape to what is observed for the emergence Poynting flux, while the horizontal velocities are more diagonally oriented similarly to what is observed in the shearing Poynting flux. Both Poynting flux components are observed in the scatter plots of Figure 26 panels a and c to suffer variations on the order of  $10^9 \text{ erg cm}^{-2} \text{ s}^{-1}$ , also illustrated in the image overlays of panels b and d. It is important to keep in mind that panels b and d of Figure 26 were tailored to unveil where the largest differences are and since the energy injection in plage is not typically on the order of  $10^8 \text{ erg cm}^{-2} \text{ s}^{-1}$  these images are not a good representation of the differences in such regions. However, panel e of Figure 26 shows that when the field-aligned velocities are removed the total Poynting flux remains unchanged for all pixels in the HARP image space, unlike what happens to each individual component. This behaviour can also be inferred from Figure 26 panels b and d since the differences shown are equal in magnitude and of opposite sign between the images. Therefore, if a study is concerned only with evaluating the total Poynting flux, removing the field-aligned velocities is an unnecessary step.

## 5.4 Distribution of Poynting flux per pixel

In Section 5.1, some of the works that studied the energy injection at the photospheric level were discussed so as to explore the values that different authors had found. This discussion was made chronologically and divided according to the instrumentation and data available at the time so that the evolution of the Poynting flux calculations could be noticed. The first step here is then to understand what are the typical Poynting flux values in the AR image space, how these values are distributed in ARs, and how they compare to what was previously reported in the literature.

The dataset of eight ARs in the sample set have a total of 10864 observations from which both emergence and shearing components of the Poynting flux are calculated. Each HARP number has on average a thousand observations associated to it that corresponds to about 8.5 days worth of data. The pixel values in these images were formed into histograms that show the value ranges for

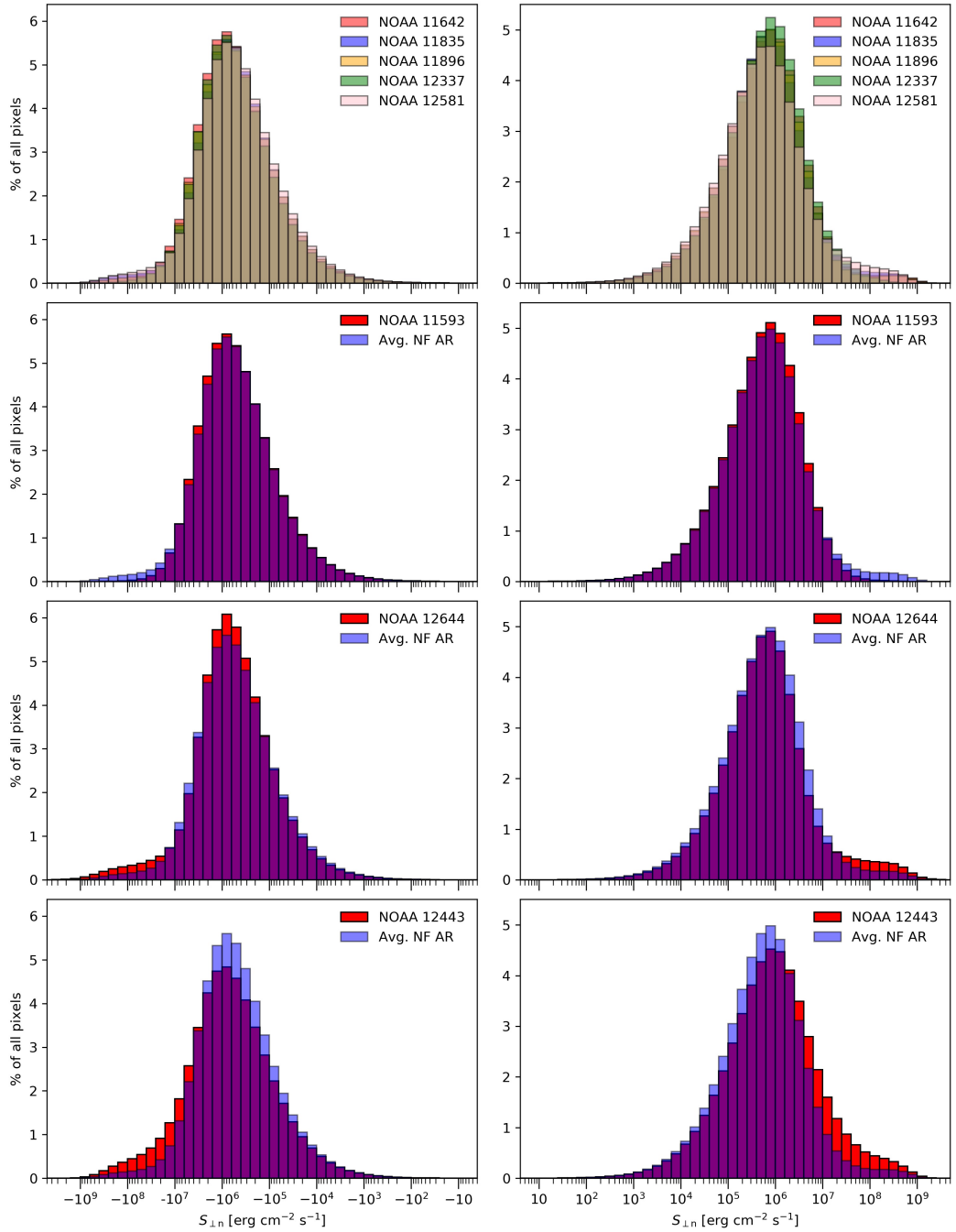


Figure 27: Frequency distributions of negative (left column) and positive (right column) values of Poynting flux emergence component,  $S_{\perp n}$ , over whole AR observation period. The top row displays all five non-flaring ARs, with the lower three rows showing the average of these distributions (in blue) for comparison with each of the flaring ARs (in red).

$S_{\perp n}$  (Figure 27),  $S_{\perp t}$  (Figure 28), and  $S_{\perp s}$  (Figure 29) over the whole lifetime of each AR.

The histograms of Figures 27-29 are divided into two columns containing only the positive values in the right-hand column and only negative values in the left-hand column. This separation

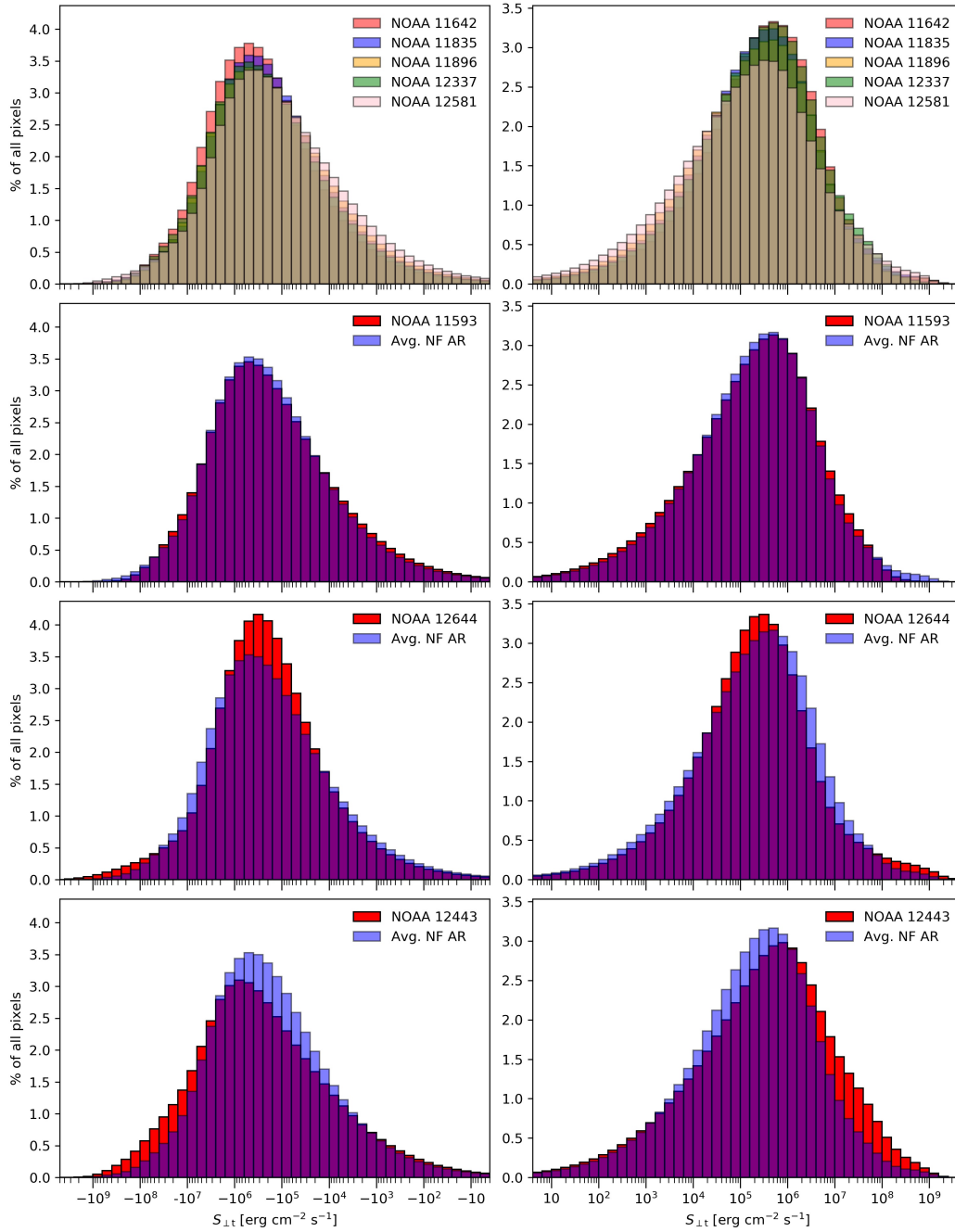


Figure 28: Same as Fig. 27, but for the Poynting flux shearing component,  $S_{\perp t}$ .

between the pixels responsible for injection and removal of energy creates a better overview of these values as a percentage of all the pixels in the dataset images. These Figures are also divided into rows where the top row contains the pixel value distributions for the non flaring regions. The average of the non flaring regions distributions is then used in the other three rows to draw comparisons with the three flaring regions as this facilitates the identification of any differences that may exist between the flaring and the non-flaring regions.

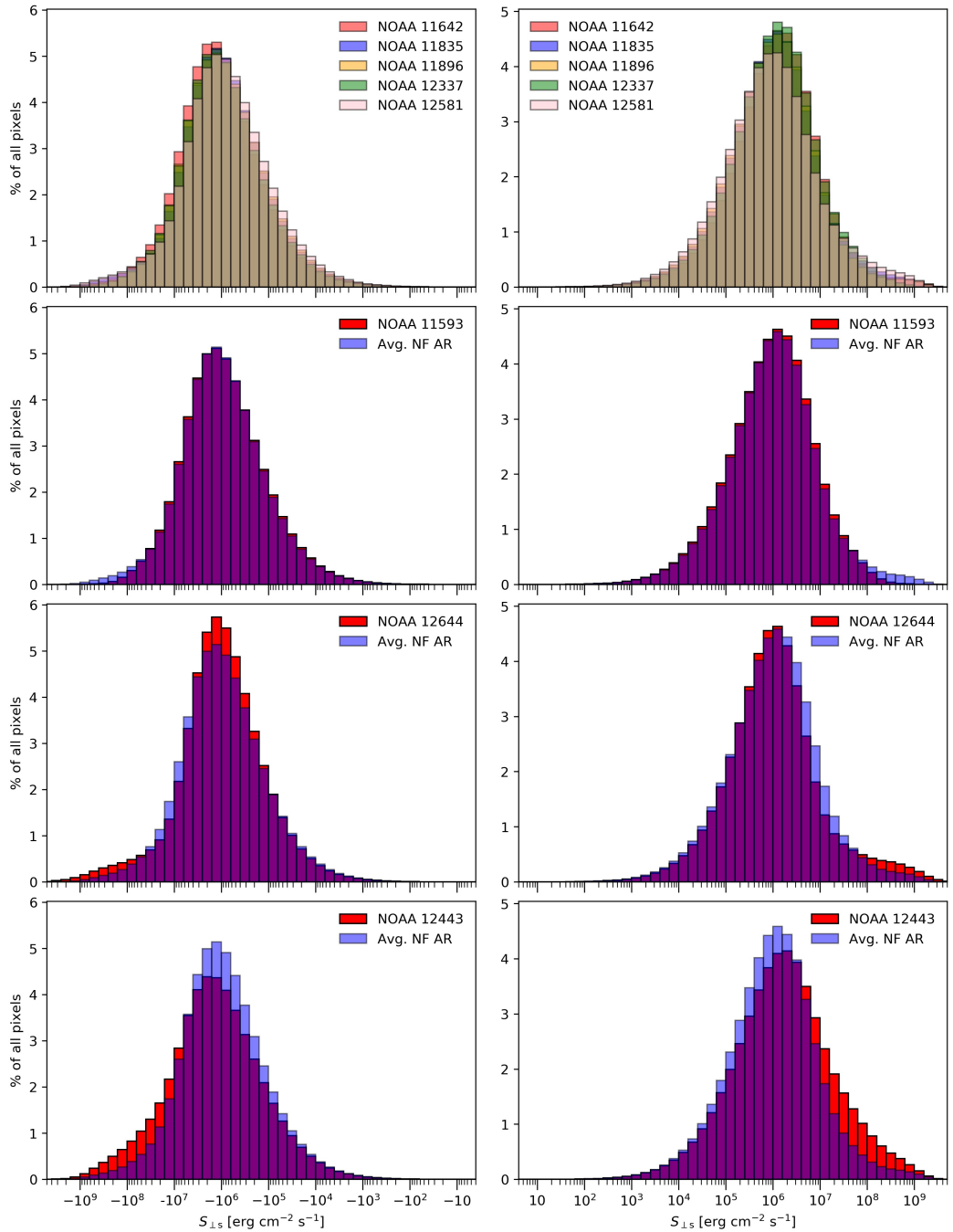


Figure 29: Same as Figs. 27 and 28, but for the total Poynting flux,  $S_{\perp s}$ .

The first and most straightforward information that can be obtained from the histograms are the value range for  $S_{\perp n}$ ,  $S_{\perp t}$  and  $S_{\perp s}$ . The values can vary over many orders of magnitude from as little as  $\pm 10^3$   $\text{erg cm}^{-2} \text{s}^{-1}$  to  $\pm 10^9$   $\text{erg cm}^{-2} \text{s}^{-1}$  but they all show a distinct peak close to  $\pm 10^6$   $\text{erg cm}^{-2} \text{s}^{-1}$ . It is important to keep in mind that in the HARP image space many pixels correspond to plage or quiet Sun regions, as illustrated in Figure 30.

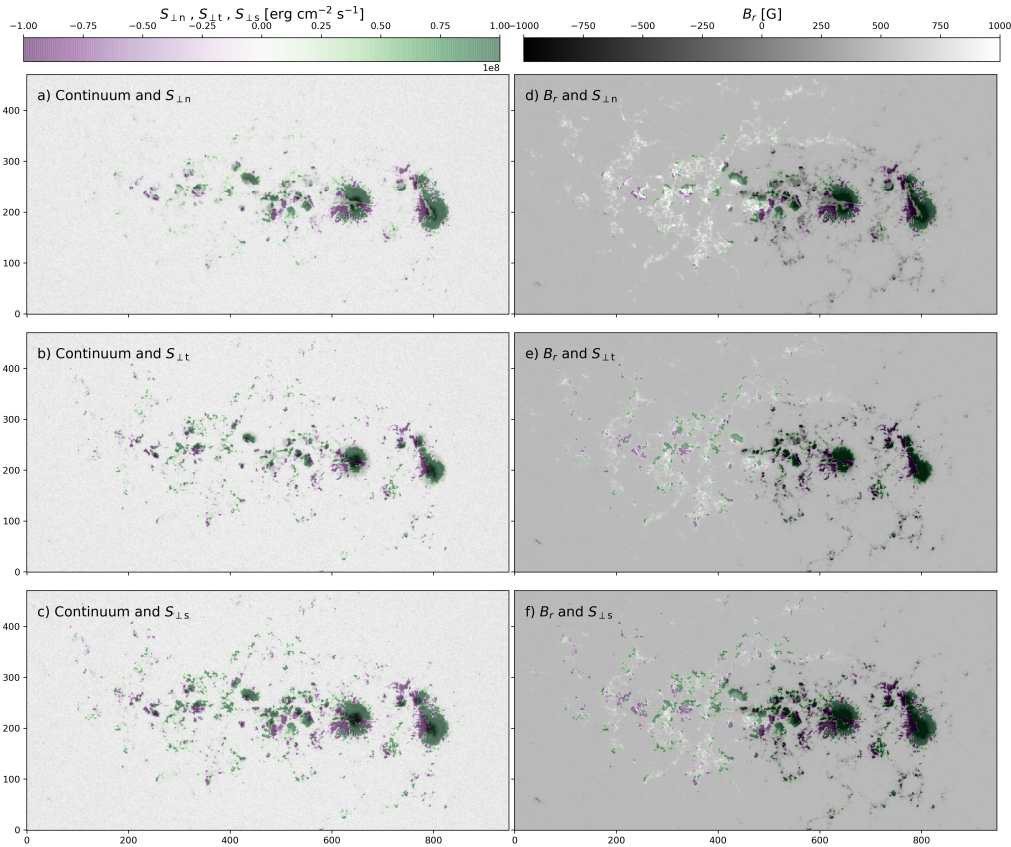


Figure 30: Overlays of  $S_{\perp n}$  (top),  $S_{\perp t}$  (middle), and  $S_{\perp s}$  (bottom) on continuum intensity (left) and radial magnetic field (right) images of NOAA 12443 at 2015-11-04 12:10 UTC. Values of Poynting flux and magnetic field are clipped at  $\pm 10^8 \text{ erg cm}^{-2} \text{ s}^{-1}$  and  $\pm 1000 \text{ G}$ , respectively, to improve the visualisation.

By comparing the results obtained for each flaring region with the non-flaring, it can be observed that for the two regions which produced M-class flares (NOAA regions 12644 and 12443) there is a greater abundance of pixels that are located in the extreme tails of the distributions for the normal ( $S_{\perp n}$ ), tangential ( $S_{\perp t}$ ) and total ( $S_{\perp s}$ ) Poynting flux. This implies that those regions not only saw greater amounts of energy being injected into them but that they also displayed greater amounts of energy removal. That is quite a contrasting result when compared to the weakly flaring region NOAA 11593 whose Poynting flux value distribution is remarkably similar to the non-flaring regions, containing only a minor proportion of extreme values in the distribution tails when compared to the average non-flaring histogram.

As discussed in Chapter 2, the HARP image space is defined by a rectangular box that is able to encompass the entirety of the AR that is being observed over its lifetime. Therefore in the image space the pixels contain not only measurements of the AR itself but also measurements

over the plage and quiet Sun. An example of how the Poynting flux distributes itself over the HARP image space and the magnetic structures therein can be seen in Figure 30 as an overlay of the Poynting flux over the continuum (left column) and vertical magnetic field (right column) for NOAA 12443 at 2015-11-04 12:10. From top to bottom, the rows show the overlays of  $S_{\perp n}$ ,  $S_{\perp t}$  and  $S_{\perp s}$ , respectively, using a green (positive) and purple (negative) colour scale.

Figure 30 suggests that values for energy injection/removal which surpass  $\pm 5 \times 10^7 \text{ erg cm}^{-2} \text{ s}^{-1}$  are found in a minority of the pixels that compose the image space and are usually located close to the spots and in some pixels that compose the plage. This example also portrays that not only regions with strong magnetic field (such as spots) have a strong Poynting flux associated to them. The preference in location for spots or plage is expected for the most intense Poynting flux when taking Equations 3.16 and 3.17 into consideration. Since the Poynting flux depends on both plasma velocity and magnetic field, regions with modest magnetic field are capable of having a substantial injection/removal of energy associated to them if they have a significant plasma velocity,  $v_{\perp}$ . The opposite also holds and can be noticed clearly in Figure 30 as some parts of the spot regions show weak Poynting flux values. The histograms (Figures 27, 28 and 29) show that those pixels which represent energy fluxes contributing more than  $\pm 5 \times 10^7 \text{ erg cm}^{-2} \text{ s}^{-1}$  account for less than 5% of the total number of pixels in the dataset.

## 5.5 Evolution of FOV-integrated energy

Time series that describe the energy evolution of each AR in the sample set were created by summing the pixel-integrated Poynting flux values over all image space at each point in time covering the ARs evolution. The results were also averaged after this spatial integration using a centered 24-hour rolling window in order to smooth out any oscillations that are introduced by the HMI orbital period (Hoeksema et al., 2014). The rolling window used to average the ARs causes 12 hours of data loss at each end of the time series, corresponding to approximately  $6^{\circ} - 8^{\circ}$  of heliographic longitude coverage.

Using this time series information, Figure 31 was created to compare the evolution of the three flaring regions NOAA 11593, 12644 and 12443, with each region in the non-flaring set. The evolution of the flaring regions is represented by the solid red lines in every panel while the non-

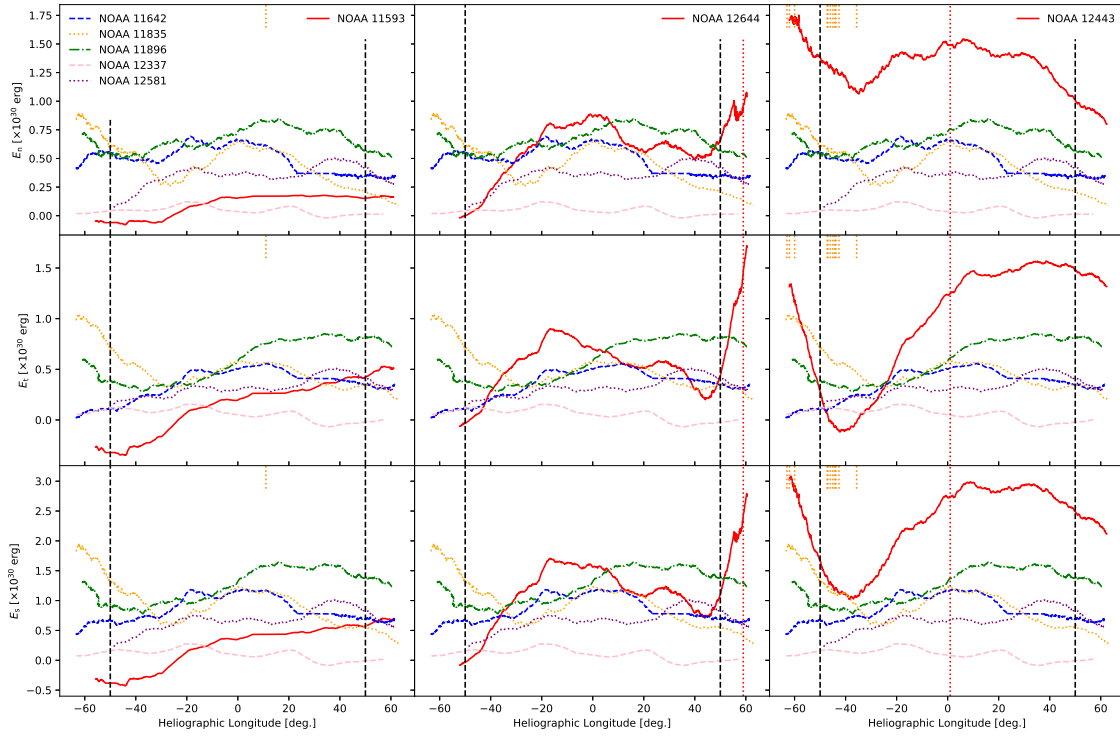


Figure 31: Time series of the energy evolution the three flaring regions compared with the non flaring regions of the control set. Each time step assume that the power obtained by calculating the Poynting flux stayed constant over the 720 seconds window. Row wise, from top to bottom we have the plots for the contributions given by the emergence, shearing and total Poynting flux. Column wise from left to right we have NOAA 11593, 12644 and 12443. The red dashed line mark the latitudes where NOAA 12644 and 12443 produced a M class flare. The gray dashed lines mark the latitudes where problems with disambiguation are diminished in our dataset.

flaring regions are represented by dashed lines in different colours. Figure 31 is divided into three columns where each column compares the energy evolution of one of the flaring regions with every region in the non-flaring set. From left to right the columns display the flaring ARs according to their activity, with the left-most column being NOAA 11593 (that produced only C-class flares), the center column being NOAA 12644 (that produced 19 flares including an M class flare), and the right-most column being NOAA 12443 (that produced over 40 flares including an M-class flare). Figure 31 is also organized in rows showing from top to bottom the emergence ( $E_n$ ), shearing ( $E_t$ ) and total ( $E_s$ ) pixel integrated Poynting flux as a function of the HARP centroid longitude. Each pair of SHARPs observations is separated by 720 seconds and the time series have an implied assumption that the Poynting flux remained constant during this interval so that each point in the time series represents how much energy was injected/removed in this time interval (Figure 31). There are also vertical dashed gray lines highlighting the  $\pm 50$  degrees of longitude

mark which is where upon visual inspection of the whole dataset it was decided that most images are free from disambiguation effects to produce the most accurate results using PyDAVE4VM. The vertical dashed orange lines located in the top of each panel represent the longitude which the flaring ARs were located when they produced a flare over C5.0 on the GOES scale. Finally, the vertical dashed red lines represent the M-class flares produced by NOAA 12644 (middle column) and NOAA 12443 (right column).

When looking at the energy injection/removal for the ARs represented in Figure 31, it can be noticed that the contributions towards the accumulation of energy are quite balanced between the emergence and shearing components. However, most of the energy removal is performed via the shearing component because  $S_{\perp n}$  is mostly (if not all the time) net positive. The time series show that the net Poynting flux is mostly injecting energy rather than removing it, which is not information that can be readily extracted from the histograms of Figures 27-29 as the pixel values seem at first glance to be symmetrically distributed between positive and negative values. This offers a strong hint that the energy dynamics are dictated by a small percentage of the pixels in the HARP image space causing the slightest differences in the tails of their value distributions to be enough to keep the energy difference positive over most of the lifetime of a region.

The accumulation of energy is illustrated in Figure 32 following the same layout as Figure 31. Figure 32 shows that the difference between the emergence and shearing contributions to the Poynting flux are generally small and vary on a case-by-case basis. Comparing the total energy accumulated by the ARs over their lifetime (bottom row of Figure 32) shows remarkably small differences in the amount of energy accumulated considering that the 8 ARs varied considerably in size, complexity and activity there is not much over one order of magnitude. There are two exceptions to this which are NOAA 11593 (flaring AR, red solid curves in left column) and NOAA 12337 (non-flaring AR, pink dashed curve in all panels) which have a much smaller spot area size than any other ARs in the dataset (see Table 5). It is also noteworthy that although the tangential Poynting flux ( $E_t$ ) presented a negative value for some observations, in none of the cases its cumulative values ended up being net negative. The total Poynting flux ( $E_s$ ) was then observed to be positive at all times for all ARs with the exception of NOAA 11593 that had energy removed from it for most of its transit over the solar disk but, even in this case, the total energy ended up net positive. Also, NOAA 11593 ended up accumulating significantly less energy than most regions (Figure 32) and was not

CHAPTER 5. CASE STUDY OF THE POYNTING FLUX OF 3 FLARING AND 5 NON-FLARING ARS

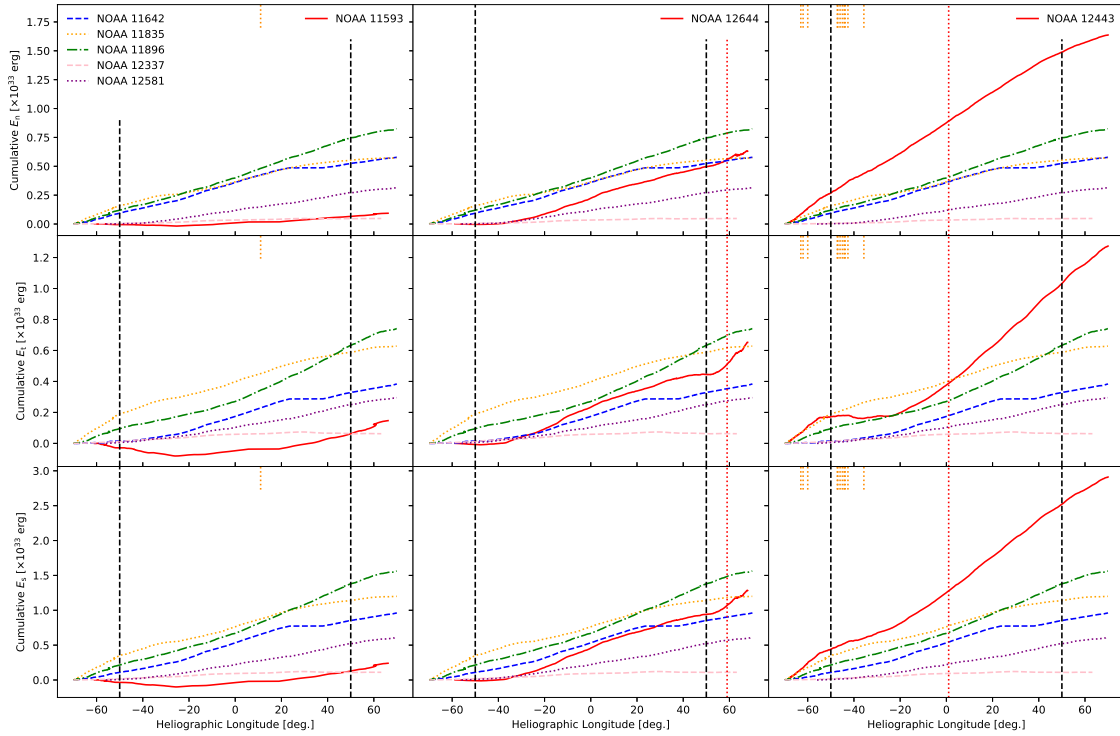


Figure 32: Time series of the cumulative energy for the three flaring regions compared with the non flaring regions of the control set. Row wise, from top to bottom we have the plots for the contributions given by the normal, tangential and total Poynting flux. Column wise from left to right we have NOAA 11593, 12644 and 12443. The red dashed line mark the latitudes where NOAA 12644 and 12443 produced a M class flare. The gray dashed lines mark the latitudes where problems with disambiguation are diminished in our dataset.

Table 6: Summary of the ARs featured in this work showing NOAA number designation, number of GOES flares produced by the AR, lifetime-average spot area expressed in millionths of the solar hemisphere, and daily Mt. Wilson class.

AR Flaring Status	NOAA Region Number	Accumulated Energy [erg]			Component Share of Total Energy [%]	
		Emergence	Shearing	Total	Emergence	Shearing
Flaring	11593	$9.32 \times 10^{31}$	$1.47 \times 10^{32}$	$2.40 \times 10^{32}$	38.8	61.2
.....	12644	$6.31 \times 10^{32}$	$6.52 \times 10^{32}$	$1.28 \times 10^{33}$	49.2	50.8
.....	12443	$1.64 \times 10^{33}$	$1.27 \times 10^{33}$	$2.91 \times 10^{33}$	56.2	43.8
.....	Average	$7.87 \times 10^{32}$	$6.78 \times 10^{32}$	$1.48 \times 10^{33}$	53.7	46.3
Non-flaring	11642	$5.78 \times 10^{32}$	$3.84 \times 10^{32}$	$9.62 \times 10^{32}$	60.1	39.9
.....	11835	$5.72 \times 10^{32}$	$6.28 \times 10^{32}$	$6.00 \times 10^{32}$	47.7	52.3
.....	11896	$8.22 \times 10^{32}$	$7.41 \times 10^{32}$	$7.82 \times 10^{32}$	52.6	47.4
.....	12337	$4.79 \times 10^{31}$	$6.26 \times 10^{31}$	$5.52 \times 10^{31}$	43.4	56.6
.....	12581	$3.15 \times 10^{32}$	$2.95 \times 10^{32}$	$3.05 \times 10^{32}$	51.6	48.4
.....	Average	$4.67 \times 10^{32}$	$4.22 \times 10^{32}$	$8.89 \times 10^{32}$	52.5	47.5
All ARs...	Average	$6.27 \times 10^{32}$	$5.50 \times 10^{32}$	$1.18 \times 10^{33}$	53.3	46.7

observed to have an energy injection that stood out from the control set (Figure 31).

Table 6 provides a complete overview of the share of the total energy that was accumulated through the emergence and shearing components of the Poynting flux. Each AR has a particular split in the percentage of total energy that was accumulated through emergence or shearing but, averaging the percentage contributions over the entire set, there is no apparent preference in energy injection as the difference between the components is considerable smaller than 1%. The largest imbalances are observed for the the least flaring region NOAA 11593 where there is a clear predominance on the energy injected due to shearing (~61%) and the non-flaring region NOAA 11642 where most of the energy was injected by emergence (~60%). The other regions had a more balanced distribution in their energy injection between the two Poynting flux components.

## 5.6 A closer look at NOAA 12644

Looking closely at NOAA 12644 can be quite insightful as its data series covers the hours before it first emerges (and later receives a NOAA designation) until hours after it produces an M-class flare. Also, the region was located close to 60° longitude when the M-class flare took place which, as discussed before, is a place where uncertainties related to problems in the magnetic field vector disambiguation become more relevant and impact the velocity flow-field calculations.

Looking at the histograms in Figures 27-29, the Poynting flux pixel values of NOAA 12644 show a clear surplus in the outermost wings of the distribution when compared to the non-flaring set, but this surplus is small when compared to what was observed for NOAA 12443. Although both regions produced M-class flares, there are significant differences in the total number of flares recorded for each region and NOAA 12443 is almost twice as large in area than NOAA 12644 (Table 5). Also the M3.7 flare produced by NOAA 12443 was possibly accompanied by a CME that would require in total approx. 2 or more times the energy (Emslie et al., 2005), unlike the confined M2.3 flare produced by NOAA 12644. Therefore, although these ARs share the fact that they produced an M-class flare during their lifetimes they are very distinct from each other.

The values for energy injection by the emergence Poynting flux ( $E_n$ ) in NOAA 12644 (represented in the centre column of the time series plots in Figure 31) are observed to quickly rise and overtake the  $E_n$  values displayed by the regions in the non-flaring set. Since NOAA 12644 is an emergent region, this was likely due to the emergence of the bipole. The spots in the region are also observed

to drift apart as it emerged due to strong horizontal flows that led to a rapid rise in the energy injection by the shearing Poynting flux ( $E_n$ ). After this initial surge, NOAA 12644 becomes less distinct to the regions in the non-flaring set except for some hours before the M-class flare where a remarkable upturn is observed in both  $E_n$  and  $E_t$ . Figure 32 shows that NOAA 12644 accumulated only as much energy as the regions in the non-flaring set during their passage, despite the moments where it was quickly increasing its energy injection.

Under the assumption that most of the energy injection was observed for NOAA 12644, Figure 32 suggests that it is not uncommon for an AR to see the levels of energy injection of a flaring region such as NOAA 12644. However, the energy build-up shown in Figure 32 does not take into account what portion of the accumulated energy was available to trigger an energetic event. To investigate the free energy build-up it is necessary to use different methods, like magnetic field extrapolations, but these can easily turn into a computationally demanding process when applied over a larger dataset.

The energy injection pattern of NOAA 12644 that can be observed in Figure 32 also seem to be related to the evolution of its Mt. Wilson classification displayed in Table 5. As an emergent region, it took some days for it to receive a NOAA designation which is why its morphology time series starts a few days later than what is observed by the other regions in this study. The first NOAA designation of 12644 was given when the region is observed to reach its first peak in energy injection which is when the region was located around  $-20^\circ$  heliographic longitude. NOAA 12644 was mostly classified as a  $\beta$  region in the days to follow while its energy injection in both components was decreasing. The AR then evolve to a  $\beta\gamma$  classification as it approached the energy surge that preceded the flare. Finally, after the flare, NOAA 12644 received a  $\beta\gamma\delta$  classification which suggests that it kept getting more complex. However, when this classification was issued the region was very close to the solar limb which undermines the accuracy of this final  $\delta$  classification.

A good degree of comparison with NOAA 12644 can be found in the two emerging regions of different flaring activity studied by Liu and Schuck (2012): NOAA 11072 (that did not produced a C-class flare or above) and NOAA 11158 (that produced several major flares). Liu and Schuck (2012) found an energy injection of  $10^{27}$  erg  $s^{-1}$  for NOAA 11158 that was almost one order of magnitude higher in both Poynting flux components than what was found for NOAA 11072. The

energy injection observed in Figure 31 for NOAA 12644 is quite similar in numbers for  $E_n$  and  $E_s$  to what is reported in Liu and Schuck (2012). However, some of the regions in the non-flaring set (NOAA 11642, 11835, and 11896) also show a similar level of energy injection, reinforcing the idea that the differences in point-in-time Poynting flux injection for flaring and non-flaring regions are not obvious.

## 5.7 Discussion

Different behaviours are observed in the horizontal and vertical velocities that are calculated using DAVE4VM when the field-aligned components are removed from them. Horizontal velocities see differences concentrated on the surroundings of the spots (showing values above  $0.5 \text{ km s}^{-1}$ ), while the differences in vertical velocities are less pronounced (showing values above  $0.2 \text{ km s}^{-1}$ ) but are more scattered over the whole HARP image space. The removal of field-aligned velocities also proved to affect the calculations on the trailing plage, as some of the pixels associated with these structures displayed differences as large as those found around the spots.

The differences found in the Poynting flux before and after removing the field-aligned velocities using Equations 3.14 and 3.15 can reach  $10^9 \text{ erg cm}^{-2} \text{ s}^{-1}$  in order of magnitude as portrait in the panels a and b of Figure 26. Values in this order of magnitude are found among the largest Poynting flux values for every region in the tails of their value distributions as shown in the histograms of Figures 27-29. However, the changes that take place when removing field-aligned components (i.e.,  $S_n \rightarrow S_{\perp n}$  and  $S_t \rightarrow S_{\perp t}$ ) in both Poynting flux components do not affect the calculation of the total Poynting flux (i.e.,  $S_s = S_{\perp s}$ ) making it unnecessary to remove the field align components if the objective is to calculate the only total Poynting flux.

It is interesting to note that the value at which the distributions of  $S_{\perp n}$ ,  $S_{\perp t}$  and  $S_{\perp s}$  peak are very comparable to the values obtained for the plage regions of NOAA 10930 presented by Yeates et al. (2014), while the value found by Welsch (2015) lies comfortably within the upper half of the distribution. This offers a strong indication that the results obtained here are also consistent with and able to account for the Poynting flux input within plage regions. The largest Poynting flux values, located in the outermost wings of the histograms, are more comparable to the Poynting flux values observed by Kazachenko et al. (2015) in NOAA 11158 that produced an X-class flare.

The peak values in the histograms are also in good agreement with previous estimates, e.g., the proxy Poynting flux values of  $\pm 10^{6.7} \sim 10^{7.6}$  erg cm<sup>-2</sup> s<sup>-1</sup> obtained by Tan et al. (2007) and the early estimations for the energy atop granules of  $5 \times 10^6$  erg cm<sup>-2</sup> s<sup>-1</sup> by Piddington (1956). Also, both pixel and integrated over the field of view Poynting flux values presented in this section are more than enough to account for the estimated coronal and chromospheric heating as well as energetic events that often happen in the solar atmosphere since every 12 minutes there is close to  $10^{30}$  erg being injected in the HARP FOV. However, it is important to remember that not all the energy injected is prone to or available to be used in energetic events and extrapolating the coronal field could offer the appropriate insight in this direction.

Comparing the energy dynamics of each flaring AR in Figure 31 (solid red lines) with the non-flaring set (dashed coloured lines), the two M-class-producing ARs (NOAA 12644 and 12443 in the middle and right columns, respectively) clearly stand out from what is observed in the non-flaring set. The energy dynamics of NOAA 12644, which is an emergent region, shows two periods of intense surges in the values of both the emergence and shearing Poynting flux components that is unlike what is observed in the non-flaring set. NOAA 12443 can be easily spotted from the non-flaring set as for most of its lifetime its Poynting flux values are considerably larger than what is observed in the non-flaring set however, both NOAA 12644 and 12443 are significantly larger in size and also displayed more complex magnetic field configurations over their lifetimes than any other region featured in this study. In comparison, the smallest flaring region (NOAA 11593) had a weaker energy injection than most of the non flaring regions despite the fact it produced C-class flares. The only region in the non-flaring set that had Poynting flux values that are comparable to NOAA 11593 is NOAA 12337 which is the smallest region in the entire dataset.

Comparing the energy injection of NOAA 12644 and 12443 before they produced their single M-class flares (marked by the vertical dashed red lines in Figure 31) it can be seen that the two regions were experiencing rather different trends in the rate at which the Poynting flux was evolving. NOAA 12644 saw a sharp gradient in both its normal and tangential Poynting flux components covering about one and a half days that lasted until the flare took place. Some extra care must be taken when considering these spikes in energy injection as this part of the data was calculated after the centroid of the HARP box passed the mark of 50 degrees of heliographic longitude. However, the sustained progression over many days indicates that this is not due to vector disambiguation

issues that “flick” between different solutions. NOAA 12443 was also experiencing a growth in its total energy injection before its M-class flare, driven by an increase in its tangential Poynting flux that was observed for over 4 days before the flare. The rate at which the energy injection was increasing in NOAA 12443 is however visibly smaller than what was observed in NOAA 12644. Unfortunately, there is no data covering the post flare phase of NOAA 12644 as the region was already approaching the west limb, making it impossible to compare the behaviour of these regions after their M-class flares took place. The number of ARs that has been studied to date is far too small to make it possible to spot a general trend that may exist in their energy injection. This points to a clear necessity of conducting a similar analysis over a larger sample.

The energy evolution of the smallest flaring AR (NOAA 11593) is also, in its own way, remarkable. NOAA 11593 was the second smallest AR in the sample dataset and its energy injection profile is only comparable to the smallest region in the non-flaring set (NOAA 12337). Nevertheless, this region produced 10 C-class flares with one of those being over C5. As this region was not observed in its entirety since emergence it was not possible to follow the entire buildup to its strongest flare that happened when it was close to the disk center. However, NOAA 11593 was not observed to have an energy injection that stood out from the non-flaring set (Figure 31).

Focusing on the total energy accumulated by the ARs over their lifetime (shown in the bottom row of Figure 32) shows remarkably small differences in the amount of energy accumulated considering that the 8 ARs varied considerably in size and complexity. There are two exceptions to this which are NOAA 11593 (flaring AR, red solid curves in left column) and NOAA 12337 (non-flaring AR, pink dashed curve in all panels) which have a much smaller spot area size than any other ARs in the dataset (see Table 5)). It is also noteworthy that although the tangential Poynting flux ( $E_t$ ) presented a negative value for some observations, in none of the cases its cumulative values ended up being net negative. The total Poynting flux ( $E_s$ ) was then observed to be positive at all times for all ARs with the exception of NOAA 11593 that had energy removed from it for most of its transit over the solar disk but, even in this case, the total energy ended up net positive.

The evolution of the ARs studied by Welsch et al. (2011) (NOAA regions 10987, 10988 and 10989) can be used to draw some comparisons with the results displayed here in Figure 32. In Welsch et al. (2011) the regions studied also have different levels of activity but their energy evolution is described using the proxy Poynting flux which is a unsigned quantity. From the three

regions displayed, NOAA 10989 produced two C-class and one M-class flares while the flaring activity displayed by both NOAA regions 10987 and 10988 were limited to flares classed as A or B. Welsch et al. (2011) found that these regions accumulated energy amounting to  $\sim(0.5 - 2.5) \times 10^{33}$  erg, which is in good agreement with the values obtained for most ARs in this study (Figure 32) with the exception of NOAA 11593 and 12337. Welsch et al. (2011) stated that there was an expectation for the energy produced and accumulated by these regions would be somehow proportional to the level of activity displayed by them. However, contrary to their initial expectations, NOAA 10989 (that produced C-and M-class flares) accumulated less energy than the other ARs with its values almost two times smaller than the values obtained for the non-flaring NOAA 10988. Figure 32 here shows a clearer difference in the total energy accumulated ( $E_s$ , featuring in the bottom row) between the most active and complex region NOAA 12443 and the other regions. NOAA 12443 ended up accumulating almost twice as much energy as the other region that produced an M-class flare (NOAA 12644). However, it is important to remember that NOAA 12644 was still emerging when its observations started to be recorded, showing a steep gradient in its emergence phase that allowed it to quickly catch up with the non-flaring set. The energy evolution curves of NOAA 12644 in Figure 32 hint that it probably surpassed the non-flaring set regions in the amount of energy accumulated at some point, but this cannot be confirmed by the HARP observations due to its proximity to the West limb.

The four moderately large flares studied by Bi et al. (2018), being 3 M-class and a C9.3, also have no clear pre-flare signature. The energy flux reported for these 4 ARs ranged from  $10^{27}$  erg  $s^{-1}$  to  $\sim 2.5 \times 10^{28}$  erg  $s^{-1}$  but were not integrated over the time between consecutive images. These ARs did show a consistent behaviour of having their Poynting flux dropping to negative values during the flare time and quickly returning to positive values before the impulsive phase finished.

The values of Poynting flux and energy accumulation displayed in Figures 31 and 32, respectively, are in good agreement with the results of Liu and Schuck (2012), Tziotziou et al. (2013), Liu et al. (2014) and Su et al. (2018) where the contributions given by the two Poynting flux components ( $S_{\perp n}$  and  $S_{\perp t}$ ) are comparable with the emergence component being slightly larger than the shearing. This is quite distinct from what is reported in Romano et al. (2015) where the total Poynting flux was mostly driven by the shearing term. This is not quite a surprise given that the region studied by Romano et al. (2015) consisted of an opposite-polarity spot close to the main leading spot

that displayed high proper motion within the AR and a large degree of rotation during its movement (See also: Ruan et al., 2014) which would then lead to an injection of significant amounts of shearing Poynting flux. The four flaring regions studied by Bi et al. (2018) also see a majority of their Poynting flux being driven by the shearing component, although the difference in energy injection caused by the different components is not as pronounced as in Romano et al. (2015). The majority of the ARs saw a similar amount of energy being injected by the two Poynting flux components, the emergence Poynting flux seems to consistently inject more energy than its shearing counterpart although this difference is small. However, the amount of ARs that have been studied is not enough to make a definitive statement.

There are no obvious differences in the energy injection across all components ( $S_{\perp n}$ ,  $S_{\perp t}$  and  $S_{\perp s}$ ) observed for the flaring and non-flaring regions, with the exception of NOAA 12443 that is considerably larger in area and showed a more complex magnetic classification than the regions in the non-flaring set. Then, it is likely that this difference spotted in its Poynting flux is more linked to the AR size and magnetic field complexity themselves than the flaring activity. All the regions featured in this study accumulated between  $\sim 10^{31} - 10^{33}$  erg which is more than enough energy to fuel even a major solar event. However, the methods used to calculate the energy injection here are not able to estimate which share of this energy injection is free to be released in energetic events.

### Questions raised

Using the whole dataset to verify if there is a statistical preference in energy injection via emergence or shearing should bring a more realistic picture. For this small sample, and comparing with some known cases in the literature, no preference can currently be found.

Since the Poynting flux evolution for the regions portrayed in this study showed indications of being linked to the ARs Mt. Wilson class, this will be explored in Chapter 6 over all the regions in the database to verify if the amount of energy of a region is somehow dependent on the region complexity. Chapter 7 will then explore the Poynting flux according to flaring activity.

When this study was conducted there was no expectation that a clear flare signature or remarkable difference between the flaring regions and non-flaring set would be found because authors such as Leka and Barnes (2003) already showed that no single parameter is likely to be responsible for a

solar flare. However, the surges in both components of the Poynting flux ( $S_{\perp n}$  and  $S_{\perp t}$ ) before the M-class flares are quite intriguing even though they happened over different timescales. Then, in Chapter 7, the evolution of the Poynting flux for the regions in the database that produced M- and X-class flares will be studied in greater detail and compared with each other.

## Chapter 6

# Differences in Poynting flux behaviour between Mt. Wilson classifications

In this Chapter results from the complete dataset are explored to answer some of the questions raised by the initial sample in Chapter 5. This explores more general aspects of the link between photospheric Poynting flux and AR Mt. Wilson class, while also connecting the manifestations of energy injection with evolutionary changes in the ARs. The first Section of this Chapter introduces the reader to the dataset used in this study and how it attempts to get a sample of ARs that is a good representation of the ARs which appeared in Solar Cycle 24. The second Section focuses on exploring the relationship between Poynting flux and Mt. Wilson class that is (as discussed in Chapter 1) a way to classify ARs according to their complexity of magnetic polarity mixing.

In Chapter 5 it was shown that removing the magnetic field-aligned velocities can dramatically impact the calculation of the emergence and shearing components of the Poynting flux, even though their sum is unaffected by this removal. All the Poynting flux results featured in this Chapter use the velocities obtained from PyDAVE4VM with the field-aligned components removed. Additionally, to avoid the uncertainty introduced by disambiguation problems as much as possible, any data where the centroid of the HARP box is located beyond  $\pm 50^\circ$  longitude were excluded.

Ordering the Mt. Wilson classifications in terms of field complexity is not a trivial task. In the discussion that takes place in the second section of this chapter it is considered that the classifications vary in complexity following the order  $\alpha$  (simplest),  $\beta$ ,  $\beta\gamma$ ,  $\beta\delta$  to  $\beta\gamma\delta$  (most complex).

By associating the magnetic complexity with the Poynting flux, graphical representations of the energy injection can be created to show any systematic variation that ARs of different Mt. Wilson classification may have. This is covered in the first few sections of this Chapter using two different temporal samplings. At first the Poynting flux over the whole lifetime of ARs is studied to search for long term trends in energy injection and determine if any of the Poynting flux components show a larger contribution for injection. Then, the daily energy accumulation is studied to match the Poynting flux and Mt. Wilson class temporal sampling enriching the AR lifetime results. Finally, a study of the characteristic Poynting flux that is associated to changes in the magnetic complexity will be presented, as the database enables tracking these changes and efficiently pair this information with the integrated Poynting flux. This process allows for a better comprehension of which processes are associated to the evolution of ARs as the Poynting flux components are associated with two different types of energy injection (emergence and shearing).

Before breaking down the statistics of overall injection across Mt. Wilson class the next Section start by introducing the dataset that is used to produce the results in this Chapter. Then, a study exploring the different contributions given by the emergence and shearing components of the Poynting flux across the whole dataset is presented. The following sections extend the analysis by profiling the Poynting flux values and accumulation in two different timescales of energy accumulation being those the full AR lifetime and 24 hours. This way, the relative contributions of emergence and shearing motions as well as the total energy injection can be more clearly seen and understood for the different Mt. Wilson classes.

## 6.1 Introducing the dataset

As explained in Chapter 4, the entire dataset consists of the products derived from 81 different HARP numbers from which each number `hmi.sharp_cea_720s` data series contain the magnetic field vector and metadata of over 122 NOAA designated ARs. The database combines the products derived from the HMI magnetic field vectors such as velocity and Poynting flux maps with the information in the SWPC SRS and *Events* reports for each AR in that is present in the HARP image space. The images stored in the database amount to 1074001 different files and the entirety of the data stored occupy close to 4 TB.

As discussed in Chapter 2, defining a box for the HARP trying to isolate each AR is quite challenging given how dynamic the solar surface is, which results in some HARPs containing more than one AR. This can lead to complications when trying to study properties of individual ARs as the presence of different ARs in the same HARP image space makes it necessary to isolate the contributions of each AR for each image. While not impossible, isolating each AR would not only be time consuming but most importantly could create images of inconsistent sizes for the same HARP number, this would make the images unsuitable for many feature tracking methods and could severely affect the integrated products that are derived from the images.

Therefore not all the data available from the HARPs registered in the results database was deemed suitable for producing the results featured in this Chapter. Only HARPs that contain one unique NOAA are used here in order to avoid inconsistencies in the Poynting flux calculations and subsequent analysis. There are 51 HARPs that satisfied this “uniqueness” condition in the entire dataset, which of course considerably reduces the number of HARPs used but it greatly improves the data consistency. Then, the dataset used here has almost 7 times more regions than the dataset used to produce the results in Chapter 5.

Although these results will have a certain statistical meaning offering a fair insight on the energy injection of ARs they are only consistent solar observations covering a small fraction of the Sun lifetime. Therefore, caution still needs to be taken when looking at these results in a broader perspective (i.e., Sun as a star) as the data used is gathered around an incredibly small temporal window in comparison to how old the Sun is. However, in comparison to the length of a solar cycle, these results have a significant coverage being them particularly meaningful for Solar Cycle 24 which is the cycle these ARs are sampled from.

In Chapter 4, Figure 22 showed the frequency distribution of the Mt. Wilson classifications issued for all NOAA ARs between 2012-2018 that guided the search for the ARs that would compose the final dataset. Similarly, Figures 33 and 34 show the frequency distribution of the Mt. Wilson classification for every region in the dataset that was used to produce the results in this Chapter, already excluding HARPs that contain more than one NOAA region. Looking at the most complex Mt. Wilson classification that was issued during the lifetime of each AR, Figure 33 shows the share of the dataset covered by each classification. The most frequent classification is  $\beta$  (~45%) followed by  $\alpha$  and  $\beta\gamma\delta$  (~20% each),  $\beta\gamma$  (~10%) and  $\beta\delta$  (<5%).

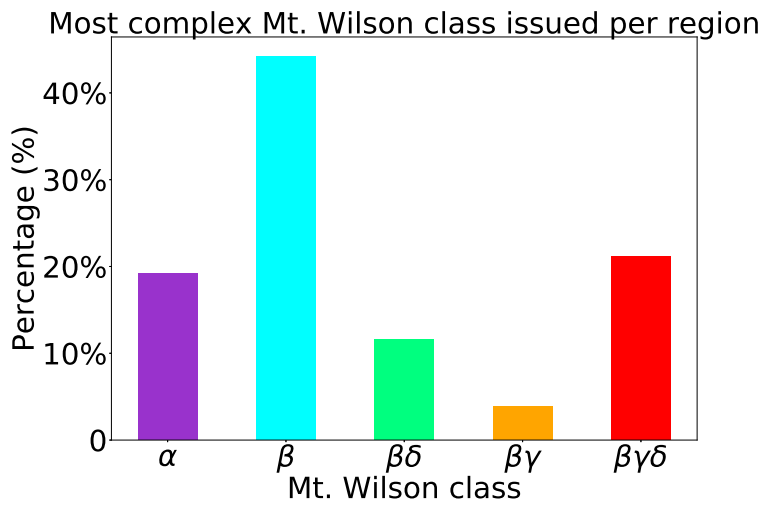


Figure 33: Frequency distribution of the most complex Mt. Wilson classification issued for each region in the dataset.

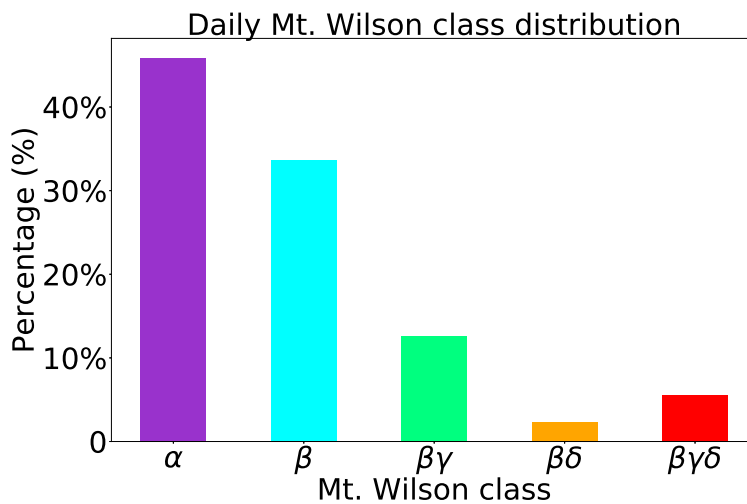


Figure 34: Frequency distribution of every daily Mt. Wilson classification issued for each region in the dataset.

Looking instead at the daily instances of each ARs Mt. Wilson class, Figure 34 illustrates that the share of the dataset covered by each classification is  $\alpha$  making up ~45%,  $\beta$  being ~35%,  $\beta\gamma$  having ~15%,  $\beta\delta$  comprising <5%, and  $\beta\gamma\delta$  covering ~ 5%. The share of entries on the database for each Mt. Wilson classification then drops with complexity with a small increase for  $\beta\gamma\delta$  regions. The differences observed in Figures 33 and 34 are just a reflection of the changes in magnetic field complexity that can be observed over an AR lifetime. When the selection of ARs that would compose the dataset took place the goal was to have a similar distribution as what was generally observed by HMI. Figure 22 contains the frequency of all the Mt. Wilson classes from

the beginning of the HMI era in 2012 to the beginning of the selection process in 2018. Figure 33 indicates that this goal was reasonably achieved and the dataset should provide a fairly accurate representation of ARs as they appeared in Solar Cycle 24. A complete table containing basic details of the ARs used in this Chapter can be found in Appendix A (Tables 10 and 11).

## 6.2 Overall energy share

It was found in Chapter 5 that for the 8 regions studied there the share of energy that was being injected by emergence and shearing was essentially the same (i.e., a roughly 50:50 split). However, two ARs displayed a difference of over 20% between the energy injected by the two components (i.e., splits of 60:40 and 40:60). Figure 35 shows a box-and-whisker plot of the percentage of the whole-lifetime energy accumulated by the emergence and shearing Poynting flux components over all ARs in the dataset.

Box-and-whisker plots are a method commonly employed to show how a dataset is distributed without assuming a distribution form. The coloured box is bounded on its lower edge by the first quartile (Q1) and on its upper edge by the third quartile (Q3), meaning that it defines the interquartile range (IQR) where the central half of the data points are located. The horizontal line in the middle of the box is the second quartile (Q2) that is the median of the distribution. The lines extending away from the IQR box are called whiskers, which (in this implementation) extend out to 1.5 times the IQR. These whiskers cover almost all of the remaining data values, but any that lie beyond the whiskers are known as outliers and are plot as individual data points.

The IQRs representing the share of the total energy accumulated via emergence ( $E_n$ ; blue box) and shearing ( $E_t$ ; orange box) show that there is a preference for the energy injection by emergence because its whole IQR is above the 50% line. The median value is slightly larger for  $E_n$  (55%) than  $E_t$  (45%). However, the shearing Poynting flux component also injects a substantial amount of energy mostly between 40 – 50% of the total and, in a few cases, even surpass the energy injected by its emergence counterpart.

The outlier representing the case where the energy injected by emergence represents close to 80% of the total was produced by NOAA 12340. Over its lifetime this region was no more complex than a  $\beta$  Mt. Wilson classification and did not produce any flares. The energy accumulated via

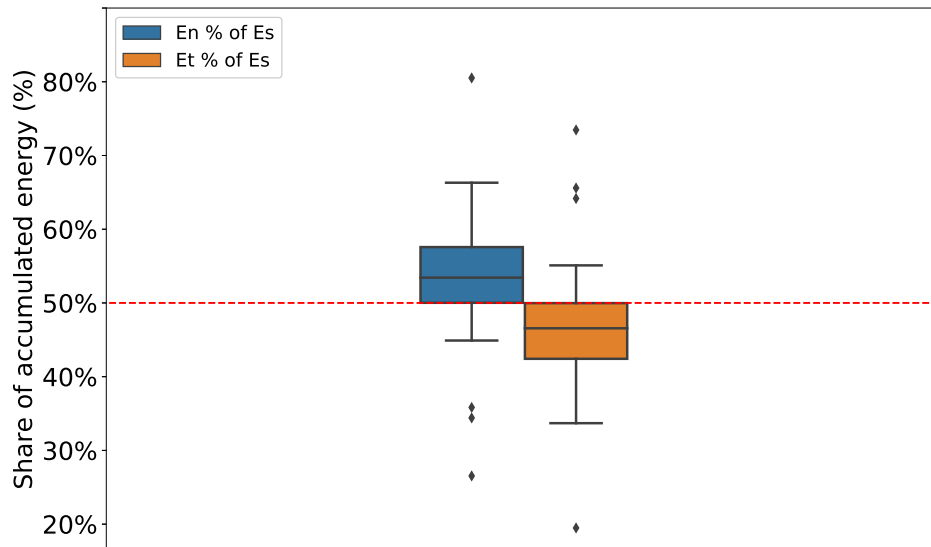


Figure 35: Box-and-whisker plot of the share of the lifetime-accumulated energy that was injected by emergence (blue box) or shearing (orange box). The red line marks the point where the contribution of the components are balanced (i.e., 50%).

emergence was  $1.3 \times 10^{31}$  erg which is almost one order of magnitude more than that injected by shearing ( $3.2 \times 10^{30}$  erg), resulting in a total injection of  $1.6 \times 10^{31}$  erg. Checking the magnetic field of the region in a movie sequence, it becomes clear why there is such imbalance as there is clearly more flux emergence taking place in the HARP image space than horizontal motions.

There are three other outliers where the share of energy injected through shearing represents more than 60% of the total energy injected. Those correspond to NOAA regions 11643 ( $\sim 73\%$  of  $2.5 \times 10^{31}$  erg), 12611 ( $\sim 65\%$  of  $3.5 \times 10^{31}$  erg), and 12196 ( $\sim 64\%$  of  $4.1 \times 10^{31}$  erg) that were issued maximum Mt. Wilson classification over their lifetimes of  $\beta$ ,  $\beta$  and  $\alpha$ , respectively. Although NOAA 11643 and 12611 produced flares, the flaring activity was rather modest as NOAA 11643 only produced a single B-class flare and NOAA 12611 produced 6 B-class and 1 C-class.

The share of energy introduced by emergence and shearing in Figure 35 shows that while emergence generally injects more energy it is not completely dominant in the ARs, consistent with what has been observed in case studies spread across the literature (e.g., Liu and Schuck, 2012; Liu et al., 2014; Su et al., 2018). Also, even in the case here with the smallest injection of energy through shearing, the amount of energy accumulated still corresponds to  $3.2 \times 10^{30}$  ergs.

### 6.3 Energy injection as a function of Mt. Wilson class

The Poynting flux values distribution and range will be explored according to the ARs Mt. Wilson class. This study is then divided into three different parts that make the use of box-and-whisker plots to study the distributions of energy injection that are linked to the Mt. Wilson classification of an AR. These consist of comparing:

- i) the energy accumulation to the most complex Mt. Wilson classification an AR presents over its lifetime;
- ii) the daily energy accumulation to the daily Mt. Wilson classification of ARs;
- iii) the daily energy accumulation to the 24-hour evolution in Mt. Wilson classification of ARs.

Comparing the Poynting flux with Mt. Wilson classification seems to be a quite straightforward task as, in principle, analysis such as that made in the last Section with box-and-whisker plots can offer a meaningful insight on the energy injection of ARs. However, Mt. Wilson classifications are issued on a daily basis following observed changes in the magnetic field of a region.

If one is interested in investigating the relationship of energy injection and the most complex morphology an AR exhibits over its lifetime (as explored in Section 6.3.1), the fact that the Mt. Wilson classification is issued daily does not represent a problem. On the other hand, breaking the analysis down to the daily Mt. Wilson classifications of an AR brings into question how to match the daily SRS classification with the 120 observations the HMI produces every day with 12 min sampling. This will be described in more detail in Section 6.3.2 for day-by-day cases, before Section 6.3.3 focuses on a similar analysis broken down into the specific evolutionary steps between Mt. Wilson classes over 24 hours.

#### 6.3.1 Analysis per most complex Mt. Wilson class issued over lifetime

In here the findings on how the energy behaves based on the most complex Mt. Wilson issued for every region are discussed. Grouping the dataset as proposed, the 51 different regions in have the following distribution: 9  $\alpha$ , 23  $\beta$ , 6  $\beta\gamma$ , 2  $\beta\delta$ , and 11  $\beta\gamma\delta$ . While there are a good number of  $\alpha$ ,  $\beta$ , and  $\beta\gamma\delta$  regions, the results featured here for  $\beta\gamma$  regions should be viewed with more caution as there are only 6 of this maximum classification in the dataset. The results for  $\beta\delta$  regions in this Section are shown for completeness as there are only 2 regions with  $\beta\delta$  as their most complex Mt.

Wilson classification. In Section 6.3.2, where the daily-accumulated Poynting flux is used, more entries will be available for every Mt. Wilson classification although the daily entries still come from the same 51 regions.

The integrated Poynting flux over the HARP FOV is already registered in the results database for every image. However, based on the discussions of Chapter 5, the integration over time series was limited to images whose HARP centroids were between  $\pm 50^\circ$  longitude to be sure of avoiding disambiguation effects. Then, the ARs were grouped based on the most complex Mt. Wilson classification that was issued in their lifetime. The top panel of Figure 36 shows box-and-whisker plots with the energy accumulated through emergence (blue box) and shearing (orange box), as well as their total (green box), across the different Mt. Wilson classifications. The bottom panel of Figure 36 contains a second set of box-and-whisker plots displaying the share of total energy that was accumulated through emergence (again in blue) and shearing (again in orange).

Comparing the energy accumulated over the whole lifetime of regions carry some biases as some regions have more days worth of observation than others. Emerging or decaying regions, for example, mostly have less days of observation and reach modest levels of magnetic complexity. Also, regions with more magnetic field complexity tend to have larger lifetimes than its less complex counterparts (see, e.g., Table 1 of van Driel-Gesztelyi and Green, 2015). This can then create a bias that will mostly affect  $\alpha$  and  $\beta$  ARs. That said, the top panel of Figure 36 shows a growing trend in the interquartile ranges covered by the amount of energy accumulated by Mt. Wilson class. The whiskers of the  $\beta$  regions are seen to approach the red line that marks no energy change over the lifetime of the regions, although the smallest value for energy injection in the dataset is on the order of  $10^{31}$  erg. On this scale of a few days that cover the transit of the regions between  $\pm 50^\circ$  heliographic longitude, out of the entire dataset, only NOAA region 11712, ( $\beta$ ) ended up with a negative value for the accumulated Poynting flux. Even in this specific case of NOAA 11712 the share of the energy that was removed via emergence was close to what is observed in the global median illustrated in Figure 35, reaching a value of  $\sim 55\%$  out of a total of  $-8.3 \times 10^{29}$  erg.

The values of every median, obtained from the dataset, represented by the horizontal lines within each interquartile box plot of Figure 36 are summarized in Table 7. The values for the medians of the energy injection across both components and their total are seen to range between  $\sim 9.3 \times 10^{31}$  erg and  $\sim 1.7 \times 10^{33}$  erg. The  $\beta\delta$  regions displayed a slightly higher median of  $\sim 1.8 \times 10^{33}$  erg

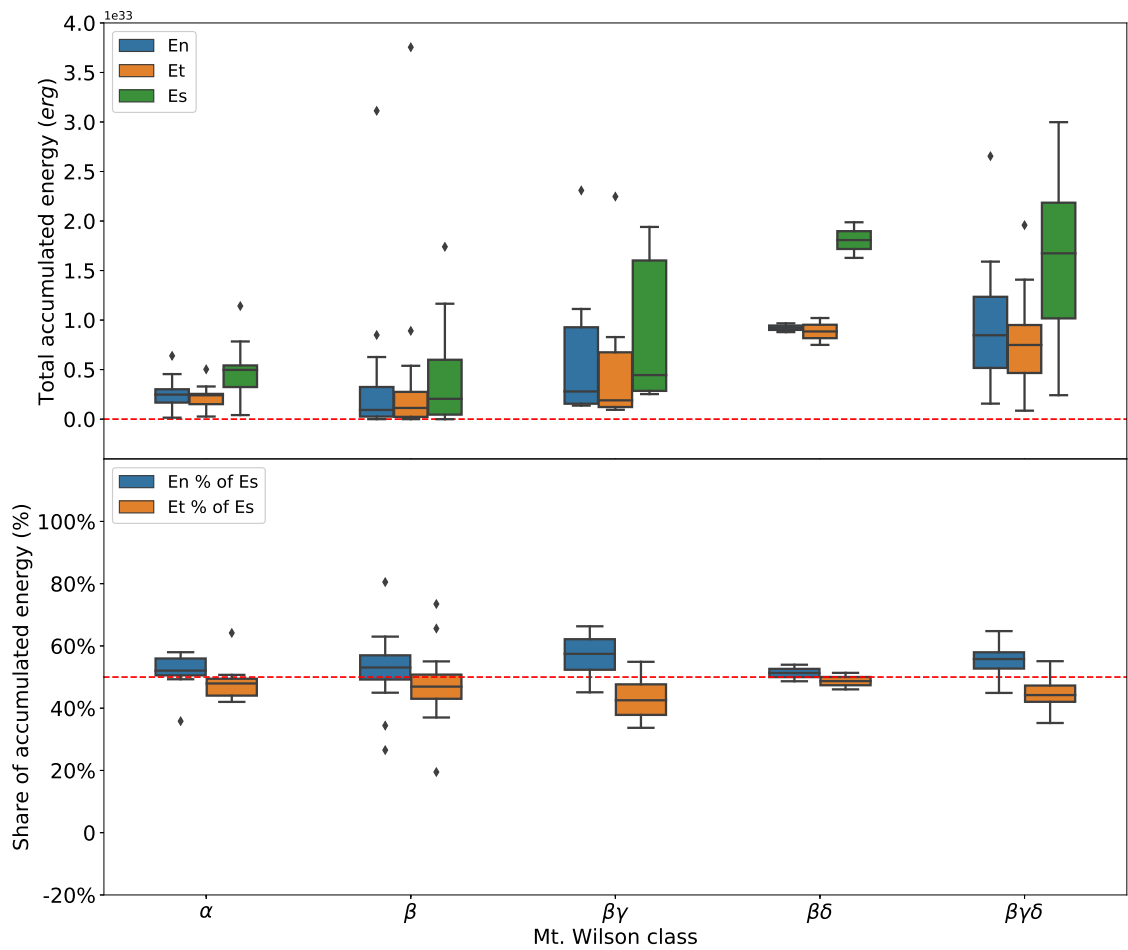


Figure 36: Top: Box-and-whisker plots of the lifetime-accumulated energy by emergence (blue) and shearing (orange) and their total (green), grouped according to the most-complex Mt. Wilson classification the ARs exhibited over their lifetime. The dashed red line indicates net zero change. Bottom: Box-and-whisker plots of the share of total lifetime-accumulated energy that is injected by emergence (blue) and shearing (orange), grouped according to the most-complex Mt. Wilson classification the ARs exhibited over their lifetime. The dashed red line marks the point where the contributions of the components are balanced.

for their total energy injection but, again, there are only two of them. Interestingly enough, the differences between the median values across the different Mt. Wilson classes are within one order of magnitude.

Surprisingly,  $\beta$  regions display a smaller median value across the two components and total energy than their  $\alpha$  counterparts. However, it must be taken into consideration that in this analysis ARs are labelled based on their single most complex classification issued during their lifetime. Therefore, an AR that spent most of its days as an  $\alpha$  but one day as a  $\beta$  would be considered  $\beta$  which may drive the  $\beta$  group values down. The  $\beta$  regions also include the region that is represented by the highest

Table 7: Median values from the box-and-whisker plots of lifetime-accumulated energy grouped by lifetime-maximum Mt. Wilson classification in Figure 36.

Lifetime-Accumulated Energy	Lifetime-Maximum Mt. Wilson Classification				
	$\alpha$	$\beta$	$\beta\gamma$	$\beta\delta$	$\beta\gamma\delta$
$E_n$ (erg)	$2.48 \times 10^{32}$	$9.26 \times 10^{31}$	$2.79 \times 10^{32}$	$9.23 \times 10^{32}$	$8.47 \times 10^{32}$
$E_t$ (erg)	$2.41 \times 10^{32}$	$1.13 \times 10^{32}$	$1.90 \times 10^{32}$	$8.85 \times 10^{32}$	$7.49 \times 10^{32}$
$E_s$ (erg)	$4.97 \times 10^{32}$	$2.05 \times 10^{32}$	$4.44 \times 10^{32}$	$1.81 \times 10^{33}$	$1.67 \times 10^{33}$
$E_n$ (% of $E_s$ )	52%	53%	57%	51%	56%
$E_t$ (% of $E_s$ )	48%	47%	43%	49%	44%

energy outlier, which is NOAA 12546. This region displays an energy injection of  $3.1 \times 10^{33}$  erg from emergence ( $E_n$ ) and  $3.8 \times 10^{33}$  erg from shearing ( $E_t$ ) leading to  $6.9 \times 10^{33}$  erg in total ( $E_s$ ), while it had a modest flaring activity over its lifetime of 11 B-class and 2 C-class flares. Notice that three of the  $E_s$  outliers are not displayed on the plotting area of Figure 36 as the axes were formatted to favour the visualisation of the IQR boxes.

The share of energy injected by emergence and shearing in the bottom panel of Figure 36 is observed to be distributed similarly to the results previously displayed in Figure 35 that combined every Mt. Wilson class. In all cases, the median and IQR of the emergence contribution lies above its shearing counterpart with only the  $\beta$ -most complex regions showing a slight overlap for their IQRs. The  $E_n$  share increases from  $\alpha$  (~52%), through  $\beta$  (~53%) to  $\beta\gamma$  (~57%) and  $\beta\gamma\delta$  (~56%). For  $\beta\delta$ -most-complex regions the difference between the components is much smaller with 51% of the energy being injected by emergence. However, as said before, only two regions on the dataset had  $\beta\delta$  as their most complex Mt. Wilson class so this may be due its small sample size.

### 6.3.2 Analysis per daily Mt. Wilson classification issued

The second task of this section uses all the daily issued Mt. Wilson classification of the ARs lifetime they will be carried matching the daily issue with the HMI data in two different ways. At first the data will be matched by its day stamp, which means that when the classification is issued at midnight all the HMI data of that day will be associated with it (labeled here as  $0 \rightarrow 24$ ). Another option is to use associate the data in the 24 hours that preceded the classification being issued, allowing us to observe how the energy injection behaved during the time that SWPC were collecting data to decide the AR classification (labeled here as  $-24 \rightarrow 0$ ). Then, the energy accumulation is

measured by summing the entries associated with each daily Mt. Wilson classification as defined by the two different time windows. When considering the daily count of Mt. Wilson classes, the sample sizes increase to 197  $\alpha$ , 168  $\beta$ , 68  $\beta\gamma$ , 13  $\beta\delta$  and 30  $\beta\gamma\delta$  for a total of 476 individual days over the 51 ARs. The daily Mt. Wilson classifications are then paired with the SHARP data in two different ways being those: the 24 hours of SHARP data before the classification is issued and the 24 hours of SHARP data following the classification being issued.

Since the HMI data acquisition and processing is incredibly reliable, there are not many missing data points in the data series to affect the calculation of daily energy accumulation. However, occasional gaps can be found in the series most of which are caused by basic instrument maintenance that includes calibration and maneuvering procedures. To produce the results of this Section, any missing data was filled using local linear interpolation to ensure that the daily sums are comparable. Also, as in the previous Section, any data from where the centroid of the HARP is beyond  $\pm 50^\circ$  longitude are discarded. Although this ensures that the data is less prone to the influence of disambiguation effects, it also creates an incomplete day record for the first and last days of the series of each region. For example, if an AR centroid crosses  $-50^\circ$  longitude at 16:00 the integration for that whole day will consist of the summation of only eight hours of injection (or removal). This can result in two days with atypically low injection, simply because there are less entries being summed. The first and last day of each series are thus also rejected from this dataset.

Figure 37 displays panels with the box-and-whisker plots of the daily-accumulated energies (top row) and the share of this accumulated energy that was injected via emergence and shearing motions (bottom row) according to the Mt. Wilson class issued. Each column represents one of the pairings between a day's worth of HMI data and Mt. Wilson class as proposed before covering  $-24 \rightarrow 0$  hours (left column) and  $0 \rightarrow 24$  hours (right column) from the issuing time of the Mt. Wilson class. Essentially Figure 37 provides the same analysis as Figure 36 but splits the data on a different timescale. This has the added effect of increasing the sample size for all classifications. Also, since the dataset is separated into daily entries, there are no biases in raw accumulated energy due to longer-living ARs (that tend to coincide with ARs of more magnetic complexity).

Unlike what is observed in the top panel of lifetime Figure 36, the whiskers of most boxes in the first row of daily Figure 37 are clearly seen to cross the red line that marks a net zero injection/removal during a day. This means that, although over their observed lifetimes ARs do not usually

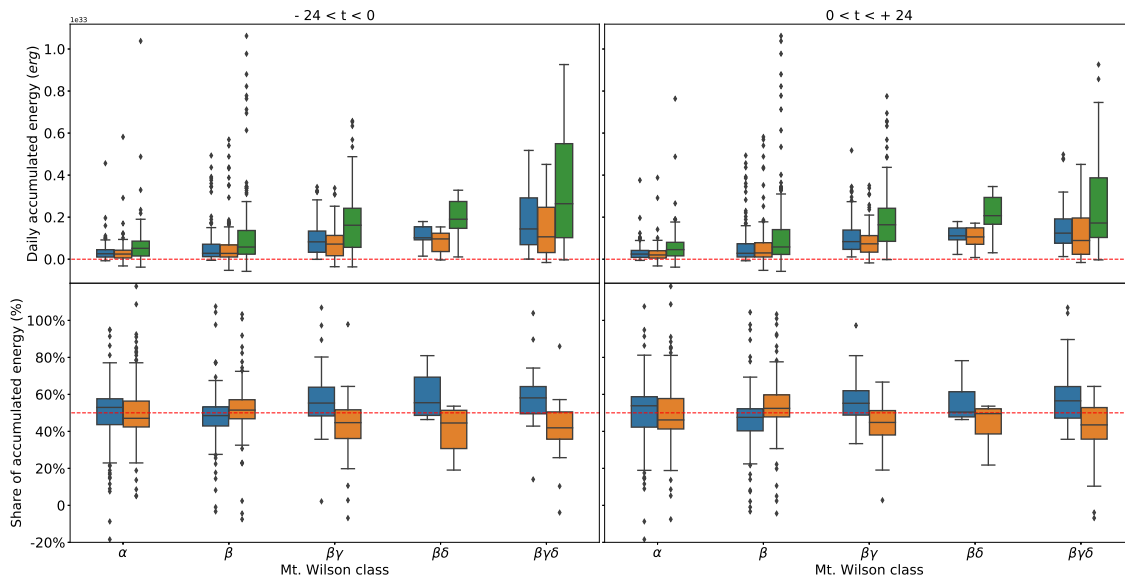


Figure 37: Same as Figure 36, but for daily-accumulated energies. The left (right) column contains the case for energy-accumulation over the 24 hours preceding (following) the Mt. Wilson classification being issued.

have a net negative Poynting flux, on a day timescale this happens more often. However, with the entirety of the IQRs of all the box plots covering positive values even on a daily sampling, injection is still the norm (representing close to 90% of the cases over all the entries in this dataset for both timescale association cases). The third quartiles of the boxes in the first row of Figure 37 show the most obvious variations between the different panels although the intervals covered by both the IQRs and whiskers are remarkably alike.

As the sample size increases the number of outliers also expands, concentrating themselves over the ARs with  $\alpha$  and  $\beta$  designation as they represent the majority of the sample size. However, looking at the daily entries it can be seen that the outliers almost exclusively happened in days where a region was either evolving up or down from more complex classifications. It is also important to keep in mind that the  $\alpha$  designations, although being morphologically simple, often have trailing plage that can have significant magnetic field through which flux can be injected. The largest outlier in the set corresponds to the evolution of NOAA 12546 (HARP number 6558). By the time NOAA 12546 saw this unusually large energy injection it was losing magnetic field complexity, going from  $\beta$  to  $\alpha$ , and the region had a significant size and polarity mixture with its trailing plage. The outliers in the  $\beta$  classification are all due to regions that evolved up to or down from more complex classifications.

Table 8: Median values from the box-and-whisker plots of daily-accumulated energy grouped by daily Mt. Wilson classification in Figure 37.

Daily-Accumulated Energy	Time w.r.t. Mt. Wilson Issuing	Daily-Issued Mt. Wilson Classification				
		$\alpha$	$\beta$	$\beta\gamma$	$\beta\delta$	$\beta\gamma\delta$
$E_n$ (erg)	-24 → 0	$2.59 \times 10^{31}$	$2.81 \times 10^{31}$	$8.24 \times 10^{31}$	$1.02 \times 10^{32}$	$1.44 \times 10^{32}$
$E_t$ (erg)	-24 → 0	$2.44 \times 10^{31}$	$2.75 \times 10^{31}$	$7.18 \times 10^{31}$	$9.64 \times 10^{31}$	$1.06 \times 10^{32}$
$E_s$ (erg)	-24 → 0	$5.17 \times 10^{31}$	$5.78 \times 10^{31}$	$1.62 \times 10^{32}$	$1.90 \times 10^{32}$	$2.64 \times 10^{32}$
$E_n$ (% of $E_s$ )	-24 → 0	53%	49%	55%	55%	58%
$E_t$ (% of $E_s$ )	-24 → 0	47%	51%	45%	45%	42%
$E_n$ (erg)	0 → 24	$2.44 \times 10^{31}$	$2.81 \times 10^{31}$	$8.35 \times 10^{31}$	$1.11 \times 10^{32}$	$1.24 \times 10^{32}$
$E_t$ (erg)	0 → 24	$2.01 \times 10^{31}$	$2.97 \times 10^{31}$	$7.31 \times 10^{31}$	$1.06 \times 10^{32}$	$8.89 \times 10^{31}$
$E_s$ (erg)	0 → 24	$4.54 \times 10^{31}$	$5.81 \times 10^{31}$	$1.64 \times 10^{32}$	$2.07 \times 10^{32}$	$1.72 \times 10^{32}$
$E_n$ (% of $E_s$ )	0 → 24	54%	48%	55%	50%	57%
$E_t$ (% of $E_s$ )	0 → 24	46%	52%	45%	50%	43%

The bottom row of Figure 37 shows some differences to what is observed looking at the lifetime injection of energy in Figure 36. Although over the different Mt. Wilson classifications most of the energy was still seen to be injected via emergence (as it was in Figure 36), the  $\beta$  regions on a daily scale are seen to have more energy being injected by the shearing component. For all other classifications the IQRs box-and-whisker plots show a slight growth in the share of energy that was injected by emergence when considering more complex ARs. For  $\beta\delta$  regions the medians show a balanced contribution for the 0 → 24 hour association but not for the -24 → 0 hour case, while the IQRs show that emergence plays a greater role in injecting energy. However, again, these results only portray a small number of regions and have less statistical significance. Cases where the share of energy is larger than 100% (all of which are outliers) come from ARs where the two components have opposite signs, leading to one of the components being larger than the total if their individual contributions are close in absolute magnitude.

Table 8, draws together the median values from the box-and-whisker plots of Figure 37, similar to Table 7, but now for the two definitions of the 24-hour data-association window. Table 8 show that the medians for the daily energy injection mostly grow with complexity and the difference between their lowest and highest values across the two components and their total is within one order of magnitude, as was observed in Section 6.3.1 for the lifetime sampling. Some ARs can see a larger imbalance between the total energy injected/removed via emergence or shearing. However, the medians of the distributions do not stray far from 50%, as can be seen in Table 8.

Comparing the columns of Figure 37, it is immediately possible to notice that the whiskers cover slightly different intervals, as expected since they represent energy accumulation being integrated over a shifted time period. However, the lack of an obvious difference in the IQRs or medians between the results portrayed in the two columns of Figure 37 may be an indication that the timescales of changes in energy injection that may be characteristic to any Mt. Wilson classification is more on the order of several days. This is consistent with previous works that show that ARs don't evolve significantly on a one-day timescale (c.f., McCloskey et al., 2016). This is further backed up by the number of daily entries that saw a change in Mt. Wilson classification in relation to the day before, which is 144 out of 501 showing that in more than 70% of the observations the classification remained stable. Thus, in the next Section the differences in energy accumulation that follow the evolution in Mt. Wilson classification is investigated to better understand if there are manifestations of energy injection linked to changes in Mt. Wilson class.

### 6.3.3 Poynting flux and the daily changes in Mt. Wilson class

It is also possible with this dataset to map the changes in Mt. Wilson class and compare the energy accumulation when the ARs are transitioning between classifications or remaining the same. Figure 38 shows how the daily-integrated Poynting flux values are distributed for regions when separated according to their assigned Mt. Wilson classification on a given day and what classification they receive on the next day. The column title indicates the starting classification of the ARs and the labels along the x-axis indicate the classifications that those ARs received at the start of the day following the energy accumulation. Additionally, it is important to keep in mind that only about a third of the daily entries show changes between days which undermines the statistical significance of some results, while some evolutionary changes did not have enough entries to create a box-and-whisker plot. However, the results here still offer indications of general trends that may later pave the way for further exploration considering all ARs in a whole solar cycle.

The left column in Figure 38 shows that the median values of energy injection for regions that kept their  $\alpha$  designation and regions that evolved from  $\alpha$  to  $\beta$  are not far apart but, surprisingly, the regions that kept their  $\alpha$  designation displayed a slightly larger energy flux. The IQRs extend over different ranges, but the location of the outliers in the regions that evolved to  $\beta$  hint that if more

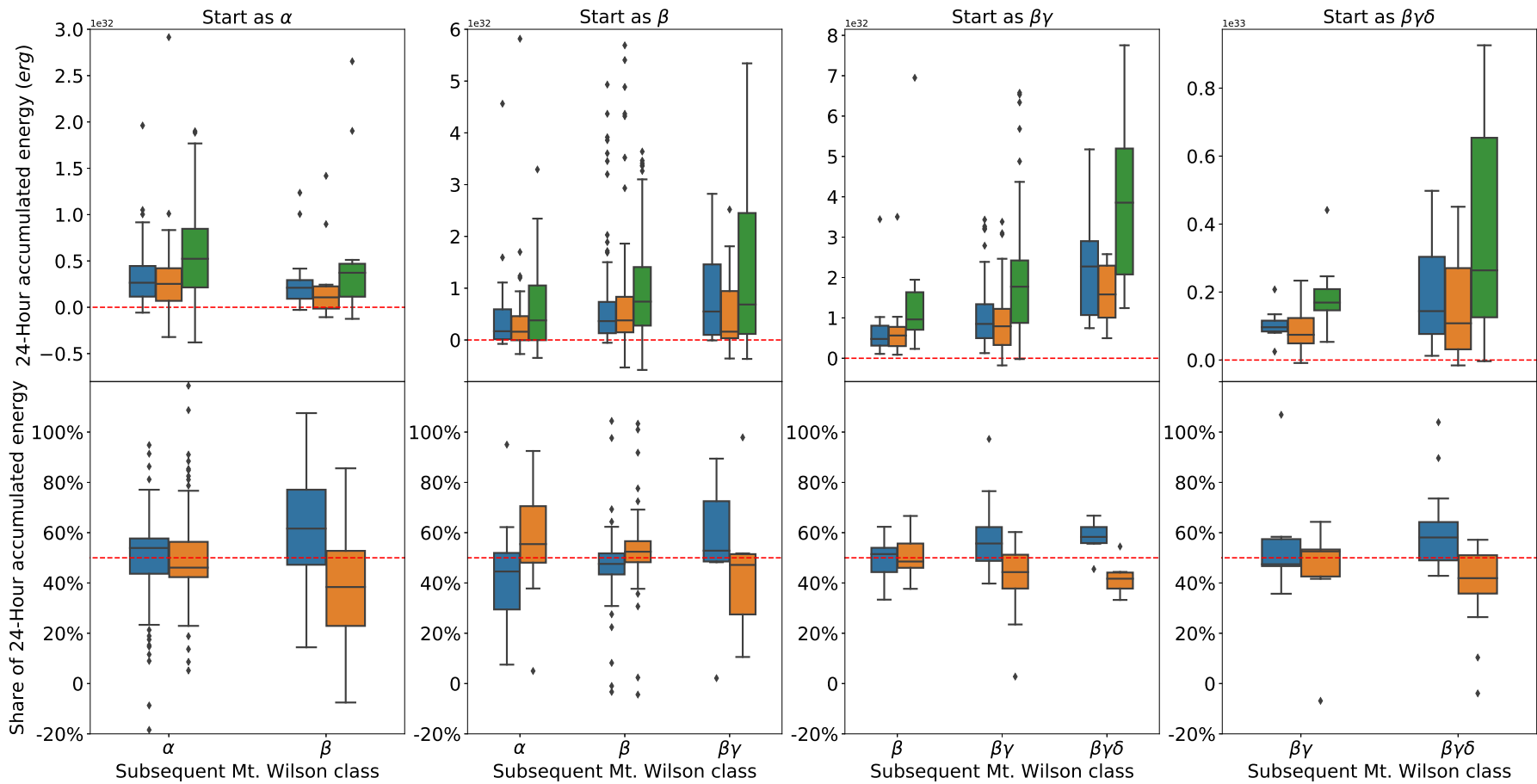


Figure 38: Same as Figure 36, but with the ARs separated into panel columns according to their daily starting Mt. Wilson classifications. In each panel the x-axis now displays the Mt. Wilson classification that the ARs subsequently evolve into at the end of the 24 hours that energy was accumulated over.

datapoints were used to make the boxplots their range might be extended. The bottom left panel of Figure 38 shows that the share of energy that is injected via emergence is predominant in regions that evolved to  $\beta$  which makes sense as this change in classification involves the emergence of a substantial amount of flux to strengthen the previously spotless polarity.

The Poynting flux of regions that started the day as  $\beta$  (second column from the left of Figure 38) see the intervals covered by the IQRs and their median values increasing following the evolution portrayed in the x-axis. Although the median value of  $E_s$  is similar for the regions that stayed as  $\beta$  and those that evolved to  $\beta\gamma$ , the emergence term is significantly more predominant in the regions that evolved upwards. This may at first be seen as an indication that the mixture of different polarities observed in  $\beta\gamma$  regions may build-up more through the emergence of new magnetic bipole structures than from the increased spatial mixing of existing ones.

Regions that started as  $\beta\gamma$  see a clear increase in their accumulated energy, median values and IQRs with evolving upwards to  $\beta\gamma\delta$  and decreasing values with evolving downwards to  $\beta$ . Regions that change from  $\beta\gamma$  to  $\beta\gamma\delta$  see an emergence of a delta spot in one of its polarities and seven different observations showed such change. It may be overly optimistic to state that this evolution is well represented, but the results in Figure 38 show that the majority of the energy for those regions is injected via emergence (as in Equation 3.16). Delta spots are small when compared to the total area of the spot and their contribution would be quite localized in the HARP image space often competing to the emergence of flux of opposite polarities that would be surrounding it.

Finally, for the regions that started as  $\beta\gamma\delta$  Figure 38 displays only two evolution cases, those being the regions that kept their  $\beta\gamma\delta$  designation and regions that evolved downwards into  $\beta\gamma$  (there was only one  $\beta\gamma\delta \rightarrow \beta$  evolution observed). Regions that kept their  $\beta\gamma\delta$  designation display more energy flux than the regions that devolved and most of this energy injection was performed by the emergence Poynting flux. The regions that evolved downwards into  $\beta\gamma$  typically have a larger share of their energy being injected by the shearing Poynting flux (shown by the median values) although the difference in the contributions of the two Poynting flux components is not as evident as the case of the regions that kept their  $\beta\gamma\delta$  designation, with significant overlap in the two energy component IQRs of those evolving from  $\beta\gamma\delta$  to  $\beta\gamma$ .

## 6.4 Discussion

As the results from Chapter 5 suggested, along with results in the literature (e.g., Liu and Schuck, 2012; Liu et al., 2014; Welsch, 2015; Su et al., 2018), a larger share of the energy being injected at the photospheric level is associated to the emergence Poynting flux ( $S_{\perp n}$ ). When looking over the lifetime of ARs portrayed in the box-and-whisker plots of Figures 35, the entire IQR of the emergence component energy is located above the line that marks 50% of the total energy injected. This shows that for the vast majority of the dataset (i.e., >75%) the energy injection was dominated by emergence. However, as the range covered by the whiskers and the outliers in Figure 35 show, there are also a minority of regions where the shearing Poynting flux injected a larger share of the energy. An example of this behaviour is NOAA 11283 studied by Romano et al. (2015) that had for most of its lifetime the shearing Poynting flux creating most of the energy injection.

Grouping ARs by their most-complex Mt. Wilson classifications, the median values for the share of total energy injected by emergence can be as large as 58%, observed for ARs with maximum complexity of  $\beta\gamma\delta$  in the  $-24 \rightarrow 0$  association (meaning that energies were accumulated over the 24 hours prior to the issuing of the Mt. Wilson classifications, see Table 8). However, the intervals covered by the IQRs in the top panels of Figures 36 and 37 show that, despite the leading role of emergence, both Poynting flux components inject a substantial amount of energy in ARs.

Curiously, on a daily timescale  $\beta$  regions are observed to have most of their energy being injected by shearing that can be seen in the bottom panel of Figure 37. There the box-and-whisker plots show that the shearing Poynting flux becomes more relevant for the total energy injection, with a difference of 2% ( $-24 \rightarrow 0$ ) and 4% ( $0 \rightarrow 24$ ) between the medians for the two components. This change in behaviour when looking at a different time scale is also a consequence of the regions being labelled based on their most complex Mt. Wilson class when looking at the lifetime injection. Then, as mentioned before, even if a region spent the majority of its lifetime as an  $\alpha$  only the most complex classification issued is considered. This may seem at first not to be in agreement with what is presented by Liu et al. (2014) as, out of the 28 regions studied by that author, 23 are  $\beta$  regions and the emergence Poynting flux accounts for  $\sim 56\%$  of the total energy injected. However, Liu et al. look specifically into emerging regions while here the data set is more diverse to try and sample what was observed by HMI through Solar Cycle 24. This difference in selecting the ARs makes the differences in the findings understandable.

The interval covered by the whiskers in Figures 36 and 37 show that the Poynting flux emergence component is more likely to be observed playing a leading role in the energy dynamics for any classification. Also, the box-and-whisker plots show that when energy removal takes place it is mostly associated with shearing and only very rarely is energy removed by emergence. A rather interesting behaviour of energy dynamics can be seen in the four regions studied by Bi et al. (2018) as for the majority of the ARs lifetimes the two Poynting flux components are seen to be working together to inject or remove energy. Also, these four regions studied by Bi et al. (2018) generally see more energy being injected or removed by the shearing. However, their Poynting flux was measured over a specific part of the image space covering a structure of negative polarity.

On a timescale of several hours or days, the Poynting flux is mostly net positive within the HARP image space. This can be clearly observed in the box-and-whisker plots in the top row of Figures 36 and 37 as only the lower whiskers are sometimes observed to cross the dashed red line that marks zero. As the accumulation time becomes shorter, more incidences of negative energy changes are observed over the whole HARP image space. However, considering the energy over the whole observed transit of the regions, only in one case did the data series end with net negative total energy. This was the case for NOAA 11712 and it comes with little surprise as this region is clearly observed to decay during its transit. NOAA 11283 that was studied by Romano et al. (2015) is also a good example of a region that ended up with a net removal of energy. However, unlike NOAA 11712 here, NOAA 11283 produced recurrent M- and X-class flares and CMEs.

The results across the different temporal samplings that are displayed in Figures 36 (whole AR lifetimes) and 37 (individual days) show that more complex regions are more likely to present larger values for the accumulated energy via Poynting flux. This can be quickly assessed by comparing the energy ranges covered by the different box-and-whisker plots, as well as the median values presented in Tables 7 and 8, where there is a clear upward progression in values as the Mt. Wilson complexity increases. Although there is an increase, the differences between all of the medians stay mostly within one order of magnitude even when comparing the least complex ( $\alpha$ ) and most complex ( $\beta\gamma\delta$ ) distributions. The median total energy accumulation values for  $\beta\delta$  regions were seen to be the largest among the different Mt. Wilson classes for one of the data association timescales (0  $\rightarrow$  24 hours), but those results are treated with scepticism as the number of ARs that fall into that category is simply not enough to be considered statistically relevant.

Some regions that were classified as  $\alpha$  and  $\beta$  produced outliers that seem oddly large when compared to their median value. However, even though this may be initially considered strange, there are a few relevant considerations about this. First, as discussed before, most of the regions that produced the outliers were evolving upwards to or evolving downwards from more complex classifications. Also, just because  $\alpha$  and  $\beta$  regions show on average smaller values of Poynting flux when compared to their more complex counterparts it does not mean that they cannot display a strong energy influx and these regions can and are known to produce significant energetic events. Finally, and most importantly, there is no coverage of the whole solar surface and the disambiguation effects prevent any accurate assessment of field at greater longitudes. Then, it is almost impossible to track an AR from emergence to decay meaning that the effects of energy injection or removal may not be fully observed and connected to changes in AR classification or energetic events that the AR may produce, as these may take place days after the energy rise or is removed from the photosphere.

Although the AR sampling did not allow Figure 38 to represent all the viable transitions that can occur between the different Mt. Wilson classifications as ARs evolve, the results can be quite insightful. First, the top row of Figure 38 shows that there is generally an increase in the energy values as regions are evolving into more complex classifications. This progression in the energy values covered by the IQRs and whiskers is neatly portrayed in the panels covering the regions that started as  $\beta$  and  $\beta\gamma$  (second and third columns) as they cover the three cases of evolving down in complexity, remaining the same, and evolving up in complexity. The exception to this can be seen in the panel that contains the regions that started as  $\alpha$ , as the box-and-whisker plots from the regions that kept their  $\alpha$  designation show that these ARs had more energy injection than the regions that evolved into  $\beta$ . Again, this can be a tricky assessment because regions with an  $\alpha$  designation can still have a significant amount of opposite flux in their trailing plage, essentially being a bipole, but without a spot showing in the continuum they will not receive a  $\beta$  designation.

Having a better knowledge on the specific energy accumulation associated to changes in Mt. Wilson class could be useful to predict solar activity, as indicated in McCloskey et al. (2016) where the connection between flares and changes in AR McIntosh classifications were explored. The authors found that regions that had an upward evolution showed larger flaring rates while regions that had a downward evolution see lower flaring rates in the day that followed the evolution. Although in

McCloskey et al. (2016) the McIntosh class is used to classify the ARs according to their white-light structural complexity and this information is used to associate AR evolution with flares, the McIntosh and Mt. Wilson classes can be mapped to each other making them interchangeable to a certain degree. Since there are considerably more possible McIntosh classifications than Mt. Wilson classifications a much larger dataset would be needed to have enough samples to explore the energy injection for the McIntosh classes as it has been performed here for Mt. Wilson.

The results presented by McCloskey et al. (2016) can be considered to be the end result of what is found here for energy injection. The easiest case to illustrate this with are regions starting as  $\beta\gamma$  in the top row of Figure 38. For those  $\beta\gamma$  regions evolving down to  $\beta$ , their reduction in magnetic polarity mixing comes with reduced energy injection (compared to those  $\beta\gamma$  regions that remained as  $\beta\gamma$ ) that will provide less energy to produce flares on subsequent days. The inverse is also clearly seen, where  $\beta\gamma$  regions that evolve into  $\beta\gamma\delta$  regions have significantly larger energy injection than their non-evolving counterparts. This in turn provides them with additional energy to produce flares in subsequent days, so long as the energy injection adds to the non-potentiality of the region. However, this is expected for the development of a  $\delta$ -spot because of the strong magnetic shear and twist that these structures display (e.g., Toriumi and Takasao, 2017).

The bottom row of Figure 38 show that there are different energy processes involved in how regions evolve. In all cases where regions evolve to a more complex classification the box-and-whisker plots across the different panels show that the energy is predominantly injected via emergence. The opposite also can be observed when regions evolve to a less complex classification, where the median values indicate that shearing becomes the leading energy injection process. However, checking the raw energies in the top panel shows that the IQRs for this injection remain smaller in magnitude than their counterparts in the non-evolving cases. As mentioned before, this also is in good agreement with the emerging ARs in Liu et al. (2014) as their evolution into (mostly)  $\beta$  regions is marked by a dominance of the emergence Poynting flux.

## Chapter 7

# Statistical relationship between Poynting flux behaviour and flare activity level

This Chapter will study the relation between energy injection in ARs and their flaring activity, both grouped according to their activity and also individually for the most extreme cases. The ARs used are the same ARs featured in Chapter 6 only this time the focus is on flaring activity obtained from the SWPC *Events* records. The list of all ARs used in this work can be found in Appendix A. Then, in this Chapter it is explored how the Poynting flux values change according to the flare class and if there are any manifestations of energy injection that are characteristic of these events.

Continuing on from Chapter 6, throughout this Chapter the timescale used to accumulate energy is the period where the ARs are between  $-50^\circ$  and  $+50^\circ$  longitude. However, since flares are produced from the free energy of ARs after some period of storage, the flare information used in here is gathered from  $-50^\circ$  to  $+90^\circ$  longitude (i.e., starting at the same eastern longitude but extending beyond the western-most point of energy accumulation). This was chosen because flares occurring before  $-50^\circ$  longitude are unrelated to the energy injection after this point, while the energy injected before  $+50^\circ$  longitude may be stored and later released as the AR approaches the western limb.

This Chapter then starts by studying the value distribution of the lifetime-accumulated energies of ARs grouped by the maximum flare activity attributed to every HARP after its centroid passes the  $-50^\circ$  mark following the SWPC Events records (Section 7.1). The goal of this section is to investigate how the manifestations of energy injection are related to flares. Unlike Chapter 6, not every option for temporal sampling will be considered as the previous results suggest that there is not a significant difference between the conclusions that can be obtained for the different temporal samplings. Also, there is no need to pair the flare time with the HMI sampling as each event is unique. Section 7.2 presents a detailed look at the ARs that produced the most intense flares (i.e., M- and X-class). Then those regions will be compared to verify if there are any similarities in their pre-flare energy dynamics as observed for NOAA 12443 and 12644 in Chapter 5. Section 7.3 investigates the lifetime-accumulated energies of ARs as a function of their lifetime-accumulated flaring activity. By effectively translating the flare class into a number it can then be more objectively compared with the energy injection in an case-by-case basis.

Before presenting and discussing the results there are a few considerations of general importance for this Chapter. As this study has its objective centred around understanding general aspects of energy injection for ARs and its connection to flares, other energetic activities such as CMEs were disregarded here. One example of the consequences of accounting for other energetic activities is that the regions that are grouped as ‘not flaring’ may have produced significant energy releases of a different nature. Then, the reader should not treat the non-flaring label as a sign of no activity. This leaves the opportunity for further work to be carried on in these regions as the database was designed to facilitate the addition of new content. New products derived from ARs (e.g., CME activity or magnetic helicity) can simply be added by creating a new results database table and connecting it to the central database table that contains the basic information of each AR.

## 7.1 Energy accumulation and maximum flare level produced

Considering the 51 HARPs in the dataset that contain only one NOAA region, 28 of those produced either no flares or up-to-and-including B-class flares, 16 had their maximum flare level as C-class, and 8 produced M- and X-class flares. This counts any activity that was reported in the SWPC *Events* files starting from the time the HARP centroid passed  $-50^\circ$  longitude. A- and B-class flares were grouped together because they have incomplete readings over the solar cycle. This happens

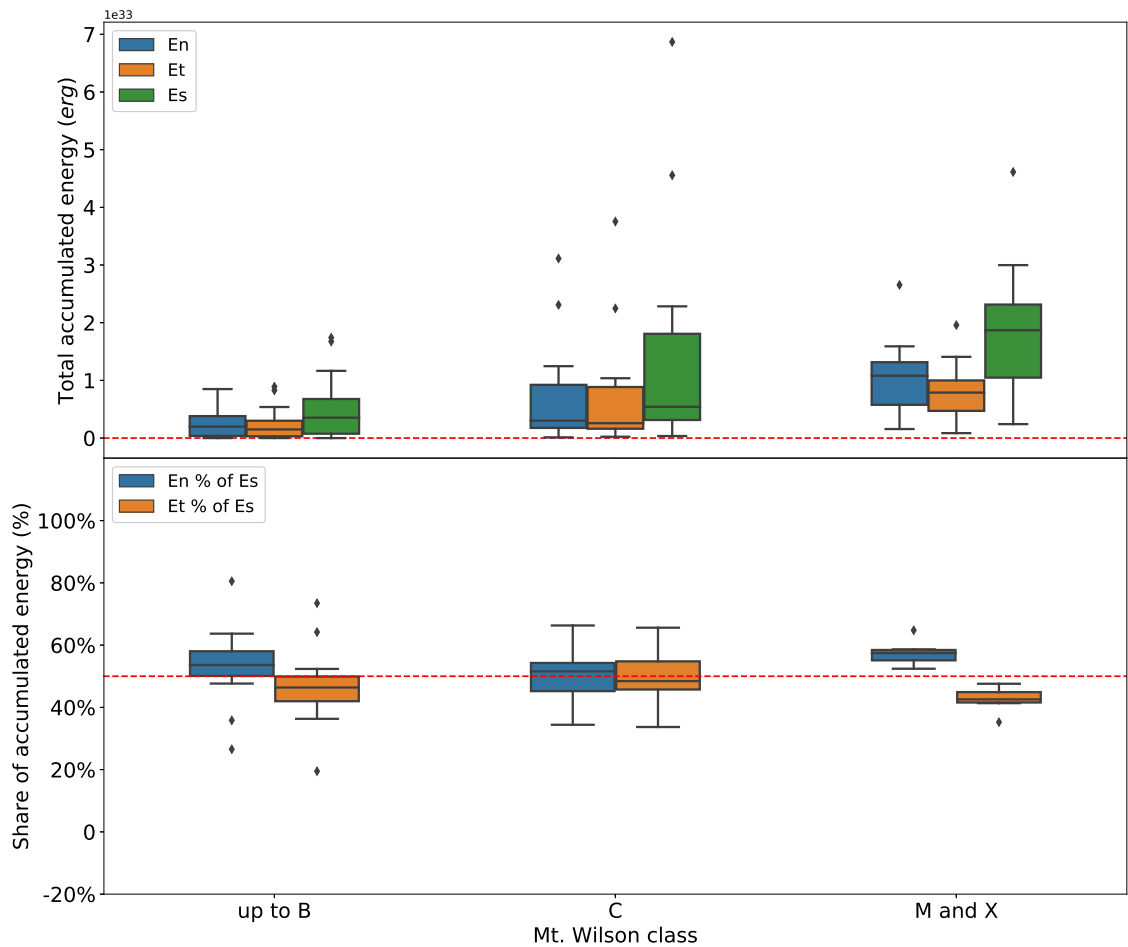


Figure 39: Top: Box-and-whisker plots of the lifetime-accumulated energy by emergence (blue) and shearing (orange) and their total (green), grouped according to the maximum GOES flare class the ARs exhibited over their lifetime. The dashed red line indicates net zero change. Bottom: Box-and-whisker plots of the share of total lifetime-accumulated energy that is injected by emergence (blue) and shearing (orange), grouped according to the maximum GOES flare class the ARs exhibited over their lifetime. The dashed red line marks the point where the contributions of the components are balanced.

because the background soft X-ray flux level varies through the solar cycle, rising up to high B-class or even low C-class level around the solar maximum making it impossible to observe these flares. Also, to make a box plot it is necessary to have at least 5 points and although algorithms can be forced to produce results for a smaller set it puts their statistical significance in check. Then for this section the regions that produced M- and X-class flares will also be grouped together.

The top panel of Figure 39 contains a box-and-whisker plot of the lifetime accumulated energy for every region in the dataset grouped according to the most intense flare activity they produced from  $-50^\circ$  to  $+90^\circ$  longitude. The value of every median, marked by the horizontal black lines

Table 9: Median values from the box-and-whisker plots of daily-accumulated energy grouped by maximum GOES flare class in Figure 39.

Lifetime- Accumulated Energy	Maximum GOES Flare Class Produced ( $-50^\circ \rightarrow +90^\circ$ longitude)		
	Up to and incl. B	C	M and X
$E_n$ (erg)	$1.98 \times 10^{32}$	$3.01 \times 10^{32}$	$1.08 \times 10^{33}$
$E_t$ (erg)	$1.49 \times 10^{32}$	$2.57 \times 10^{32}$	$7.88 \times 10^{32}$
$E_s$ (erg)	$3.53 \times 10^{32}$	$5.42 \times 10^{32}$	$1.86 \times 10^{33}$
$E_n$ (% of $E_s$ )	53%	51%	57%
$E_t$ (% of $E_s$ )	47%	49%	43%

inside the IQR boxes, can be found in Table 9. The IQRs and medians show a clear progression of increasing values with increasing maximum flare activity, observed across energy accumulated via the emergence (blue box) and shearing (orange box) components of the Poynting flux and also their total (green box). The value of the medians increase significantly with the flaring level and the energy injected across both components and their total mostly stays within the same order of magnitude. This behaviour is similar to what was observed in Chapter 6 (Figures 36 and 37) when the regions were grouped based on their Mt. Wilson class. This similarity is not quite a surprise as all of the 8 regions that produced the M- and X-class flares were issued a  $\beta\gamma\delta$  classification at least once over their daily Mt. Wilson classifications.

The lower panel of Figure 39 provides box-and-whisker plots of the percentage share of total energy accumulated via emergence (blue box) and shearing (orange box) distributed among the regions again grouped by maximum flaring level, with their median values also provided in Table 9. The regions that produced up to and including B-class flares saw in the vast majority of cases (i.e., 75%) more energy being injected via emergence (since the IQRs for emergence and shearing touch at the 1st and 3rd quartiles, respectively). In contrast to this, the C-class maximum group shows completely overlapping IQRs, although the emergence median lies slightly higher than that for shearing. The highest imbalance between the energy injection components occurs for the most extreme flaring group of M- and X-class producing regions for this grouping.

It is at first surprising that the regions that fall into the extreme ends of the grouping (up to B-class and up to X-class) in Figure 39 have most of their energy being injected by emergence while the group in between (Up to C-class) sees almost a perfect balance between the contributions for emergence and shear to the Poynting flux. However, regions that have their full emergence

capture by the HARP series see a whole magnetic structure emerging, which will then result in a larger share of  $E_n$ . Some regions like NOAA 12644 or 12673 that were observed to fully emerge and a few days after their full emergence triggered significant flare activity however, this sort of observation is a rather rare find. Most regions that are seen to emerge do not produce this sort of activity although they will also have a relatively high share of  $E_n$ .

One outlier in the regions that produced a maximum of C-class flaring displays an energy injection that is even above the highest observed for any of the regions that produced M- and X-class flares. However, considering the energy release estimations for flares (e.g., see Maehara et al., 2012) most of the 51 regions in the dataset had enough energy injected to produce these events which suggests that energy injection alone may not be sufficient to classify regions into flaring and non-flaring. Additionally, and probably most importantly, these calculations do not show which portion of the injected energy is ‘free energy’ that can be released in energetic events. Finally, HMI observations only cover one side of the Sun meaning that, unless they are seen to decay before rotating over the Western limb, there is no way to tell if they produced a flare later on in their lifetimes unless one is fortunate enough to find a record of it from the STEREO (Kaiser et al., 2008) mission. However, these would not be equivalent records to the GOES flares used here because there are no soft X-ray instruments on either STEREO spacecraft.

## 7.2 A closer look at the M- and X-class flaring regions

In Chapter 5, both NOAA 12443 and 12644 displayed an interesting surge in their Poynting flux components before their M- and X-class flares took place. Although other regions studied in the literature don’t necessarily share this behaviour, it was deemed interesting enough to investigate how often any similarities can be observed in the Poynting flux time series in the complete dataset days leading to M- and X-class flares. This section focuses on the time series of the eight regions that produced M- and X-class flares after their HARP centroids passed  $-50^\circ$  longitude. From these 8 regions only 6 produced their M-/X-class flares while located within  $\pm 50^\circ$  longitude. The two regions that produced their flares after  $50^\circ$  longitude are still considered in this study as a significant part of their evolution that precedes the flare activity is covered. The evolution of Poynting flux integrated over the entire HARP FOV of these 8 regions is displayed in Figure 40, with the red vertical lines marking the times where M- (dotted) and X-class (dashed) flares took

CHAPTER 7. STATISTICAL RELATIONSHIP BETWEEN POYNTING FLUX BEHAVIOUR AND FLARE ACTIVITY LEVEL

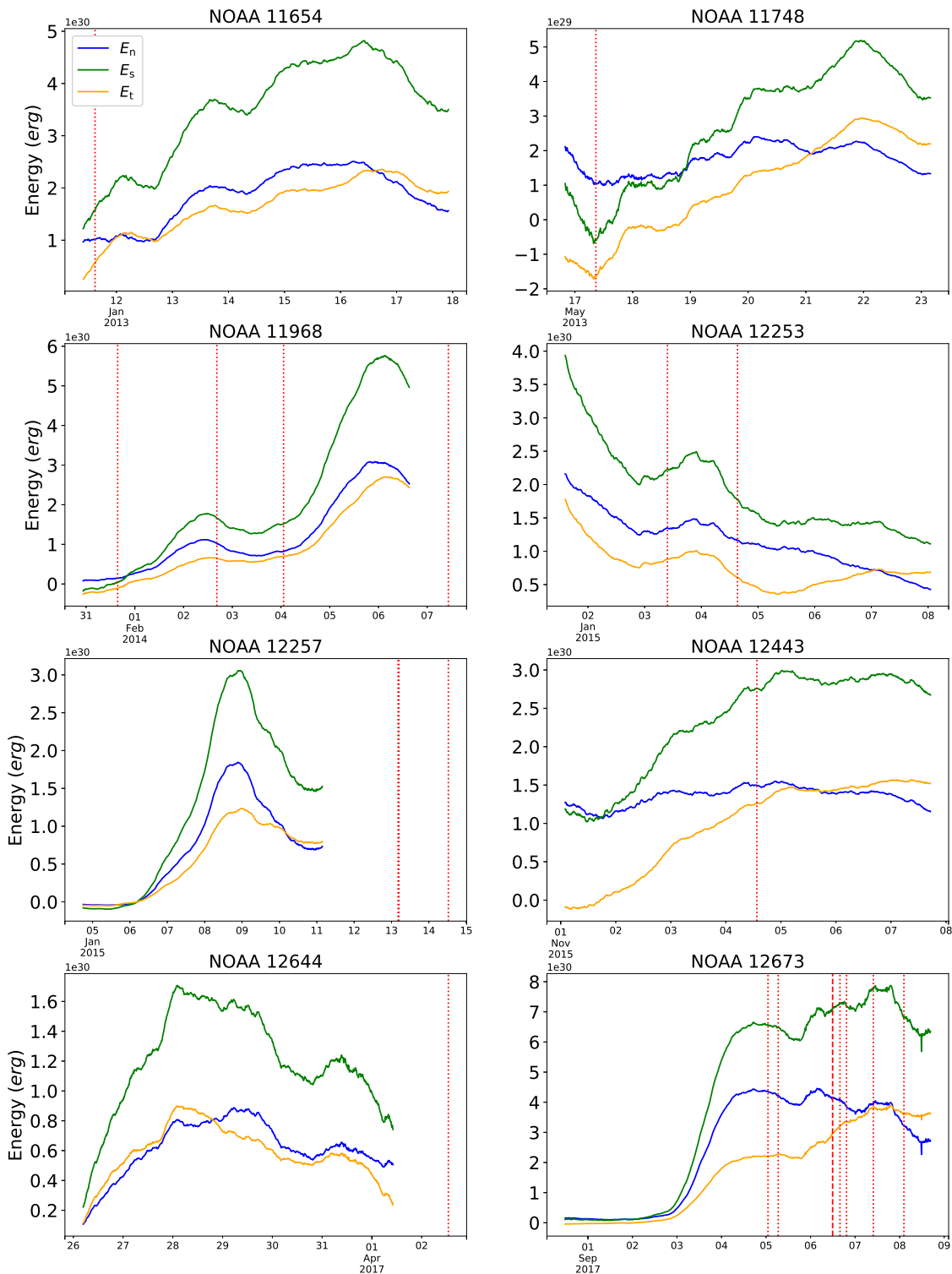


Figure 40: Evolution of energy injection via Poynting flux for NOAA regions 11654, 11748, 11968, 12253, 12257, 12443, 12644 and 12673. The blue, green and orange curves represent, the energy injected via the emergence, shearing and total Poynting flux, respectively. The red vertical lines represent the moment where the M- (dotted lines) and X-class (dashed lines) flares took place.

place. A rolling average with a centred 24-hour window was applied to each of these time series to smooth out the effects introduced by the HMI orbital period which creates a data loss of half a day at each end of the plot.

Surges in the Poynting flux akin to what was observed for NOAA regions 12443 and 12644 in Chapter 5 (Also in Figure 40) is not consistently observed for this subset of ARs illustrated in Figure 40. Even in this rather small set it is possible to observe how diverse the trend in AR energy injection is both before and after a flare takes place. The first surge in Energy levels observed for NOAA 12673 and NOAA 12644 are actually similar as it is a reflection of the spot emergence and structure formation. This result comes with little surprise because these are both emergent regions. However, their energy evolution show something interesting as both regions flared after a steep climb in their Poynting flux values showing that ARs can quickly after emergence gather enough energy to produce even X-class flares.

All the ARs in Figure 40 are in good agreement with what is shown in the bottom panel of Figure 39 where the energy injected by emergence is observed to be generally larger than its shearing counterpart and positive at almost all times. The shearing Poynting flux is observed to surpass the injection produced by emergence towards the end of the data series for NOAA regions 11654, 11748, 12253, 12257, 12443 and 12573.

It must be considered that although Figure 40 covers several days of AR energy injection, the analysis narrows down to the M- and X-class events. Then any flares that are C-class or lower and CMEs are not shown in the panels, as trying to look at every event may render the analysis fruitless due to a dense concentration of events in a short time interval. The uniqueness of the energy evolution displayed by each AR also does not come as a big surprise given that the ARs themselves can be quite unique in their morphology, size and evolution. However, the energy levels seen in these 8 regions are remarkably larger than what is observed in the rest of the dataset. It can be noticed that the total energy injected every 12 min in these ARs is mostly above  $10^{30}$  erg. The exception is NOAA 11748, whose values were on the order of  $10^{29}$  erg while also showing a considerable energy removal via shearing Poynting flux in the first day registered in its data series. Interestingly enough, all 8 regions considered here had  $\beta\gamma\delta$  as their most complex Mt. Wilson class over their lifetimes. During their evolution, the changes in the total energy injection mostly stays within the same order of magnitude after the ARs have first emerged.

### 7.3 Relationship between lifetime-accumulated energy and lifetime-accumulated flare index

In the previous Sections of this Chapter, ARs were grouped according to the largest magnitude flare they produced after the start of the energy accumulation window. The grouping of these ARs was based on the GOES flare class (i.e., the soft X-ray flux order of magnitude), but the class by itself draws a limited picture of these events. Consider an example of two ARs that produce a C9.9 and M1.0 as their largest flares over their respective lifetimes. These ARs would not be grouped together based only on their class, even though the peak X-ray flux of their largest flares are almost the same. In this Section, the energy accumulated via Poynting flux will be studied considering all flaring activity that the ARs produced after the start of the energy accumulation window.

To account for all flaring activity that ARs produce, the soft X-ray flare index (first devised by Antalova, 1996) is used in the form (Joshi and Joshi, 2004),

$$FI_{SXR} = 0.01 \times \sum_{n_A} m_A + 0.1 \times \sum_{n_B} m_B + 1 \times \sum_{n_C} m_C + 10 \times \sum_{n_M} m_M + 100 \times \sum_{n_X} m_X, \quad (7.1)$$

where  $m_{A-X}$  are the GOES-class multipliers that define the peak flux of each flare and  $n_{A-X}$  signify the summation over all flares of that GOES class that an AR produced. For example, in this formulation a single M5.0 flare will account for a contribution of 50 to the overall flare index. Then, all the activity produced by an AR after its HARP centroid passed  $-50^\circ$  longitude is summed using Equation 7.1 and compared to the energy accumulated by that AR between  $\pm 50^\circ$  longitude. The top panel of Figure 41 presents a scatter plot between the accumulated flare index and the energy accumulated by the emergence (blue) and shearing (orange) components of the Poynting flux and their total (green), while the bottom panel of Figure 41 then presents the share of the total energy that was injected by emergence (blue) and shearing (orange).

From the top panel of Figure 41 it is immediately obvious that all of the flaring ARs, regardless of how small their flare index was, are net positive over the lifetime of all regions. The distribution of the data points over the plot area suggest that there is a weak correlation between the accumulated flare index and the energy injected. In the bottom panel of Figure 41 it can be seen that all ARs with  $FI_{SXR}$  larger than  $\sim 30$  show a clear dominance of energy injection via emergence over their lifetimes as those  $E_n$  data points are consistently above the 50% line. Those data points

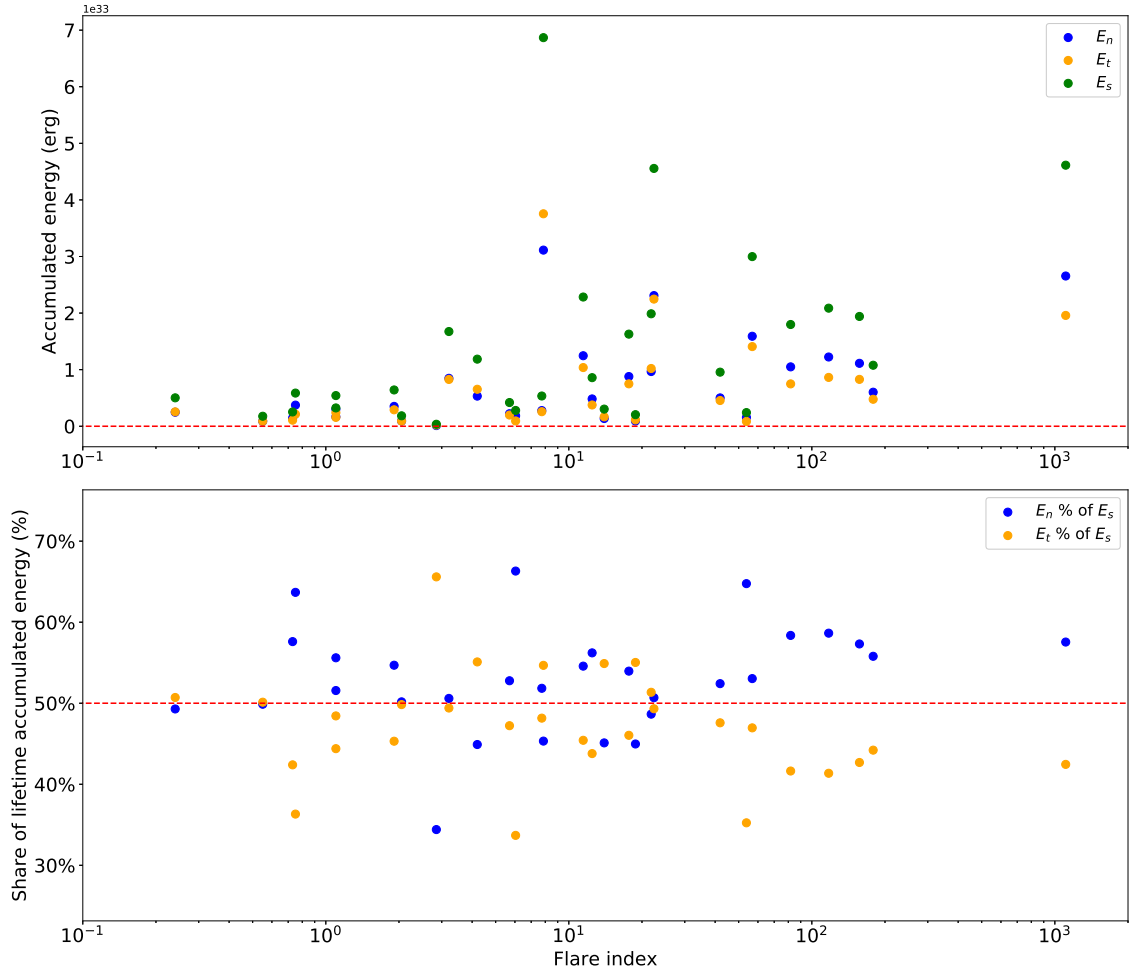


Figure 41: Top panel: Scatter plots of the lifetime-accumulated energy injected by emergence (blue) and shearing (orange) and their total (green) against the accumulated soft X-ray flare index of every region. The dashed red line indicates net zero change. Bottom panel: Scatter plots of the share of the lifetime-accumulated total energy that is injected by emergence (blue) and shearing (orange) the accumulated soft X-ray flare index of every region. The dashed red line marks the point where the contributions of the components are balanced.

with  $FI_{SXR} > 30$  are, in fact, the same eight ARs whose time series were portrayed in detail in Figure 40. In contrast, ARs with  $FI_{SXR} < 30$  show a considerably more mixed picture in terms of the largest share of energy being due to emergence in some cases and shearing in others with some tendency to more energy being injected by emergence for  $FI_{SXR} < 3$ .

## 7.4 Discussion

In this Chapter the results are produced based on the energy injection of 51 different ARs. The results cover a remarkable amount of the whole period that these ARs were observed on the disk

while still ensuring that the results are as free as they can be from the disambiguation problems related to the magnetic field measurements. This coverage is unique in the literature, as other works that have studied the Poynting flux in ARs mostly consist of case studies covering only a few hours (e.g., Aschwanden et al., 2014; Bi et al., 2018) or a couple of days (e.g., Liu and Schuck, 2012; Romano et al., 2015; Su et al., 2018) around the time the main flare/CME activity took place. This Chapter contributes to the existing knowledge with an extensive profiling of energy accumulation via Poynting flux in ARs with different levels of flare activity. Also, as ARs were selected to provide an accurate sample of the ARs that were observed in Solar Cycle 24, the results should approach a more general description. It is important to keep in mind though, any CMEs that these ARs produced are not taken into consideration, although the results database was designed in a way that facilitates a CME-specific table being added later for future studies.

When comparing the behaviour of 3 regions of different flaring activity to 5 non-flaring regions in Chapter 5, it remained unclear if the Poynting flux had any characteristic values or timescales that depended upon the AR activity. Also, it was proposed to verify if the surge in Poynting flux values observed prior to M-class flares in NOAA regions 12644 and 12443 present for other ARs. In this Chapter, Figures 39-41 were then created in an attempt to answer these questions making the best use of the available data while avoiding known sources of uncertainty, such as the HMI magnetic field disambiguation effects that were discussed before.

Figure 39 and Table 9 show that the lifetime-accumulated energy injection created by both Poynting flux components and their total is generally larger as the ARs display more intense flaring activity. This can be quickly verified by comparing the extent of the 3 IQRs and whiskers that have increased values with increasing level of activity, similar to what was observed in Chapter 6 when the ARs were grouped according to their Mt. Wilson classification. Although the differences in the median stay within one order of magnitude, the regions that produced the M- and X-class flares clearly stand out from the other two groups (i.e., regions that produced up to and including B-class flares and at maximum C-class flares). The large difference in the energy values observed in the regions that produced the most intense flares may, at first, strongly suggest that there is a characteristic level of energy injection for regions that produce such events.

A larger predominance of energy being injected by emergence as the level of activity exhibited by an AR increases can be noticed over the dataset. However, the total energy injected does

not stray more than 7% from a balanced contribution between the two components. The ARs that produced M- and X-class flares have in all the cases most of their energy injected by the emergence component of Poynting flux (bottom panel of Figure 39). Interestingly enough, regions that produced up to and including B-class flares also display most of their energy being injected by emergence. As this group has the largest share of emergent regions in the dataset it is not a surprise that their energy injection is dominated by the emergence Poynting flux component. A ‘proxy’ comparison for this group can then be made with what is reported in Liu et al. (2014) who studied helicity changes in 28 different ARs. Liu et al. (2014) show that the helicity injection for emergent regions has 56% of its total injected by its emergence component which, similarly to  $E_n$ , depends on both  $v_{\perp n}$  and  $B_t$ . Interestingly enough, the largest median in the share of energy injected by emergence was observed in those regions that produced M- and X-class flares ( $E_n \approx 57\%$  of  $E_s$ ) even though only one of those regions was an emergent region.

In Chapter 5 both NOAA regions 12644 and 12443 produced their M-class flares while their Poynting flux gradient was positive even though the timescale of the upward trend was different for the two regions. Such a pre-flare build up cannot be seen in the other ARs with the possible exception of NOAA 12673. This region displays strong growth during its initial emergence and spot formation that lasted for almost two days before the first two M-class flares took place. This was followed by a surge that lasted over almost a whole day before the series of M- and X-class flares, and another smaller surge before a final M-class flare. The last flare produced by NOAA 12673 happened when the values of energy injection were declining.

In Bi et al. (2018), where the Poynting flux of four different regions is compared, it is also not possible to identify a shared pre-flare behaviour. However, the observations in Bi et al. (2018) cover only a couple of hours looking at a specific structure in the image space which the author identify as being the footpoints of the flaring loops. In Romano et al. (2015), NOAA 11283 produced a series of M- and X-class flares and was shown (over most of the hours they focused on) to have an energy injection dominated by the shearing term, which is unlike any of the ARs in Figure 40.

There seems to be a weak correlation between the soft X-ray flare index ( $FI_{SXR}$ ) and energy injection in Figure 41. The 8 ARs with the largest  $FI_{SXR}$  (also in Figure 40) show a clear preference for emergence in their energy injection. However, some of the other regions stand out by showing

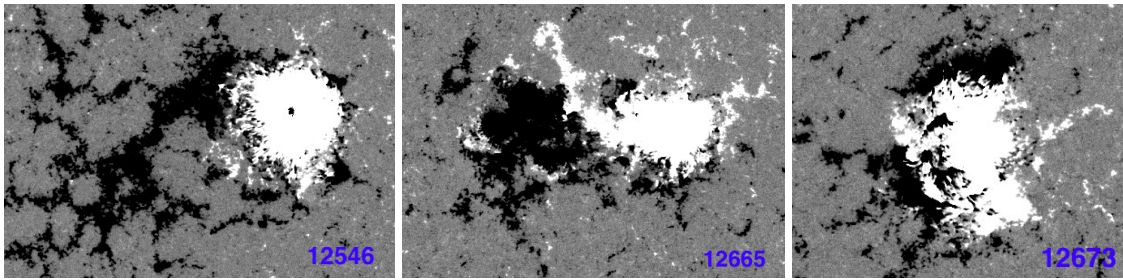


Figure 42: Magnetograms of NOAA regions 12546 (left; 2016-05-15), 12665 (centre; 2017-07-10), and 12673 (right; 2017-09-03). The regions were close to the disk centre at the time those images were produced. Source: LMSAL.

rather large lifetime-accumulated energies even though these did not translate into large  $FI_{SXR}$ . The three largest energy accumulations are observed for NOAA regions 12546 (highest total energy), 12665, and 12673 (highest  $FI_{SXR}$ ). Magnetograms of those regions taken when they were located close to the disk centre can be found in Figure 42.

NOAA 12546 (left panel of Figure 42) was observed on the disk from 2016-05-15 and consisted of a main spot with a strong opposite-polarity trailing plage. The evolution of NOAA 12546 was recently studied by Murabito et al. (2020) who found that that the region had a horizontal plasma velocity close to  $1 \text{ km s}^{-1}$  close to regions of where flux emergence was taking place. The strong horizontal motions reported by the authors come with little surprise given that NOAA 12546 was one of the few regions where its share of lifetime-accumulated energy was dominated by the shearing component of the Poynting flux. A corresponding AR (NOAA 12553) to NOAA 12546 was observed half a solar rotation ( $\sim 2016-06-12$ ) after NOAA 12546 disappeared in the Western limb showing that the region had a long lifetime. Altogether these findings makes one wonder if its flare index would change considerably if its activity could be tracked for an extended period of time.

NOAA 12665 (centre panel of Figure 42) was observed on the disk from 2017-07-06. Its flare index in Figure 41 is also observed to be relatively low compared to its accumulated energy. The calculation of NOAA 12665 flare index did miss some of the events it produced (including an M1.4 flare) as these took place before the  $-50^\circ$  longitude mark, although they would have been the result of energy injection from before the period used here. Wang et al. (2020) conducted a study of small-scale flux emergence in NOAA 12665 using the near-infrared imaging spectropolarimeter (NIRIS) finding signatures of energetic events such as Ellerman bombs (micro solar flares).

NOAA 12673 (right panel of Figure 42) was observed on the disk since its emergence that started on 2017-08-29 and is the region with the largest flare index in Figure 41. Furthermore, this region has its complete accumulated energy time series represented in Figure 40. This is an emergent region that quickly rose in energy and produced a series of intense flares, which took place while the region was close to disk centre. With such a unique set of features, it is not a surprise that a number of studies about the evolution of this region can be found in the literature. Verma (2018) specifically looks into how strong shearing flows in NOAA 12673 caused the existing spot to merge with the trailing structure. The strong horizontal motions within the main spot area were also studied by Romano et al. (2019), showing that during the flare the horizontal velocities in the main spot structure caused the null point height to vary in time which could have created favourable conditions for the X9.7 flare to take place. Despite these remarkable shearing motions that were studied in great detail by such authors, Figure 41 here shows that slightly less than 60% of this AR's energy was injected by emergence, although the 40% due to shearing does amount to  $\sim 2 \times 10^{33}$  erg. A closer look into the emergence of new flux and changes in the morphology of NOAA 12673 around this flaring activity can be found in Li et al. (2019), which neatly portray how quickly the spot and penumbral area increased prior to these major flares.

The largest energy injection observed was that of NOAA 12673 which emerged close to the disk centre. Its energy injection quickly rose to surpass that shown by the other 7 regions displayed in Figure 40. The average of its lifetime-accumulated Poynting flux was still the largest in the set, even though the first few days include its pre-emergence period where energy injection was negligible. NOAA 12673 then unleashed a sequence of M- and X-class flares that is unmatched in the data set. This showcases how quickly an AR can build-up energy for flaring, even though potentially only up to 25% of the energy may be free energy (cf. Aschwanden et al., 2014).

There is a significant difference in size between the 8 regions that produced the most intense flares and the other regions in the set. This difference of roughly 200 pixels in both latitude and longitude covered by the HARP FOV between those two groups creates an average difference close to  $2 \times 10^{16}$  m<sup>2</sup> in the area covered by these HARPs. All the Poynting flux whiskers show most (if not the entirety) of their ranges covering positive values, showing that the energy injected by emergence and shearing is predominantly positive. Then, over a larger spot and plage area this difference in size should mostly result in a larger Poynting flux over the HARP image space.

The study that perhaps bring the most comprehensive statistical analysis of parameters derived from solar data and involve the Poynting flux was carried on by Tan et al. (2007) before the SDO era. The author finds that among the measurements derived from the magnetic field the parameter with the best correlation with the soft X-ray brightness is the Poynting flux density (0.71). Although by the time only the proxy Poynting flux could be calculated, the results in Figure 39 show that there is a clear progression in the value covered by the IQRs and whiskers suggesting that indeed there might be a significant correlation between the Poynting flux and flare activity. On the other hand, the results in Figure 41 show that the flare index of a region and the amount of energy a region accumulate have at best a weak correlation. The correlation could significantly improve if the ARs could be fully tracked as NOAA 12546 for example had a lifetime larger than a solar rotation and only  $\sim 1/3$  of the ARs activity can be tracked here.

While the time series of Figure 40 show that the Poynting flux evolution of flaring ARs is not much alike, Figures 39 and 41 offer indications that there is a certain correlation between Poynting flux and the flare activity that an AR produces. However, as expected, flare activity is connected to a larger variety of factors as already discussed by Leka and Barnes (2003) and should not be able to be fully predicted using the Poynting flux alone. Looking at the HARP FOV size of these 8 ARs and their magnetic field morphology they show some contrast to the other ARs in the complete dataset. On average these 8 flaring ARs had a HARP FOV of  $\sim 500 \times 900$  pixels, which is considerably more than the  $\sim 347 \times 676$  pixels average displayed by the other 43 ARs, and also all 8 of these ARs were issued a  $\beta\gamma\delta$  classification at some point during their lifetime.

There are many works that devote their efforts to study ARs that produce a significant activity and, mostly, they limit the analysis to a few minutes or hours around the event that is being studied. In this study the ARs were selected to represent an accurate picture of what was usually seen over Solar Cycle 24 and the analysis extends itself for as much as possible for every AR regardless of activity or complexity. Thus, the results presented here are in a unique position to describe the general properties of the Poynting flux in ARs. Furthermore, the algorithms were developed in a way to facilitate both the continuity (i.e., adding more ARs to the database) and extension (i.e., adding more products to the database) of this work. Then, given time and resources, the pipeline could process all of the ARs observed by HMI in Solar Cycle 24 (and eventually Solar Cycle 25) providing the most complete picture that could be created on the Poynting flux in ARs.

## Chapter 8

# Conclusions & Future Work

This final Chapter is divided in two sections. First, Section 8.1 summarizes the primary results presented in Chapters 5-7 while emphasizing how this work contributes to the existing knowledge. Then, Section 8.2 provides suggestions for future work that could extend what was presented here to further explore the topic of AR energetics and their relation to flaring activity.

The results of this thesis were based on a sample of 51 different ARs that were carefully sampled to provide an accurate representation of Solar Cycle 24. Each AR has its Poynting flux processed for its whole observation time, although due to disambiguation problems the analysis is constrained to when the HARP centroids are within  $\pm 50^\circ$  Heliographic longitude. One factor that contributes to this reduced number of ARs is that ARs often appear in groups, especially around the peak of the solar cycle, making it challenging to find HARPs with just one NOAA region in the FOV. Furthermore, considering that the magnetic field vector data is increasingly more reliable as the observed regions approach the disk centre, finding data that is appropriate for this study is a challenge by itself, given the amount of constraints. Trusting that the sampling of regions that was created based on information extracted from years of SWPC reports was accurate, the results contained here should offer a meaningful insight for future studies that will be able to take place as the database of HMI products gets larger.

## 8.1 Principal results

### 8.1.1 Case study of the Poynting flux of 3 flaring and 5 non-flaring ARs

#### Removal of field-aligned velocities

The total Poynting flux ( $S_s$ ; Equation 3.6) depends on a cross product and, therefore, its calculation is not affected by the field-aligned velocities that come as a result of feature tracking methods. However, calculation of the Poynting flux components for emergence ( $S_n$ ; Equation 3.7) and shearing ( $S_t$ ; Equation 3.8) depends on dot products which are then susceptible to the influence of field-aligned velocities. The scatter plots of Figures 25 and 26 show that not removing the field-aligned velocities causes the velocity components to be shifted by up to  $0.5 \text{ km s}^{-1}$  in the horizontal sense and up to  $0.2 \text{ km s}^{-1}$  in the vertical sense. This severely impacts the calculation of the individual Poynting flux components, evidenced by the corrected versions (i.e.,  $S_{\perp n}$  and  $S_{\perp t}$  in Equations 3.16 and 3.17, respectively) displaying pixel differences as large as  $\pm 10^9 \text{ erg cm}^{-2} \text{ s}^{-1}$ . Thus, it is clear that removing the field-aligned flows from the output velocities of feature tracking methods is a mandatory step if the individual components are being calculated.

#### Profiling the Poynting flux values across the HARP image space

To understand the distributions of energy injection values, Chapter 5 explored the Poynting flux components and total across the whole lifetime of an initial sample of 8 ARs (3 flaring; 5 non-flaring). The histograms of  $S_{\perp n}$  (Figure 27),  $S_{\perp t}$  (Figure 28), and  $S_{\perp s}$  (Figure 29) outline that individual pixels range from approx.  $\pm 10^2$  to  $\pm 10^9 \text{ erg cm}^{-2} \text{ s}^{-1}$ , peaking close to  $10^6 \text{ erg cm}^{-2} \text{ s}^{-1}$ . This large dynamic range indicates that most of the energy injection is concentrated in less than 5% of the HARP FOV pixels. The largest differences in the AR pixel distributions are observed for the two regions that produced M-class flares (i.e., NOAA 12443 and 12644), which stand out from the average-distribution of the non-flaring regions because these M-class producing ARs display a greater frequency of high-valued Poynting fluxes. It is also worth noting that, for all regions considered, the peaks of the total Poynting flux distributions lie close to the energy flux requirement for coronal heating.

### **Evolution of energy injection**

Each of the 3 ARs with differing flaring levels had their point-in-time energy injection and cumulative energy time series displayed along with the 5 non-flaring ARs in Figures 31 and 32, respectively, in order to compare the evolution of flaring and non-flaring regions. Only the energy values for the AR that produced the most flare activity (NOAA 12443) were seen to clearly stand out from the non-flaring ARs. The intermediate flaring region (NOAA 12644), that was an emergent region, showed similar levels of energy injection and accumulation compared to the non-flaring regions. The weakest of the flaring regions (NOAA 11072) displayed smaller levels of energy injection than most non-flaring regions. In relation to flaring activity, both NOAA 12443 and 12644 underwent significant increases in energy injection before each of their M-class flares occurred, although these were over quite different time scales of  $\sim 1$  day and  $\sim 5$  days, respectively.

### **8.1.2 Differences in Poynting flux behaviour between Mt. Wilson classifications**

#### **Overall energy share**

The role of the Poynting flux emergence and shearing components in the overall energy dynamics of ARs was studied in Chapter 6 over a statistical sample of 51 individual ARs. For the share of total energy accumulated over the AR lifetimes, the interquartile ranges (IQRs) of Figure 35 show that more energy is injected by emergence than shearing in  $\sim 75\%$  of the ARs (typically at the 50 – 60% level, with a median of 55% over the whole dataset). Despite this, the contribution of the shearing component is still significant for most ARs. Only in one case (NOAA 11712) was the lifetime-accumulated energy net negative.

#### **Energy accumulation and Mt. Wilson classification**

The 51 ARs were then divided according to their Mt. Wilson classifications to study how the energy values and preferred mechanisms of energy injection might change with AR magnetic complexity. Once again, the dominance of the emergence Poynting flux was consistently observed across almost all Mt. Wilson classifications. In addition, it was found that the ranges of energies accumulated in ARs clearly grow with increasing magnetic complexity. The fact that this trend of increasing lifetime-accumulated energy with increasing lifetime-maximum Mt. Wilson classification (Figure 36) is replicated in the daily-accumulated energies vs daily-issued Mt. Wilson

classifications case (Figure 37) confirms that the results from the former are not simply a biasing effect of more magnetically complex regions having longer lifetimes.

### **Energy accumulation with evolution in Mt. Wilson classification**

The investigation of Chapter 6 then proceeded to study the distributions of energy injection in ARs in relation to their evolution in Mt. Wilson classification. It was found that ARs which evolve upwards in magnetic complexity, with the exception of those that start as  $\alpha$ , display larger values of energy accumulation during the day leading up to the change in classification in comparison to their counterparts who maintain their classification. The opposite was also found, such that ARs which evolved downwards in magnetic complexity display smaller values of energy accumulation than those that remain as the same classification. Furthermore, ARs that evolve upwards in Mt. Wilson classification have a more pronounced share of their energy being injected by emergence, the most clear case being for  $\beta\gamma$  regions that evolve into  $\beta\gamma\delta$  which resulted in the IQRs of emergence and shearing being totally separated. This shows that the main mechanism behind these changes in magnetic complexity is the emergence of new magnetic flux. Since ARs see their energy levels increasing during the day before the Mt. Wilson classification increases, monitoring energy injection in near-realtime could be useful for short-term space weather forecasting.

### **8.1.3 Statistical relationship between Poynting flux behaviour and flare activity level**

#### **Energy accumulation and maximum GOES flare class**

The energy injection of the same 51 ARs was studied in Chapter 7 by dividing these into groups according to the maximum GOES flare class they produced in their lifetime. It was found that the medians of the lifetime-accumulated energy distributions (and their whole IQRs) shift to greater values as the maximum flare class increases (upper panel of Figure 39). The clear preference for energy injection by emergence is reflected in the distribution medians being 53% (up to and including B-class), 51% (C-class), and 57% (M- and X-class). This injection imbalance is most clear for the ARs that produced M- and X-class flares as their maximum flare class, not only because of having the largest median values for the share of energy injection but also because the whole range covered by the IQRs and whiskers of the two components are completely separated.

### **A closer look at the M- and X-class flaring regions**

The time series of energy injection of the 8 ARs that produced M- and X-class flares were also studied and compared to search for any similarities that may exist in the hours or days leading up to these major flares. The growth of energy injection observed for NOAA regions 12443 and 12644 in Chapter 5 is not consistently observed in the time series of the additional 6 ARs in Chapter 7. However, NOAA 12673 does display two periods of significant growth in energy injection, the first preceding a pair of M-class flares and the second preceding an X-class and two M-class flares. Also, all of the regions that produced the M- and X-class flares were classified as  $\beta\gamma\delta$  at some point over their lifetimes.

### **Relationship between lifetime-accumulated energy and lifetime-accumulated flare index**

The lifetime-energy accumulated by the emergence and shearing components of the Poynting flux was then studied for the 51 ARs as a function of their accumulated soft X-ray flare index ( $FI_{SXR}$ ). A weak correlation was found between the lifetime-accumulated energies and the  $FI_{SXR}$  (Figure 41). However, the AR observations used here to calculate accumulated energy are limited to  $\sim 1/3$  of the solar surface, which will affect the correlation observed in this post. Regions like NOAA 12546 that accumulated the most total energy but produced only modest  $FI_{SXR}$  may have continued to exist and produce significant flaring activity after rotating beyond the West limb. This is supported for NOAA 12546 by the fact that a mature spot group (NOAA 12553) was observed to rotate over the East limb at the same latitude half a solar rotation later. The ARs with the largest values of flare index (i.e.,  $FI_{SXR} > 30$ ) show a clear preference for emergence as the primary mechanism of energy injection (bottom panel of Figure 41).

## **8.2 Future work**

### **Extended analysis**

To ensure that the results here approach a general description of the energy injection in ARs at the photospheric level, the dataset was selected based on what was observed by HMI up to 2018 covering a significant part of Solar Cycle 24. Although there is no vector magnetic field data with a consistent temporal sampling for the ARs of Solar Cycle 23, with the start of Solar Cycle 25 it

is now possible to start exploring possible differences in the energy injection of ARs of different cycles. Carrying on comparisons of this nature should be possible in less than 10 years as Solar Cycle 25 will be completed (or close to completion). With the improvements seen over the years in access and quality of solar data, including new instruments, the chances are the conditions will be favourable to conduct such work.

The database was designed in a way to facilitate the incorporation of new AR-related data. Then, any new products can still be associated with the central table containing the basic information (e.g., HARP number and NOAA number) of each AR. Data from CMEs can then be mined from the existing catalogs of CME activity and inserted in the database. This way, all the main energetic releases that ARs generally produce would be covered allowing a more complete description of their evolution. Since most of this data will consist of text and numbers the database space requirements would essentially stay the same.

Future studies that attempt to reconstruct the results of Figure 39 using an even larger dataset could, and probably should, create subgroups when grouping the flares. For example, in here a C1.0 flare would be in the same group as a C9.9 flare even though the difference in the X-ray flux of these two events is off by almost an entire order of magnitude with the latter being notably close to M-class. However, even in a larger dataset the limitations involved in measuring the magnetic field vectors close to the limbs will most likely still be present and care must be taken to avoid biases in the data.

### **Magnetic helicity and magnetic field extrapolations**

The extrapolated 3D magnetic field and maps of the magnetic helicity also could be added to the database. Adding these two products however would increase the database demands for space and also take a considerable computational time. Over this work it was pointed out several times how much being able to track the energy content on the 3D field, especially the energy budget, could contribute to interpreting the results. Also, the magnetic helicity could be particularly helpful to differentiate drops in the energy content caused by flares and CMEs as it is conserved during flares.

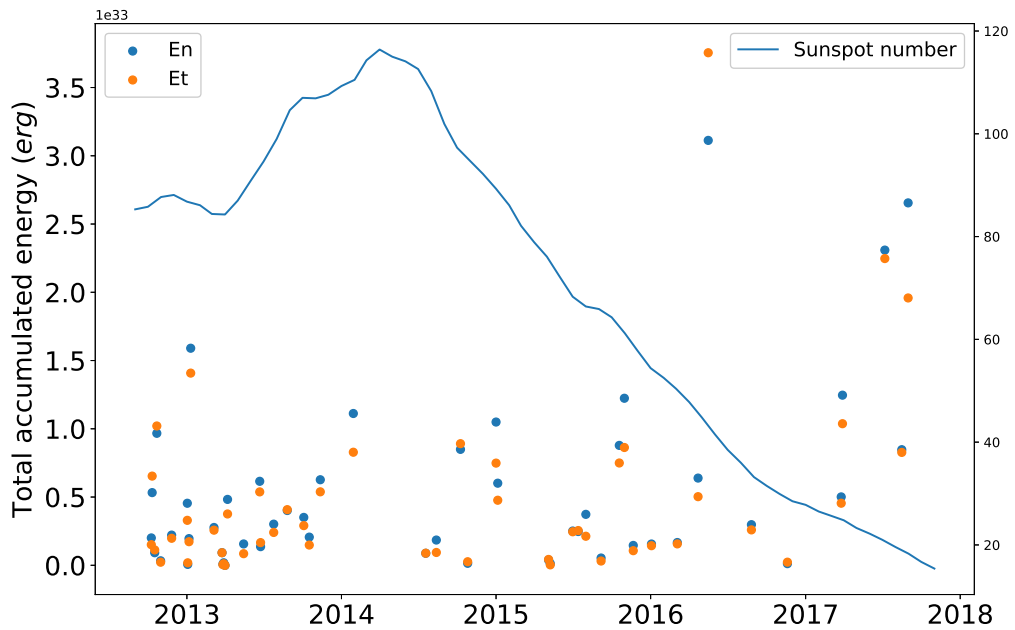


Figure 43: Lifetime-accumulated energy for all of the ARs in the complete data set as a function of their NOAA number.

### Energy injection across the Solar Cycle

It is not the objective of this work to evaluate how energy injection distributes itself in ARs as a function of the solar cycle itself. However, given that NOAA designations for ARs increase fairly orderly as the regions appear in the disk the NOAA number itself can be used as a proxy for the time passage and, thus, to track the solar cycle itself. Given that the data used in this study was gathered fairly spread over the cycle starting with NOAA 11586 (2012-10-09) and ending with 12673 (2017-09-09) the data points are spread around its peak that happened in 2014. Then, Figure 43 brings the lifetime-accumulated energy for each AR in the dataset and the 13-month smoothed sunspot count (SILSO World Data Center, n.d.). In February of 2014 the NOAA numbers assigned were close to 1200 and the data points were showing a faint indication of a growing trend although these values are still significantly smaller than the largest values in the set. It may be worthy for future works that have access to data from all the regions of the HMI era to remake Figure 43 as that may actually show if the energy injection also has some variation with the cycle or not.



## Appendix A

### List of ARs used in this work

Table 10: List of ARs featured in this thesis (2012–2013).

HARP Number	NOAA Number	Date of First NOAA Designation	Most Complex Mt. Wilson Class	Total Number of GOES Flares
2107	11586	2012-10-9	$\alpha$	0
2109	11589	2012-10-11	$\beta\gamma\delta$	12
2117	11593	2012-10-17	$\beta$	10
2137	11598	2012-10-22	$\beta\delta$	31
2166	11602	2012-10-31	$\beta$	0
2240	11621	2012-11-26	$\beta$	6
2341	11642	2013-1-2	$\alpha$	0
2342	11643	2013-1-3	$\beta$	1
2358	11649	2013-1-6	$\beta$	0
2372	11654	2013-1-10	$\beta\gamma\delta$	22
2522	11689	2013-3-6	$\beta$	7
2585	11705	2013-3-27	$\beta$	0
2587	11704	2013-3-25	$\beta$	9
2598	11707	2013-3-29	$\beta$	0
2610	11712	2013-4-1	$\beta$	0
2635	11719	2013-4-7	$\beta\gamma\delta$	7
2748	11748	2013-5-15	$\beta\gamma\delta$	16
2878	11777	2013-6-22	$\beta$	2
2887	11778	2013-6-24	$\beta\gamma$	11
2999	11801	2013-7-25	$\alpha$	4
3122	11835	2013-8-26	$\beta$	0
3247	11857	2013-10-4	$\beta$	4
3286	11872	2013-10-17	$\beta$	0
3368	11896	2013-11-12	$\beta$	0

APPENDIX A. LIST OF ARS USED IN THIS WORK

---

Table 11: List of ARs featured in this thesis (2014–2017).

HARP Number	NOAA Number	Date of First NOAA Designation	Most Complex Mt. Wilson Class	Total Number of GOES Flares
3688	11968	2014-1-29	$\beta\gamma$	22
4375	12119	2014-7-19	$\beta$	1
4448	12139	2014-8-13	$\beta\gamma$	10
4667	12186	2014-10-9	$\beta$	0
4733	12196	2014-10-26	$\alpha$	0
5011	12253	2015-1-1	$\beta\gamma\delta$	34
5026	12257	2015-1-5	$\beta\gamma\delta$	17
5534	12337	2015-5-5	$\beta$	0
5543	12340	2015-5-9	$\beta$	0
5724	12375	2015-7-1	$\alpha$	0
5772	12386	2015-7-14	$\alpha$	2
5831	12394	2015-8-1	$\beta\gamma$	1
5940	12411	2015-9-6	$\beta$	0
6027	12436	2015-10-19	$\beta\delta$	15
6063	12443	2015-10-31	$\beta\gamma\delta$	43
6124	12457	2015-11-21	$\beta\gamma$	3
6223	12477	2016-1-3	$\alpha$	1
6403	12513	2016-3-4	$\alpha$	1
6505	12533	2016-4-22	$\alpha$	0
6558	12546	2016-5-16	$\beta$	13
6722	12581	2016-8-26	$\beta$	0
6846	12611	2016-11-19	$\beta$	7
6972	12644	2017-3-26	$\beta\gamma\delta$	19
6975	12645	2017-3-29	$\beta\gamma\delta$	15
7075	12665	2017-7-7	$\beta\gamma$	29
7107	12671	2017-8-16	$\beta\gamma\delta$	11
7115	12673	2017-8-31	$\beta\gamma\delta$	14

# References

- Alfvén, H. (1942), ‘Existence of Electromagnetic-Hydrodynamic Waves’, *Nature* **150**(3805), 405–406.
- Alfvén, H. (1943), ‘On the Existence of Electromagnetic-Hydrodynamic Waves’, *Arkiv for Matematik, Astronomi och Fysik* **29B**, 1–7.
- Alfvén, H. (1947), ‘Magneto hydrodynamic waves, and the heating of the solar corona’, *Monthly Notices of the Royal Astronomical Society* **107**, 211.
- Andrews, M. D. (2003), ‘A Search for CMEs Associated with Big Flares’, *Solar Physics* **218**(1), 261–279.
- Antalova, A. (1996), ‘Daily soft X-ray flare index (1969-1972)’, *Contributions of the Astronomical Observatory Skalnaté Pleso* **26**(2), 98–120.
- Antolin, P. (2020), ‘Thermal instability and non-equilibrium in solar coronal loops: from coronal rain to long-period intensity pulsations’, *Plasma Physics and Controlled Fusion* **62**(1), 014016.
- Arlt, R. and Vaquero, J. M. (2020), ‘Historical sunspot records’, *Living Reviews in Solar Physics* **17**(1), 1.
- Aschwanden, M. J. (2016), ‘Global Energetics of Solar Flares. IV. Coronal Mass Ejection Energetics’, *The Astrophysical Journal* **831**(1), 105.
- Aschwanden, M. J., Caspi, A., Cohen, C. M. S., Holman, G., Jing, J., Kretzschmar, M., Kontar, E. P., McTiernan, J. M., Mewaldt, R. A., O’Flannagain, A., Richardson, I. G., Ryan, D., Warren, H. P. and Xu, Y. (2019), Global Energetics of Solar Flares and Coronal Mass Ejections, *in*

## REFERENCES

---

- ‘Journal of Physics Conference Series’, Vol. 1332 of *Journal of Physics Conference Series*, p. 012002.
- Aschwanden, M. J., Xu, Y. and Jing, J. (2014), ‘Global Energetics of Solar Flares. I. Magnetic Energies’, *The Astrophysical Journal* **797**(1), 50.
- Asensio Ramos, A., Requerey, I. S. and Vitas, N. (2017), ‘DeepVel: Deep learning for the estimation of horizontal velocities at the solar surface’, *Astronomy & Astrophysics* **604**, A11.
- Astropy Collaboration, Price-Whelan, A. M., Sipőcz, B. M., Günther, H. M., Lim, P. L., Crawford, S. M., Conseil, S., Shupe, D. L., Craig, M. W., Dencheva, N., Ginsburg, A., VanderPlas, J. T., Bradley, L. D., Pérez-Suárez, D., de Val-Borro, M., Aldcroft, T. L., Cruz, K. L., Robitaille, T. P., Tollerud, E. J., Ardelean, C., Babej, T., Bach, Y. P., Bachetti, M., Bakanov, A. V., Bamford, S. P., Barentsen, G., Barmby, P., Baumbach, A., Berry, K. L., Biscani, F., Boquien, M., Bostroem, K. A., Bouma, L. G., Brammer, G. B., Bray, E. M., Breytenbach, H., Buddelmeijer, H., Burke, D. J., Calderone, G., Cano Rodríguez, J. L., Cara, M., Cardoso, J. V. M., Cheedella, S., Copin, Y., Corrales, L., Crichton, D., D’Avella, D., Deil, C., Depagne, É., Dietrich, J. P., Donath, A., Droettboom, M., Earl, N., Erben, T., Fabbro, S., Ferreira, L. A., Finethy, T., Fox, R. T., Garrison, L. H., Gibbons, S. L. J., Goldstein, D. A., Gommers, R., Greco, J. P., Greenfield, P., Groener, A. M., Grollier, F., Hagen, A., Hirst, P., Homeier, D., Horton, A. J., Hosseinzadeh, G., Hu, L., Hunkeler, J. S., Ivezić, Ž., Jain, A., Jenness, T., Kanarek, G., Kendrew, S., Kern, N. S., Kerzendorf, W. E., Khvalko, A., King, J., Kirkby, D., Kulkarni, A. M., Kumar, A., Lee, A., Lenz, D., Littlefair, S. P., Ma, Z., Macleod, D. M., Mastropietro, M., McCully, C., Montagnac, S., Morris, B. M., Mueller, M., Mumford, S. J., Muna, D., Murphy, N. A., Nelson, S., Nguyen, G. H., Ninan, J. P., Nöthe, M., Ogaz, S., Oh, S., Parejko, J. K., Parley, N., Pascual, S., Patil, R., Patil, A. A., Plunkett, A. L., Prochaska, J. X., Rastogi, T., Reddy Janga, V., Sabater, J., Sakurikar, P., Seifert, M., Sherbert, L. E., Sherwood-Taylor, H., Shih, A. Y., Sick, J., Silbiger, M. T., Singanamalla, S., Singer, L. P., Sladen, P. H., Sooley, K. A., Sornarajah, S., Streicher, O., Teuben, P., Thomas, S. W., Tremblay, G. R., Turner, J. E. H., Terrón, V., van Kerkwijk, M. H., de la Vega, A., Watkins, L. L., Weaver, B. A., Whitmore, J. B., Woillez, J., Zabalza, V. and Astropy Contributors (2018), ‘The Astropy Project: Building an Open-science Project and Status of the v2.0 Core Package’, *The Astronomical Journal* **156**(3), 123.

- Astropy Collaboration, Robitaille, T. P., Tollerud, E. J., Greenfield, P., Droettboom, M., Bray, E., Aldcroft, T., Davis, M., Ginsburg, A., Price-Whelan, A. M., Kerzendorf, W. E., Conley, A., Crighton, N., Barbary, K., Muna, D., Ferguson, H., Grollier, F., Parikh, M. M., Nair, P. H., Unther, H. M., Deil, C., Woillez, J., Conseil, S., Kramer, R., Turner, J. E. H., Singer, L., Fox, R., Weaver, B. A., Zabalza, V., Edwards, Z. I., Azalee Bostroem, K., Burke, D. J., Casey, A. R., Crawford, S. M., Dencheva, N., Ely, J., Jenness, T., Labrie, K., Lim, P. L., Pierfederici, F., Pontzen, A., Ptak, A., Refsdal, B., Servillat, M. and Streicher, O. (2013), ‘Astropy: A community Python package for astronomy’, *Astronomy & Astrophysics* **558**, A33.
- Athay, R. G. (1976), *The solar chromosphere and corona: Quiet sun*, Vol. 53.
- Bellot Rubio, L. and Orozco Suárez, D. (2019), ‘Quiet Sun magnetic fields: an observational view’, *Living Reviews in Solar Physics* **16**(1), 1.
- Benz, A. O. (2017), ‘Flare Observations’, *Living Reviews in Solar Physics* **14**(1), 2.
- Berger, M. A. (2005), ‘Magnetic Helicity Conservation’, *Highlights of Astronomy* **13**, 85.
- Berger, M. A. and Field, G. B. (1984), ‘The topological properties of magnetic helicity’, *Journal of Fluid Mechanics* **147**, 133–148.
- Bi, Y., Liu, Y. D., Liu, Y., Yang, J., Xu, Z. and Ji, K. (2018), ‘A Survey of Changes in Magnetic Helicity Flux on the Photosphere During Relatively Low-class Flares’, *The Astrophysical Journal* **865**(2), 139.
- Bobra, M. G., Mumford, S. J., Hewett, R. J., Christe, S. D., Reardon, K., Savage, S., Ireland, J., Pereira, T. M. D., Chen, B. and Pérez-Suárez, D. (2020), ‘A Survey of Computational Tools in Solar Physics’, *Solar Physics* **295**(4), 57.
- Bobra, M. G., Sun, X., Hoeksema, J. T., Turmon, M., Liu, Y., Hayashi, K., Barnes, G. and Leka, K. D. (2014), ‘The Helioseismic and Magnetic Imager (HMI) Vector Magnetic Field Pipeline: SHARPs - Space-Weather HMI Active Region Patches’, *Solar Physics* **289**(9), 3549–3578.
- Bolduc, L. (2002), ‘GIC observations and studies in the Hydro-Québec power system’, *Journal of Atmospheric and Solar-Terrestrial Physics* **64**(16), 1793–1802.

## REFERENCES

---

- Borrero, J. M., Tomczyk, S., Kubo, M., Socas-Navarro, H., Schou, J., Couvidat, S. and Bogart, R. (2011), ‘VFISV: Very Fast Inversion of the Stokes Vector for the Helioseismic and Magnetic Imager’, *Solar Physics* **273**(1), 267–293.
- Borrero, J. M., Tomczyk, S., Norton, A., Darnell, T., Schou, J., Scherrer, P., Bush, R. and Liu, Y. (2007), ‘Magnetic Field Vector Retrieval With the Helioseismic and Magnetic Imager’, *Solar Physics* **240**(1), 177–196.
- Camporeale, E. (2019), ‘The Challenge of Machine Learning in Space Weather: Nowcasting and Forecasting’, *Space Weather* **17**(8), 1166–1207.
- Chae, J. (2001), ‘Observational Determination of the Rate of Magnetic Helicity Transport through the Solar Surface via the Horizontal Motion of Field Line Footpoints’, *The Astrophysical Journal* **560**(1), L95–L98.
- Chandrasekhar, S. (1960), *Radiative transfer*.
- Chapman, S. (1937), ‘The heating of the ionosphere by the electric currents associated with geomagnetic variations’, *Terrestrial Magnetism and Atmospheric Electricity (Journal of Geophysical Research)* **42**(4), 355.
- Chapman, S. and Ferraro, V. C. A. (1940), ‘The theory of the first phase of a geomagnetic storm’, *Terrestrial Magnetism and Atmospheric Electricity (Journal of Geophysical Research)* **45**(3), 245.
- Charbonneau, P. (2014), ‘Solar Dynamo Theory’, *Annual Review of Astronomy and Astrophysics* **52**, 251–290.
- Charbonneau, P. (2016), ‘Solar physics: Dynamo theory questioned’, *Nature* **535**(7613), 500–501.
- Charbonneau, P. (2020), ‘Dynamo models of the solar cycle’, *Living Reviews in Solar Physics* **17**(1), 4.
- Christe, S., Barnes, W. T., Bobra, M., Freij, N., Hayes, L., Ireland, J., Mumford, S., Pérez-Suárez, D., Ryan, D., Shih, A. Y., Chand a, P., Glogowski, S., Hewett, R., Hughitt, V. K., Hill, A., Hiware, K., Inglis, A., Kirk, M. S., Konge, S., Mason, J. P., Maloney, S., Park, J., Pereira, T. J., Reardon, K., Savage, S. L., Yadav, T., Taylor, G., Stansby, D., Jain, Y., Sipocz, B., Rajulapati,

- C. R. and Panda, A. (2019), SunPy v1.0, the community-developed, free and open-source solar data analysis environment for Python., in ‘AGU Fall Meeting Abstracts’, Vol. 2019, pp. SH41C–3309.
- Cliver, E. W. and Dietrich, W. F. (2013), ‘The 1859 space weather event revisited: limits of extreme activity’, *Journal of Space Weather and Space Climate* **3**, A31.
- del Toro Iniesta, J. C. (2007), *Introduction to Spectropolarimetry*.
- Démoulin, P. and Berger, M. A. (2003), ‘Magnetic Energy and Helicity Fluxes at the Photospheric Level’, *Solar Physics* **215**(2), 203–215.
- DeRosa, M. L. (2001), Dynamics in the upper solar convection zone, PhD thesis, UNIVERSITY OF COLORADO AT BOULDER.
- Diamond, P. H. and Malkov, M. (2003), ‘Dynamics of helicity transport and Taylor relaxation’, *Physics of Plasmas* **10**(6), 2322–2329.
- Domingo, V., Fleck, B. and Poland, A. I. (1995), ‘The SOHO Mission: an Overview’, *Solar Physics* **162**(1-2), 1–37.
- Dominguez-Tagle, C., Collados, M., Lopez, R. L., Vaz Cedillo, J. J., Esteves, M. A., Paez, E. and Asensio Ramos, A. (2017), First tests on the Integral Field Unit for GRIS at GREGOR, in ‘SOLARNET IV Meeting’, p. 89.
- Eddington, A. S. (1926), Cambridge University Press, Cambridge.
- Eddington, A. S. (1988), *The Internal Constitution of the Stars*, Cambridge University Press, Cambridge.
- Emslie, A. G., Dennis, B. R., Holman, G. D. and Hudson, H. S. (2005), ‘Refinements to flare energy estimates: A followup to “Energy partition in two solar flare/CME events” by A. G. Emslie et al.’, *Journal of Geophysical Research (Space Physics)* **110**(A11), A11103.
- Fan, Y. L., Wang, H. N., He, H. and Zhu, X. S. (2011), ‘Study of the Poynting Flux in Active Region 10930 Using Data-driven Magnetohydrodynamic Simulation’, *The Astrophysical Journal* **737**(1), 39.

## REFERENCES

---

- Frisch, H. (1972), 'The Solar Chromosphere and Its Transition to the Corona', *Space Science Reviews* **13**(3), 455–483.
- Gary, G. A. and Hagyard, M. J. (1990), 'Transformation of vector magnetograms and the problems associated with the effects of perspective and the azimuthal ambiguity', *Solar Physics* **126**, 21–36.
- Georgoulis, M. K. and LaBonte, B. J. (2006), 'Reconstruction of an Inductive Velocity Field Vector from Doppler Motions and a Pair of Solar Vector Magnetograms', *The Astrophysical Journal* **636**(1), 475–495.
- Gingerich, O., Noyes, R. W., Kalkofen, W. and Cuny, Y. (1971), 'The Harvard-Smithsonian reference atmosphere', *Solar Physics* **18**(3), 347–365.
- Giovanelli, R. G. (1939), 'The Relations Between Eruptions and Sunspots.', *ApJ* **89**, 555.
- Gonzalez, W. D., Joselyn, J. A., Kamide, Y., Kroehl, H. W., Rostoker, G., Tsurutani, B. T. and Vasyliunas, V. M. (1994), 'What is a geomagnetic storm?', *Journal of Geophysical Research* **99**(A4), 5771–5792.
- Hale, G. E. (1908), 'The Zeeman Effect in the Sun', *Publications of the Astronomical Society of the Pacific* **20**(123), 287.
- Hale, G. E., Ellerman, F., Nicholson, S. B. and Joy, A. H. (1919), 'The Magnetic Polarity of Sun-Spots', *ApJ* **49**, 153.
- Hanle, W. (1925), 'Die magnetische Beeinflussung der Resonanzfluoreszenz', *Ergebnisse der exakten Naturwissenschaften* **4**, 214.
- Harvey, K. L. (1994), The solar magnetic cycle, in R. J. Rutten and C. J. Schrijver, eds, 'NATO Advanced Science Institutes (ASI) Series C', Vol. 433 of *NATO Advanced Science Institutes (ASI) Series C*, p. 347.
- Hathaway, D. H. (2015), 'The Solar Cycle', *Living Reviews in Solar Physics* **12**(1), 4.
- Hayakawa, H., Ebihara, Y., Cliver, E. W., Hattori, K., Toriumi, S., Love, J. J., Umemura, N., Namekata, K., Sakaue, T., Takahashi, T. and Shibata, K. (2019), 'The extreme space weather

- event in September 1909', *Monthly Notices of the Royal Astronomical Society* **484**(3), 4083–4099.
- Hoeksema, J. T., Liu, Y., Hayashi, K., Sun, X., Schou, J., Couvidat, S., Norton, A., Bobra, M., Centeno, R., Leka, K. D., Barnes, G. and Turmon, M. (2014), 'The Helioseismic and Magnetic Imager (HMI) Vector Magnetic Field Pipeline: Overview and Performance', *Solar Physics* **289**(9), 3483–3530.
- Hoyt, D. V. and Schatten, K. H. (1998), 'Group Sunspot Numbers: A New Solar Activity Reconstruction', *Sol. Phys.* **181**(2), 491–512.
- Hrazdřira, Z., Druckmüller, M. and Habbal, S. (2021), 'Measuring Solar Differential Rotation with an Iterative Phase Correlation Method', *The Astrophysical Journal Supplement Series* **252**(1), 6.
- Hughitt, V. K., Christe, S., Ireland, J., Shih, A., Mayer, F., Earnshaw, M. D., Young, C., Perez-Suarez, D. and Schwartz, R. (2012), SunPy: Python for Solar Physics Data Analysis, in 'American Astronomical Society Meeting Abstracts #220', Vol. 220 of *American Astronomical Society Meeting Abstracts*, p. 522.07.
- Hurlburt, N. E., Schrijver, C. J., Shine, R. A. and Title, A. M. (1995), Simulated MDI Observations of Convection, in 'Helioseismology', Vol. 376 of *ESA Special Publication*, p. 239.
- Ignace, R., Nordsieck, K. H. and Cassinelli, J. P. (1997), 'The Hanle Effect as a Diagnostic of Magnetic Fields in Stellar Envelopes. I. Theoretical Results for Integrated Line Profiles', *The Astrophysical Journal* **486**(1), 550–570.
- Jaeggli, S. A. and Norton, A. A. (2016), 'The Magnetic Classification of Solar Active Regions 1992-2015', *The Astrophysical Journal Letters* **820**(1), L11.
- Joshi, B. and Joshi, A. (2004), 'The North—South Asymmetry of Soft X-Ray Flare Index During Solar Cycles 21, 22 and 23', *Solar Physics* **219**(2), 343–356.
- Kaiser, M. L., Kucera, T. A., Davila, J. M., St. Cyr, O. C., Guhathakurta, M. and Christian, E. (2008), 'The STEREO Mission: An Introduction', *Space Science Reviews* **136**(1-4), 5–16.
- Kazachenko, M. D., Fisher, G. H., Welsch, B. T., Liu, Y. and Sun, X. (2015), 'Photospheric Elec-

## REFERENCES

---

- tric Fields and Energy Fluxes in the Eruptive Active Region NOAA 11158’, *The Astrophysical Journal* **811**(1), 16.
- Kosugi, T., Matsuzaki, K., Sakao, T., Shimizu, T., Sone, Y., Tachikawa, S., Hashimoto, T., Minesugi, K., Ohnishi, A., Yamada, T., Tsuneta, S., Hara, H., Ichimoto, K., Suematsu, Y., Shimojo, M., Watanabe, T., Shimada, S., Davis, J. M., Hill, L. D., Owens, J. K., Title, A. M., Culhane, J. L., Harra, L. K., Doschek, G. A. and Golub, L. (2007), ‘The Hinode (Solar-B) Mission: An Overview’, *Solar Physics* **243**(1), 3–17.
- Kuperus, M. (1969), ‘The Heating of the Solar Corona’, *Space Science Reviews* **9**(5), 713–739.
- Kusano, K., Maeshiro, T., Yokoyama, T. and Sakurai, T. (2002), ‘Measurement of Magnetic Helicity Injection and Free Energy Loading into the Solar Corona’, *The Astrophysical Journal* **577**(1), 501–512.
- Landi Degl’Innocenti, E. (1992), *Magnetic field measurements.*, p. 71.
- Landstreet, J. D. (2015), Basics of spectropolarimetry, in G. Meynet, C. Georgy, J. Groh and P. Stee, eds, ‘New Windows on Massive Stars’, Vol. 307 of *IAU Symposium*, pp. 311–320.
- Leenaarts, J. (2020), ‘Radiation hydrodynamics in simulations of the solar atmosphere’, *Living Reviews in Solar Physics* **17**(1), 3.
- Leka, K. D. and Barnes, G. (2003), ‘Photospheric Magnetic Field Properties of Flaring versus Flare-quiet Active Regions. II. Discriminant Analysis’, *The Astrophysical Journal* **595**(2), 1296–1306.
- Lemen, J. R., Title, A. M., Akin, D. J., Boerner, P. F., Chou, C., Drake, J. F., Duncan, D. W., Edwards, C. G., Friedlaender, F. M., Heyman, G. F., Hurlburt, N. E., Katz, N. L., Kushner, G. D., Levay, M., Lindgren, R. W., Mathur, D. P., McFeaters, E. L., Mitchell, S., Rehse, R. A., Schrijver, C. J., Springer, L. A., Stern, R. A., Tarbell, T. D., Wuelser, J.-P., Wolfson, C. J., Yanari, C., Bookbinder, J. A., Cheimets, P. N., Caldwell, D., Deluca, E. E., Gates, R., Golub, L., Park, S., Podgorski, W. A., Bush, R. I., Scherrer, P. H., Gummin, M. A., Smith, P., Aufer, G., Jerram, P., Pool, P., Soufli, R., Windt, D. L., Beardsley, S., Clapp, M., Lang, J. and Waltham, N. (2012), ‘The Atmospheric Imaging Assembly (AIA) on the Solar Dynamics Observatory (SDO)’, *Sol. Phys.* **275**(1-2), 17–40.

- Li, Q., Yan, X., Wang, J., Kong, D., Xue, Z. and Yang, L. (2019), ‘The Formation and Decay of Sunspot Penumbrae in Active Region NOAA 12673’, *The astrophysical journal* **886**(2), 149.
- Li, Y., Lynch, B. J., Welsch, B. T., Stenborg, G. A., Luhmann, J. G., Fisher, G. H., Liu, Y. and Nightingale, R. W. (2010), ‘Sequential Coronal Mass Ejections from AR8038 in May 1997’, *Solar Physics* **264**(1), 149–164.
- Liu, C., Xu, Y., Cao, W., Deng, N., Lee, J., Hudson, H. S., Gary, D. E., Wang, J., Jing, J. and Wang, H. (2016), ‘Flare differentially rotates sunspot on Sun’s surface’, *Nature Communications* **7**, 13104.
- Liu, J., Sun, X. and Schuck, P. (2020), Estimating Magnetic Energy and Helicity Flux in Solar Active Regions with Doppler Velocities, in ‘AAS/Solar Physics Division Meeting’, Vol. 52 of *AAS/Solar Physics Division Meeting*, p. 207.07.
- Liu, Y., Hoeksema, J. T., Bobra, M., Hayashi, K., Schuck, P. W. and Sun, X. (2014), ‘Magnetic Helicity in Emerging Solar Active Regions’, *The Astrophysical Journal* **785**(1), 13.
- Liu, Y. and Schuck, P. W. (2012), ‘Magnetic Energy and Helicity in Two Emerging Active Regions in the Sun’, *The Astrophysical Journal* **761**(2), 105.
- Longcope, D. W. (2004), ‘Inferring a Photospheric Velocity Field from a Sequence of Vector Magnetograms: The Minimum Energy Fit’, *The Astrophysical Journal* **612**(2), 1181–1192.
- Lu, Y., Wang, J. and Wang, H. (1993), ‘Shear Angle of Magnetic Fields’, *Solar Physics* **148**(1), 119–132.
- Maehara, H., Shibayama, T., Notsu, S., Notsu, Y., Nagao, T., Kusaba, S., Honda, S., Nogami, D. and Shibata, K. (2012), ‘Superflares on solar-type stars’, *Nature* **485**(7399), 478–481.
- Mandal, S. and Banerjee, D. (2016), ‘Sunspot Sizes and the Solar Cycle: Analysis Using Kodaikanal White-light Digitized Data’, *The Astrophysical Journal Letters* **830**(2), L33.
- McCloskey, A. E., Gallagher, P. T. and Bloomfield, D. S. (2016), ‘Flaring Rates and the Evolution of Sunspot Group McIntosh Classifications’, *Solar Physics* **291**(6), 1711–1738.

## REFERENCES

---

- McCloskey, A. E., Gallagher, P. T. and Bloomfield, D. S. (2018), 'Flare forecasting using the evolution of McIntosh sunspot classifications', *Journal of Space Weather and Space Climate* **8**, A34.
- McIntosh, P. S. (1990), 'The Classification of Sunspot Groups', *Sol. Phys.* **125**(2), 251–267.
- Metcalf, T. R. (1994), 'Resolving the 180-degree ambiguity in vector magnetic field measurements: The 'minimum' energy solution', *Solar Physics* **155**(2), 235–242.
- Milne, E. A. (1921), 'Radiative equilibrium in the outer layers of a star', *Monthly Notices of the Royal Astronomical Society* **81**, 361–375.
- Moore, R. L., Sterling, A. C., Hudson, H. S. and Lemen, J. R. (2001), 'Onset of the Magnetic Explosion in Solar Flares and Coronal Mass Ejections', *The Astrophysical Journal* **552**(2), 833–848.
- Moraitis, K., Pariat, E., Valori, G. and Dalmasse, K. (2019), 'Relative magnetic field line helicity', *Astronomy & Astrophysics* **624**, A51.
- Murabito, M., Ermolli, I., Giorgi, F., Stangalini, M., Guglielmino, S. L., Jafarzadeh, S., Socas-Navarro, H., Romano, P. and Zuccarello, F. (2020), The penumbral solar filaments from the photosphere to the chromosphere, in 'Journal of Physics Conference Series', Vol. 1548 of *Journal of Physics Conference Series*, p. 012017.
- Murabito, M., Guglielmino, L., Ermolli, I., Stangalini, M. and Giorgi, F. (2020a), 'Penumbral Brightening Events Observed in AR NOAA 12546', *The astrophysical journal* **890**(2), 96.
- Murabito, M., Guglielmino, S. L., Ermolli, I., Stangalini, M. and Giorgi, F. (2020b), 'Penumbral brightening events observed in AR NOAA 12546', *The Astrophysical Journal* **890**(2), 96.
- Nakagawa, Y., Raadu, M. A. and Harvey, J. W. (1973), 'The Topological Association of H $\alpha$  Structures and Magnetic Fields', *Sol. Phys.* **30**(2), 421–437.
- November, L. J. and Simon, G. W. (1988), 'Precise Proper-Motion Measurement of Solar Granulation', *The Astrophysical Journal* **333**, 427.
- Osterbrock, D. E. (1961a), 'Heating of the Solar Chromosphere, Plages, and Corona by Magneto-hydrodynamic Waves.', *Astronomical Journal* **70**, 50.

- Osterbrock, D. E. (1961*b*), ‘The Heating of the Solar Chromosphere, Plages, and Corona by Magnetohydrodynamic Waves.’, *Astrophysical Journal* **134**, 347.
- Owens, M. J., Lockwood, M., Hawkins, E., Usoskin, I., Jones, G. S., Barnard, L., Schurer, A. and Fasullo, J. (2017), ‘The Maunder minimum and the Little Ice Age: an update from recent reconstructions and climate simulations’, *Journal of Space Weather and Space Climate* **7**, A33.
- Parker, E. N. (1965), ‘Dynamical Theory of the Solar Wind’, *Space Science Reviews* **4**(5-6), 666–708.
- Parker, E. N. (1979), *Cosmical magnetic fields. Their origin and their activity*.
- Parker, E. N. (1988), ‘Nanoflares and the Solar X-Ray Corona’, *The Astrophysical Journal* **330**, 474.
- Pence, W. D., Chiappetti, L., Page, C. G., Shaw, R. A. and Stobie, E. (2010), ‘Definition of the Flexible Image Transport System (FITS), version 3.0’, *Astronomy and Astrophysics* **524**, A42.
- Pesnell, W. D., Thompson, B. J. and Chamberlin, P. C. (2012), ‘The Solar Dynamics Observatory (SDO)’, *Sol. Phys.* **275**(1-2), 3–15.
- Petrovay, K. (2020), ‘Solar cycle prediction’, *Living Reviews in Solar Physics* **17**(1), 2.
- Piddington, J. H. (1956), ‘Solar atmospheric heating by hydromagnetic waves’, *Monthly Notices of the Royal Astronomical Society* **116**, 314.
- Rachkovsky, D. N. (1962), ‘Magnetic rotation effects in spectral lines’, *Izvestiya Ordena Trudovogo Krasnogo Znameni Krymskoj Astrofizicheskoj Observatorii* **28**, 259–270.
- Régnier, S. (2012), ‘Magnetic Energy Storage and Current Density Distributions for Different Force-Free Models’, *Solar Physics* **277**(1), 131–151.
- Régnier, S. (2013), ‘Magnetic Field Extrapolations into the Corona: Success and Future Improvements’, *Solar Physics* **288**(2), 481–505.
- Riley, P. (2012), ‘On the probability of occurrence of extreme space weather events’, *Space Weather* **10**(2), 02012.

## REFERENCES

---

- Romano, P., Elmhamdi, A. and Kordi, A. S. (2019), ‘Two Strong White-Light Solar Flares in AR NOAA 12673 as Potential Clues for Stellar Superflares’, *Solar Physics* **294**(1), 4.
- Romano, P., Zuccarello, F., Guglielmino, S. L., Berrilli, F., Bruno, R., Carbone, V., Consolini, G., de Lauretis, M., Del Moro, D., Elmhamdi, A., Ermolli, I., Fineschi, S., Francia, P., Kordi, A. S., Landi Degl’Innocenti, E., Laurenza, M., Lepreti, F., Marcucci, M. F., Pallocchia, G., Pietropaolo, E., Romoli, M., Vecchio, A., Vellante, M. and Villante, U. (2015), ‘Recurrent flares in active region NOAA 11283’, *Astronomy & Astrophysics* **582**, A55.
- Ruan, G., Chen, Y., Wang, S., Zhang, H., Li, G., Jing, J., Su, J., Li, X., Xu, H., Du, G. and Wang, H. (2014), ‘A Solar Eruption Driven by Rapid Sunspot Rotation’, *The Astrophysical Journal* **784**(2), 165.
- Rušin, V., Druckmüller, M., Aniol, P., Minarovjech, M., Saniga, M., Mikić, Z., Linker, J. A., Lionello, R., Riley, P. and Titov, V. S. (2010), ‘Comparing eclipse observations of the 2008 August 1 solar corona with an MHD model prediction’, *Astronomy and Astrophysics* **513**, A45.
- Santiago, J. M. B. (2004), The fine structure of the sunspot penumbra, PhD thesis, Universitat zu Göttingen.
- Schaefer, B. E., King, J. R. and Deliyannis, C. P. (2000), ‘Superflares on Ordinary Solar-Type Stars’, *The Astrophysical Journal* **529**(2), 1026–1030.
- Schatzman, E. (1949), ‘The heating of the solar corona and chromosphere’, *Annales d’Astrophysique* **12**, 203.
- Scherrer, P. H., Bogart, R. S., Bush, R. I., Hoeksema, J. T., Kosovichev, A. G., Schou, J., Rosenberg, W., Springer, L., Tarbell, T. D., Title, A., Wolfson, C. J., Zayer, I. and MDI Engineering Team (1995), ‘The Solar Oscillations Investigation - Michelson Doppler Imager’, *Solar Physics* **162**(1-2), 129–188.
- Scherrer, P. H., Schou, J., Bush, R. I., Kosovichev, A. G., Bogart, R. S., Hoeksema, J. T., Liu, Y., Duvall, T. L., Zhao, J., Title, A. M., Schrijver, C. J., Tarbell, T. D. and Tomczyk, S. (2012), ‘The Helioseismic and Magnetic Imager (HMI) Investigation for the Solar Dynamics Observatory (SDO)’, *Solar Physics* **275**(1-2), 207–227.

- Schmidt, W., von der Lühe, O., Volkmer, R., Denker, C., Solanki, S. K., Balthasar, H., Bello Gonzalez, N., Berkefeld, T., Collados, M., Fischer, A., Halbgewachs, C., Heidecke, F., Hofmann, A., Kneer, F., Lagg, A., Nicklas, H., Popow, E., Puschmann, K. G., Schmidt, D., Sigwarth, M., Sobotka, M., Soltau, D., Staude, J., Strassmeier, K. G. and Waldmann, T. A. (2012), 'The 1.5 meter solar telescope GREGOR', *Astronomische Nachrichten* **333**(9), 796.
- Schrijver, C. J., Beer, J., Baltensperger, U., Cliver, E. W., Güdel, M., Hudson, H. S., McCracken, K. G., Osten, R. A., Peter, T., Soderblom, D. R., Usoskin, I. G. and Wolff, E. W. (2012), 'Estimating the frequency of extremely energetic solar events, based on solar, stellar, lunar, and terrestrial records', *Journal of Geophysical Research (Space Physics)* **117**(A8), A08103.
- Schrijver, C. J., Kauristie, K., Aylward, A. D., Denardini, C. M., Gibson, S. E., Glover, A., Gopalswamy, N., Grande, M., Hapgood, M., Heynderickx, D., Jakowski, N., Kalegaev, V. V., Lapenta, G., Linker, J. A., Liu, S., Mandrini, C. H., Mann, I. R., Nagatsuma, T., Nandy, D., Obara, T., Paul O'Brien, T., Onsager, T., Opgenoorth, H. J., Terkildsen, M., Valladares, C. E. and Vilmer, N. (2015), 'Understanding space weather to shield society: A global road map for 2015-2025 commissioned by COSPAR and ILWS', *Advances in Space Research* **55**(12), 2745–2807.
- Schrijver, C. J. and Mitchell, S. D. (2013), 'Disturbances in the US electric grid associated with geomagnetic activity', *Journal of Space Weather and Space Climate* **3**, A19.
- Schrijver, C. J. and Zwaan, C. (2008), *Solar and Stellar Magnetic Activity*.
- Schuck, P. W. (2006), Tracking Magnetic Footprints in Active Regions, in 'AAS/Solar Physics Division Meeting #37', AAS/Solar Physics Division Meeting, p. 34.05.
- Schuck, P. W. (2008), 'Tracking Vector Magnetograms with the Magnetic Induction Equation', *The Astrophysical Journal* **683**(2), 1134–1152.
- SILSO World Data Center (n.d.), 'The international sunspot number', *International Sunspot Number Monthly Bulletin and online catalogue*.
- Silva, A. C. A. (2017), Evolution of active regions based on solar-surface magnetic flux observations and coronal magnetic fields extrapolations: a case-study of NOAA 12443., PhD thesis, Instituto Nacional de Pesquisas Espaciais.

## REFERENCES

---

- Simon, G. W. and Weiss, N. O. (1970), 'On the Magnetic Field in Pores', *Solar Physics* **13**(1), 85–103.
- Singer, H. J., Cash, M. D., Camporeale, E., Balch, C. C., Steenburgh, R. A., Murtagh, W. J., Millward, G. H., Toth, G. and Huang, Z. (2019), Predicting Geomagnetically Induced Currents (GICs): Meeting the Challenge with Improved Space Weather Services, in 'AGU Fall Meeting Abstracts', Vol. 2019, pp. IN41B–11.
- Smith, H. J. and Smith, E. V. P. (1963), *Solar flares*.
- Smith, S. F. and Howard, R. (1968), Magnetic Classification of Active Regions, in K. O. Kiepenheuer, ed., 'Structure and Development of Solar Active Regions', Vol. 35 of *IAU Symposium*, p. 33.
- Solanki, S. K. (1993), 'Smallscale Solar Magnetic Fields - an Overview', *Space Science Reviews* **63**(1-2), 1–188.
- Solanki, S. K. (2002), 'The magnetic structure of sunspots and starspots', *Astronomische Nachrichten* **323**, 165–177.
- Solov'ev, A. A., Parfinenko, L. D., Efremov, V. I., Kirichek, E. A. and Korolkova, O. A. (2019), 'Structure of photosphere under high resolution: granules, faculae, micropores, intergranular lanes', *Astrophysics and Space Science* **364**(12), 222.
- Spann, J. F., Talaat, E. R., Keshian, J., Bonadonna, L. C. M. F., Murtagh, W. J., Blunt, K., Backhaus, S. and Farrar, M. (2019), National Space Weather Strategy and Action Plan - implications for space weather observations and applications, in 'AGU Fall Meeting Abstracts', Vol. 2019, pp. IN51B–07.
- Stern, D. P. (1966), 'The Motion of Magnetic Field Lines', *Space Science Reviews* **6**(2), 147–173.
- Su, Y., Liu, R., Li, S., Cao, W., Ahn, K. and Ji, H. (2018), 'High-resolution Observations of Flares in an Arch Filament System', *The Astrophysical Journal* **855**(2), 77.
- Tan, C., Jing, J., Abramenko, V. I., Pevtsov, A. A., Song, H., Park, S.-H. and Wang, H. (2007), 'Statistical Correlations between Parameters of Photospheric Magnetic Fields and Coronal Soft X-Ray Brightness', *The Astrophysical Journal* **665**(2), 1460–1468.

- Taylor, J. B. (1974), ‘Relaxation of Toroidal Plasma and Generation of Reverse Magnetic Fields’, *Physical Review Letters* **33**(19), 1139–1141.
- Thompson, W. T. (2006), The FITS World Coordinate System for Solar Images, in ‘AAS/Solar Physics Division Meeting #37’, AAS/Solar Physics Division Meeting, p. 3.07.
- Topasna, G. A. and Topasna, D. M. (2009), Stokes parameters in undergraduate laboratory exercises, in ‘Proceedings of the SPIE’, Vol. 9666 of *Society of Photo-Optical Instrumentation Engineers (SPIE) Conference Series*, p. 96660R.
- Toriumi, S. and Takasao, S. (2017), ‘Numerical Simulations of Flare-productive Active Regions:  $\delta$ -sunspots, Sheared Polarity Inversion Lines, Energy Storage, and Predictions’, *The astrophysical journal* **850**(1), 39.
- Toriumi, S. and Wang, H. (2019), ‘Flare-productive active regions’, *Living Reviews in Solar Physics* **16**(1), 3.
- Tritschler, A., Rimmele, T. R., Berukoff, S., Casini, R., Kuhn, J. R., Lin, H., Rast, M. P., McMullin, J. P., Schmidt, W., Wöger, F. and DKIST Team (2016), ‘Daniel K. Inouye Solar Telescope: High-resolution observing of the dynamic Sun’, *Astronomische Nachrichten* **337**(10), 1064.
- Trujillo Bueno, J. (2003), ‘Solar Magnetism and Astrophysical Spectropolarimetry’.
- Tsuneta, S., Ichimoto, K., Katsukawa, Y., Nagata, S., Otsubo, M., Shimizu, T., Suematsu, Y., Nakagiri, M., Noguchi, M., Tarbell, T., Title, A., Shine, R., Rosenberg, W., Hoffmann, C., Jurcevich, B., Kushner, G., Levay, M., Lites, B., Elmore, D., Matsushita, T., Kawaguchi, N., Saito, H., Mikami, I., Hill, L. D. and Owens, J. K. (2008), ‘The Solar Optical Telescope for the Hinode Mission: An Overview’, *Solar Physics* **249**(2), 167–196.
- Tsurutani, B. T., Gonzalez, W. D., Lakhina, G. S. and Alex, S. (2003), ‘The extreme magnetic storm of 1-2 September 1859’, *Journal of Geophysical Research (Space Physics)* **108**(A7), 1268.
- Tziotziou, K., Georgoulis, M. K. and Liu, Y. (2013), ‘Interpreting Eruptive Behavior in NOAA AR 11158 via the Region’s Magnetic Energy and Relative-helicity Budgets’, *The Astrophysical Journal* **772**(2), 115.

## REFERENCES

---

- Unno, W. (1956), ‘Line Formation of a Normal Zeeman Triplet’, *Publications of the Astronomical Society of Japan* **8**, 108.
- Usoskin, I. G., Arlt, R., Asvestari, E., Hawkins, E., Käpylä, M., Kovaltsov, G. A., Krivova, N., Lockwood, M., Mursula, K., O’Reilly, J., Owens, M., Scott, C. J., Sokoloff, D. D., Solanki, S. K., Soon, W. and Vaquero, J. M. (2015), ‘The Maunder minimum (1645-1715) was indeed a grand minimum: A reassessment of multiple datasets’, *Astronomy & Astrophysics* **581**, A95.
- van der Walt, S., Colbert, S. C. and Varoquaux, G. (2011), ‘The NumPy Array: A Structure for Efficient Numerical Computation’, *Computing in Science and Engineering* **13**(2), 22–30.
- van Driel-Gesztelyi, L. and Green, L. M. (2015), ‘Evolution of Active Regions’, *Living Reviews in Solar Physics* **12**(1), 1.
- Verma, M. (2018), ‘The origin of two X-class flares in active region NOAA 12673. Shear flows and head-on collision of new and preexisting flux’, *Astronomy & Astrophysics* **612**, A101.
- Virtanen, P., Gommers, R., Oliphant, T. E., Haberland, M., Reddy, T., Cournapeau, D., Burovski, E., Peterson, P., Weckesser, W., Bright, J., van der Walt, S. J., Brett, M., Wilson, J., Millman, K. J., Mayorov, N., Nelson, A. R. J., Jones, E., Kern, R., Larson, E., Carey, C. J., Polat, İ., Feng, Y., Moore, E. W., Vand erPlas, J., Laxalde, D., Perktold, J., Cimrman, R., Henriksen, I., Quintero, E. A., Harris, C. R., Archibald, A. M., Ribeiro, A. H., Pedregosa, F., van Mulbregt, P. and SciPy 1.0 Contributors (2020), ‘SciPy 1.0: fundamental algorithms for scientific computing in Python’, *Nature Methods* **17**, 261–272.
- Waldmeier, M. (1938), ‘Chromosphärische Eruptionen. I. Mit 6 Abbildungen.’, *Z. Astrophys.* **16**, 276.
- Wang, J. (1994), On the development of magnetic shear, in J. J. Hunt, ed., ‘Solar Dynamic Phenomena and Solar Wind Consequences, the Third SOHO Workshop’, Vol. 373 of *ESA Special Publication*, p. 83.
- Wang, J., Liu, C., Cao, W. and Wang, H. (2020), ‘High-resolution Observations of Small-scale Flux Emergence by GST’, *The astrophysical journal* **900**(1), 84.

- Wang, R., Liu, Y. D., Wiegelmann, T., Cheng, X., Hu, H. and Yang, Z. (2016), ‘Relationship Between Sunspot Rotation and a Major Solar Eruption on 12 July 2012’, *Solar Physics* **291**(4), 1159–1171.
- Warren, H. P., Crump, N. A., Ugarte-Urra, I., Sun, X., Aschwanden, M. J. and Wiegelmann, T. (2018), ‘Toward a Quantitative Comparison of Magnetic Field Extrapolations and Observed Coronal Loops’, *The Astrophysical Journal* **860**(1), 46.
- Waskom, M. and the seaborn development team (2020), ‘mwaskom/seaborn’.
- Wells, D. C., Greisen, E. W. and Harten, R. H. (1981), ‘FITS - a Flexible Image Transport System’, *Astronomy and Astrophysics Supplement* **44**, 363.
- Welsch, B. T. (2006), ‘Magnetic Flux Cancellation and Coronal Magnetic Energy’, *The Astrophysical Journal* **638**(2), 1101–1109.
- Welsch, B. T. (2015), ‘The photospheric Poynting flux and coronal heating’, *Publications of the Astronomical Society of Japan* **67**(2), 18.
- Welsch, B. T., Abnett, W. P., De Rosa, M. L., Fisher, G. H., Georgoulis, M. K., Kusano, K., Longcope, D. W., Ravindra, B. and Schuck, P. W. (2007), ‘Tests and Comparisons of Velocity-Inversion Techniques’, *The Astrophysical Journal* **670**(2), 1434–1452.
- Welsch, B. T., Christe, S. and McTiernan, J. M. (2011), ‘Photospheric Magnetic Evolution in the WHI Active Regions’, *Solar Physics* **274**(1-2), 131–157.
- Welsch, B. T., Fisher, G. H., Abnett, W. P. and Regnier, S. (2004), ‘ILCT: Recovering Photospheric Velocities from Magnetograms by Combining the Induction Equation with Local Correlation Tracking’, *The Astrophysical Journal* **610**(2), 1148–1156.
- Welsch, B. T., Fisher, G. H. and Sun, X. (2013), ‘A Magnetic Calibration of Photospheric Doppler Velocities’, *The Astrophysical Journal* **765**(2), 98.
- Welsch, B. T., Li, Y., Schuck, P. W. and Fisher, G. H. (2009), ‘What is the Relationship Between Photospheric Flow Fields and Solar Flares?’, *The Astrophysical Journal* **705**(1), 821–843.
- Wiegelmann, T., Petrie, G. J. D. and Riley, P. (2017), ‘Coronal Magnetic Field Models’, *Space Science Reviews* **210**(1-4), 249–274.

## REFERENCES

---

- Withbroe, G. L. and Noyes, R. W. (1977), 'Mass and energy flow in the solar chromosphere and corona.', *Annual review of astronomy and astrophysics* **15**, 363–387.
- Wolf, R. (1851), 'Auszug aus einem Schreiben des Herrn Professors Rudolf Wolf an den Herausgeber', *Astron. Nachr.* **32**(13), 193.
- Woltjer, L. (1958), 'A Theorem on Force-Free Magnetic Fields', *Proceedings of the National Academy of Science* **44**(6), 489–491.
- Yeates, A. R., Bianchi, F., Welsch, B. T. and Bushby, P. J. (2014), 'The coronal energy input from magnetic braiding', *Astronomy and Astrophysics* **564**, A131.
- Zeeman, P. (1897), 'The Effect of Magnetisation on the Nature of Light Emitted by a Substance', *Nature* **55**(1424), 347.